ADSORPTIVE REMOVAL OF DYES FROM AQUEOUS SOLUTIONS USING METAL ORGANIC FRAMEWORKS (MOFs)

by

Abdollah Karami

A Thesis presented to the Faculty of the
American University of Sharjah
College of Engineering
In Partial Fulfillment
of the Requirements
for the Degree of

Master of Science in
Chemical Engineering

Sharjah, United Arab Emirates

April 2019

Approval Signatures

We, the undersigned, approve the Master's Thesis of Abdollah Karami.

Thesis Title: Adsorptive Removal of Dyes from Aqueous Solutions Using Metal Organic Frameworks (MOFs).

Signature	**Date of Signature** (dd/mm/yyyy)
_____	_____
Dr. Rana Sabouni Assistant Professor, Department of Chemical Engineering Thesis Advisor	
_____	_____
Dr. Ahmed Aidan Senior Lab Instructor, Department of Chemical Engineering Thesis Co-Advisor	
_____	_____
Dr. Zarook Shareefdeen Professor, Department of Chemical Engineering Thesis Committee Member	
_____	_____
Dr. Kazi Fattah Associate Professor, Department of Civil Engineering Thesis Committee Member	
_____	_____
Dr. Sameer Al-Asheh Interim Head, Department of Chemical Engineering	
_____	_____
Dr. Lotfi Romdhane Associate Dean for Graduate Affairs and Research College of Engineering	
_____	_____
Dr. Naif Darwish Acting Dean, College of Engineering	
_____	_____
Dr. Mohamed El-Tarhuni Vice Provost for Graduate Studies	

Acknowledgement

I am profoundly grateful for my advisor, Dr. Rana Sabouni. Her dedication, thoughtful suggestions, and generous support helped me overcome the challenges I faced throughout the thesis work. It was my pleasure and privilege working under her supervision. I could never thank her enough.

I would like to express my sincere gratitude to my co-advisor, Dr. Ahmed Aidan for his support, care, and constant encouragement from the first day I joined the master program. I am thankful for his assistance during my work in the lab.

I would also like to thank Dr. Ghaleb's Drug Delivery group for allowing me to use their lab equipment and instruments which were essential in the completion of my thesis work. Also, I would like to thank Dr. Mohammad Al-Sayah for his help and valuable input.

My sincere thanks go to Engineer Muhammad Qasim and Engineer Mohamed Badrelzaman for their valuable technical input and suggestions that helped me in the experimental work.

My deepest appreciation goes to Dr. Naif Darwish for his encouragement during the early stages of my thesis. Also, I thank the college of Engineering and the Chemical Engineering Department for financially supporting me through the Graduate Teaching Assistantship.

Special thanks go to my thesis committee members, Dr. Zarook Shareefdeen and Dr. Kazi Fattah for providing useful remarks in the early stages of my thesis.

Finally, my heartfelt gratitude goes to my beloved parents and dear siblings for their love and continuous support.

Dedication

To my beloved family

Abstract

Synthetic dyes are commonly found in industrial wastewater due to their wide application as colorants in the textile, paper, food, leather and plastic industries. Among the various treatment methods, adsorption is generally considered to be the most efficient method for quickly lowering the concentration of dissolved dyes in an effluent. In recent years, there has been great interest in the use of Metal Organic Frameworks (MOFs) to remove dyes from contaminated water because of their diverse porous structures, high surface areas, and chemical tunability. In this thesis, the removal of methyl orange (MO) from aqueous solutions was investigated in batch and continuous setups using three MOFs, namely, Fe-BTC, Cu-BTC, and ZIF-8. The experimental results showed that at the same MO initial concentration (15 mg/L) and the same dosage (100 mg), Fe-BTC had the highest removal efficiency of 91%, followed by ZIF-8 (63%), and finally Cu-BTC (35%). Furthermore, pH effect experiments showed that Fe-BTC maintained consistent adsorption capacity over a wide range of pH suggesting that it could be a good candidate for dye removal from wastewater. The equilibrium study revealed that the experimental data could be best described by the Langmuir isotherm. The calculated maximum monolayer adsorption capacities were 100.3, 105, and 114 mg/g for Fe-BTC compared to 7.56, 5.62, and 4.65 mg/g for ZIF-8 at 298, 303 and 313 K, respectively. The calculated thermodynamic parameters indicated that the adsorption process was endothermic in the case of Fe-BTC ($\Delta H°$ was 16.86 kJ/mol) and exothermic in the case of ZIF-8 ($\Delta H°$ was -9.94 kJ/mol). In the continuous setup, a fixed-bed column was packed with Fe-BTC to study the performance of MO adsorption. The influent MO solution concentration was 15 mg/L, and the influent flow rate was 4.5 mL/hr. The adsorption performance was investigated at two different bed heights (0.75 and 1.5 cm). The results showed that as bed height increased the breakthrough time increased (20.0 hr at 0.75 cm to 46.2 hr at 1.5 cm). The bed maximum adsorption capacity also increased from 20.2 to 21.6 mg/g. The experimental data were found to best fit the modified dose response model (R^2>0.99).

Search Terms: ***Adsorption; Dyes; Methyl orange; Metal organic frameworks (MOFs); Fe-BTC; Cu-BTC; ZIF-8***

Table of Contents

List of Figures

List of Tables

Chapter 1. Introduction

1.1 Overview

Micropollutants are contaminants in wastewater such as pharmaceuticals, pesticides, detergents, endocrine disrupting chemicals, and organic dyes. These contaminants are becoming the focus of scientific research efforts due to their potential risks to both human and aquatic environment [1]. Usually, micropollutants are not covered by existing water quality regulations due to their lower concentrations (i.e., ng/L up to μg/L) but are thought to be potential threats to environmental ecosystems [2]. The discharge of treated effluent from wastewater treatment plants (WWTPs) is a major pathway for the introduction of micropollutants to surface water [3]. The main reason micropollutants are released to the environment through sewage discharge is that they are chemically stable and not completely biodegradable. Therefore, they cannot be removed with conventional wastewater treatment technologies. Consequently, these contaminants may end up in the aquatic environment becoming threats to wildlife and may eventually end up in the groundwater [3].

A major example of micropollutants is organic dyes. Organic dyes are a class of pollutants that are commonly found in industrial wastewater due to their wide application as colorants for textiles, papers, food, and as imaging agents [4]–[6]. It is predicted that the production of pigments and dyes will grow to reach 9.9 million tons and $26.53 billion globally by 2017, motivated by the growth in key end-use industries [7]. Of such a huge production, the exact amount that end-up being discharged into the environment is not exactly determined. However, it is reported that 10-15% of the used dyes enter the environment through wastes [8], [9].

Dyes from industrial effluents are problematic not only because their presence in wastewater introduces high levels of chemical and biological oxygen demand (COD and BOD) and total suspended solids (TSS), but also for their color, which is an immediate visual indication of water pollution. Dyes are also difficult to be biodegraded and photodegraded because they usually have synthetic origins and complex aromatic compounds which make them very stable to light and oxidation [10], [11]. Also, the presence of even very low concentrations of dyes in water reduces light penetration through the water surface, which may affect photosynthetic activity in aquatic life, and

may also be toxic to some aquatic life due to the presence of aromatics and metals in them [12], [13]. Therefore, dye wastewater needs to be treated for the sake of protecting human health and the environment.

WWTPs act as primary barriers against the spread of micropollutants. In developed countries, where discharge to the environment is highly regulated, industrial effluent usually receives at least pretreatment if not full treatment at the plants themselves to reduce the contaminants load, before discharge to the sewer. In developing countries, however, the same does not always apply, where industrial effluents usually enter the sewer – if it exists – or even the receiving water body without pretreatment. In general, wastewater undergoes three main processes in Sewage Treatment Plants (STPs). These are primary, secondary, and tertiary.

Primary treatment consists of coagulation/flocculation and primary sedimentation. Coagulation is a process for combining small particles into larger aggregates (flocs) and for adsorbing dissolved organic matter on to particulate aggregates so that these impurities can be removed in subsequent solid/liquid separation processes which is the primary sedimentation [14]. To achieve this, a coagulating agent, for example, aluminum sulfate [$Al_2(SO_4)_3$], ferric Sulfate [$Al_2(SO_4)_3$], ferric chloride [$FeCl_3$] or lime [$Ca(OH)_2$] is added to destabilize colloidal particles by charge neutralization and promoting collision between neutralized particles, resulting in cohesion, floc growth, and eventual sedimentation [15]. Following coagulation/flocculation is primary sedimentation or primary clarification where suspended agglomerated solid particles can settle at the bottom and are removed as primary sludge for further processing, while lighter particles float to the surface and leave with primary treated water to the next process [16], [17]. Dyes as an example of micropollutants cannot be removed in this process since they cannot be settled by gravity; hence, they are discharged downstream to the next process, which is secondary treatment.

Secondary treatment usually referred to as biological treatment, is used to convert remaining dissolved and colloidal organics from primary treatment into microbial solids. Secondary treatment is typically performed by microorganisms like bacteria and protozoa in a managed aerobic or anaerobic conditions, where they consume biodegradable soluble organic contaminants in either fixed or suspended

growth systems to convert them into water, carbon dioxide (CO_2), and energy for their growth and reproduction to form cells of biological solids [16], [17]. The resulting microbial mass is then removed by a secondary sedimentation unit, creating a secondary sludge. Similar to the primary treatment, dyes cannot be removed in this process because of their resistance to biodegradation and therefore are released with the secondary treated wastewater. In addition, it has been reported that aerobic biological methods are ineffective in textile wastewater treatment as no significant color removal can be obtained for most of the dyes [18].

The third stage of wastewater treatment is tertiary treatment or sometimes referred to as advanced wastewater treatment. The purpose of this stage is to further improve the effluent quality before discharge to the receiving environment. Single or more than one tertiary treatment process may be used. This depends on several factors such as standards and regulations and the intended use of the treated water, whether it is discharge to surface water, irrigation, groundwater recharge, or agricultural purposes. Several techniques are utilized at this stage in Sewage Treatment Plants (STPs) to remove organic dyes from wastewater before discharge, or they can be implemented separately at the plants generating these pollutants before discharge in the sewage network to reduce the load on STPs. In the literature review section, a brief overview of these techniques, advantages, and disadvantages, and efficiencies of each technique will be presented. In addition, the current research on the potential of metal organic frameworks as a promising emerging technique to remove organic dyes will be discussed.

1.2 Thesis Objectives

The main objective of this thesis is to investigate Metal Organic Frameworks (MOFs) as a promising adsorbent for the removal of methyl orange from aqueous solutions. The following tasks are addressed.

1. Study the removal efficiency and adsorption capacity of methyl orange using three MOFs (Fe-BTC, Cu-BTC, and ZIF-8) under the following conditions: 100–200 mg dosage; 5–15 mg/L initial concentration; 2–12 pH; and 25–40 °C.

2. Fit the experimental data to kinetic and isotherm equilibrium models, and calculate the following thermodynamic parameters: Gibbs free energy (ΔG°); enthalpy (ΔH°); and entropy (ΔS°).
3. Perform characterization tests (XRD, SEM, FTIR, and TGA) on the MOFs samples before and after adsorption to determine the effects of adsorption on the structure of the MOFs and confirm their stabilities.
4. Employ full factorial experimental design to study the main factors and their interactions that affect the removal efficiency of methyl orange.
5. Build a bench-scale fixed-bed column, packed with Fe-BTC for the removal of MO from aqueous solutions in a continuous setup, and study the breakthrough performance when the bed heights are 0.75 and 1.5 cm while maintaining the flow rate at 4.5 mL/hr and feed concentration at 15 mg/L.
6. Fit the fixed-bed data to kinetic breakthrough models and determine the parameters related to each model.

1.3 Thesis Organization

The thesis is organized as follows:

- Chapter 2: Literature review related to the classification of dyes and dye removal technologies.
- Chapter 3: A batch study on the adsorptive removal of methyl orange from aqueous solutions.
- Chapter 4: A dynamic study of fixed-bed column adsorption of methyl orange using Fe-BTC.
- Chapter 5: Conclusions and recommendations.

Chapter 2. Literature Review

In this chapter, the relevant literature pertaining to classification of dyes and dye removal technologies in general such as biological-based oxidation, ozonation, chemical oxidation, photocatalytic oxidation, membranes, ion exchange, and adsorption materials (e.g., activated carbons and zeolites) will be reviewed. In more details, metal organic frameworks (MOFs) as a new emerging technology for dye removal using adsorption. Classification of dye section will introduce two types of classifications of dyes: chemical structure based and application methods based classification. In addition, the section related to methods of dye removal is divided into three main subsections, namely, biological treatment, chemical treatment (ozonation, oxidation, and photocatalytic oxidation), and physical treatment (membrane, ion exchange, and adsorption). The MOFs review section is intended to provide a comprehensive overview of MOFs including material characteristics, structural features, applications, and adsorption capacities.

2.1 Classification of Dyes

Dyes are essentially chemical compounds that are applied to surfaces or fabrics to give them color. The majority of dyes are synthetic and complex in nature. They are also required to be resistant to a variety of factors such as temperature, chemicals, weather and action of detergents. It is essential to have a classification of dyes due to huge increase in kind and number of colorants. In general, dye molecules have two functional groups which are chromophores and auxochromes. Chromophores, responsible for the color of the dye, are delocalized electron systems with a conjugated double bond which are normally electron-withdrawing groups such as –N=N–, –N=O, and $–NO_2$ groups. Based on these chromophores, dyes are classified as azo, anthraquinone, indigoid, phthalocyanine, nitro, nitroso and triarylmethane (triphenylmethane). On the other hand, auxochromes, responsible for the intensity of the color, are electron-donating substituent such as $–NH_2$, –COOH, and –OH. In addition, dyes can be classified according to application methods as follows: acid, basic, reactive, direct, disperse, and vat. At the same time, acid, basic, reactive, and direct are classes of dyes that are water soluble. However, disperse dyes have very low water solubility, and vat dyes are water-insoluble [19].

Throughout this thesis work, Methyl Orange (MO) (or C.I. Acid Orange 52) will be deliberated as an example of dye pollutants. The subsequent sections in the literature review will present removal methods of dyes in general and MO in particular where related data is available. MO is a common dye usually used as pH indicator in titrations. In basic solutions, the dye has azo structure while in acidic solutions, it has quinoid structure. Figure 1 shows the chemical structure of MO under both acidic and basic conditions. Under acidic conditions, the dye tends to have more red color, whereas under basic conditions it tends to be more yellow in color.

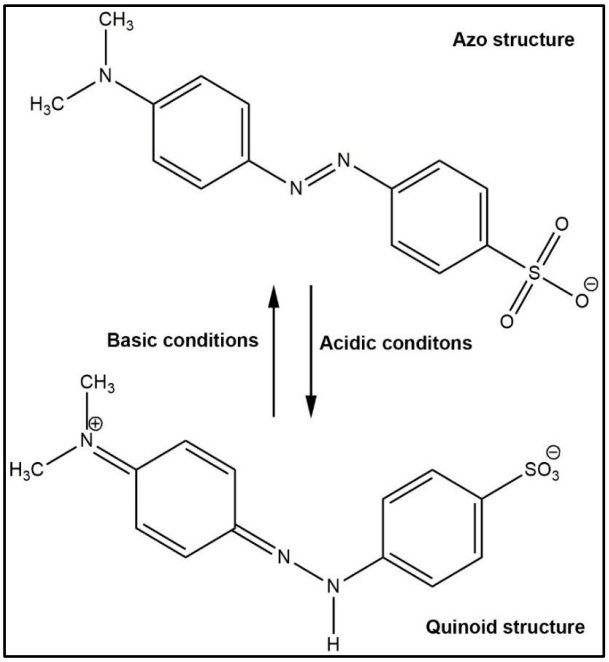

Figure 1: Structural forms of methyl orange under acidic and basic conditions.

2.2 Methods of Dye Removal

Since the presence of dyes in wastewater effluent is highly undesirable, several methods have been investigated to remove dyes from wastewater before discharge to the environment. However, there is no single standard methodology/treatment procedure used for all types of wastes. Furthermore, despite the availability of many techniques to remove dye pollutants from wastewater, each of these methods has inherent limitations, and all of them have advantages and disadvantages. The technologies can be divided into biological, chemical, and physical.

2.2.1 Biological treatment. Biological treatment is the most widely used in wastewater treatment. In this method, microorganisms metabolize the biodegradable organic compounds to be converted into water, carbon dioxide (CO_2), and energy for their growth and reproduction of biomass. In addition, biological treatment has several advantages such as inexpensive, low running cost and no toxic byproducts. The process can be aerobic (in the presence of oxygen), anaerobic (without oxygen) or combined aerobic–anaerobic using fixed or suspended growth systems. In fixed systems, microorganisms attach to a biofilm surface while wastewater flows over it. In suspended growth system, on the other hand, microorganisms are suspended and mixed in the wastewater. Although biological treatment methods are usually less expensive than physical and chemical treatment options, they often have huge limitations, as most of the dyes were observed to be non-biodegradable under aerobic conditions, or require long retention times to achieve decent removal efficiencies [20]. For instance, reactive azo dyes usually have low biodegradability index ($BOD_5/COD < 0.1$), indicating that these dyes are resistant to conventional biological treatment methods [19]. This is expected since the majority of synthetic dyes are chemically stable and resistant to microbial assault. Nevertheless, the potential of anaerobic treatment applications for the degradation of several synthetic dyes has been demonstrated. Studies reported that reduction under anaerobic conditions can convert azo dyes to aromatic amines [21]. Although aromatic amines are likely to be harmful, they can be biologically degraded under aerobic conditions. As this process is just a partial degradation process, anaerobic treatment is not sufficient as a final wastewater treatment step. Beside the time of treatment may take a few days for high removal, the removal efficiency may vary for each type of azo dyes. One research group investigated the degradation of textile dye using bacterial strains isolated from textile mill effluent. The results showed that the highest decolorization percentage for one of the dyes (Pink) was 93% after 5 days. Another dye was used (Green), and the highest decolorization percentage after 5 days was 85% [22].

In general, the factors that affect decolorization are the concentration of dyes, initial pH and temperature of the effluent. Although biological treatment has attractive advantages such as being cost-competitive, and suitable for a variety of dyes, the main disadvantages are low biodegradability of the dyes (as dyes are designed to be stable and permanent), complexity of design and operation, inability of microorganisms to

cope up with large volumes of wastewater, larger foot-print, and longer times required for decolorization processes, hence making it unattractive choice for the removal of dyes from effluents on a continuous basis [23].

2.2.2 Chemical treatment. Chemical processes often involve chemical oxidation where chemical reagents (oxidizing agents such as hydrogen peroxide (H_2O_2) and ozone (O_3), or energy-activated catalysts (such as TiO_2 or ZnO) are used

2.2.2.1 Ozonation. Ozone is a powerful oxidant with a relatively short lifetime. Ozone reacts with organic dyes either through direct ozone assault or indirect free radical assault. Ozonation method is favorable for soluble dyes as ozone usually reacts with the double bond which is responsible for coloration, and subsequently, oxidation takes place [24], [25]. The advantage of ozonation is that it does not result in increased volume of wastewater, nor sludge production due to the application of ozone in gaseous phase [26]. Preethi et al. [25] reported the use of ozone to treat direct brown dye as well as tanning wet process effluents. It was found that the ratio of biological oxygen demand to chemical oxygen demand (BOD_5/COD) increased by more than 0.4 within 30 min of ozonation. Furthermore, the maximum COD removal efficiency for direct brown dye effluent and tannery effluent under optimum operating conditions after 80 min of ozonation were 92 and 70%, respectively. Hence, an increase in BOD_5/COD ratio to above 0.4 indicates the suitability of ozonation as a pre-treatment method for subsequent biological treatment methods to enhance their biodegradation efficiency. Sundrarajan et al. [27] studied the ozonation for reactive dyes removal and found that color removal of the effluent can be achieved in 5 min of contact time for yellow and blue shades at an ozone consumption of 37.5 and 36 mg/L, respectively. As a result, they suggested that ozonation is efficient in decolorization of exhausted dye bath effluents containing conventional reactive dyes [27].

Ozonation can also be combined with other methods. For example, Zhang et al. [28] studied the decolorization of methyl orange by ozonation in combination with ultrasonic irradiation. The study showed that ozonation in combination with ultrasonic irradiation has a synergistic effect on the decolorization of methyl orange, where the synergistic effect was more significant as the system temperature was raised due to the heat effect of ultrasonic irradiation. Also, the effect of pH on the decolorization was insignificant when initial pH ranged from 5.5 to 9.7 (all initial pH values investigated

while keeping dye concentration, ozone concentration, ozone gas flow rate and ultrasonic power constant gave the same rate constant, which was 0.24 min^{-1}), whereas the decolorization rate increased with increasing ultrasonic power, ozone gas flow rate, and gaseous ozone concentration, respectively, due to improved mass transfer under the experimental conditions. However, the decolorization rate decreased with the increasing initial dye concentration. In another study, Ge et al. [29] investigated the degradation of methyl orange by ozone in the presence of ferrous and persulfate ions ($O_3/Fe^{2+}/S_2O_8^{2-}$) in a rotating packed bed. The study indicated that the degradation rates increased from 58% to 85% with an increase in pH from 1 to 4.

Even though ozone is able to decolorize soluble dyes such as reactive and acid dyes, it reacts much slower for non-soluble dyes. In addition, dyes discharge varies among different industries and may contain other pollutants other than dyes. For example, textile effluent contains other pollutants such as inorganic salts, surfactants that have a possibility to react with ozone which may as a result increase ozone consumption.

2.2.2.2 Oxidation. Oxidation is a method by which dye wastewater is treated using oxidizing agents. Chemical oxidation is used to degrade the organic dyes due to its effectiveness in destroying organic compounds that are non-biodegradable, toxic, or inhibitory to microbial growth. This method is used to partially or completely degrade the dyes.

Chlorine (applied as gaseous chlorine) is one of the oxidizing agents used, and may also be applied as calcium hypochlorite ($Ca(ClO)_2$) or sodium hypochlorite (NaOCl). Water soluble dyes are decolorized by hypochlorite, but water-insoluble dyes are resistant to decolorization in this process. Although oxidation by chlorine gas is a low-cost methodology for decolorizing dye wastewater, it is limited by the unavoidable side reactions and the production of organochlorine compounds including toxic trihalomethane, which results in increasing the absorbable organic halogens content of the treated water [23].

Hydrogen peroxide (H_2O_2) is another oxidizing agent that can be used to decolorize dye effluents. H_2O_2 is a strong oxidizing agent and can be used for bleaching paper besides other uses. Although H_2O_2 is a strong oxidizing agent, it is, however, pH-

dependent and produces sludge [23]. Also, the use of H_2O_2 alone can cause the reactions to occur at a slow rate, and catalysts such as ferrous iron ($FeSO_4$ or Fenton's reagent) at acidic pH are generally required [19]. The use of Fenton's reagents is generally considered to be effective in decolorizing of both soluble and insoluble dyes, though some dyes like vat and disperse were found to be resistant to it. Hameed and Lee [30] conducted an experimental study on the removal of malachite green in aqueous solution through Fenton reaction in homogenous condition. They reported that color removal of 20 mg/L dye could attain up to 99% after 60 min under optimum conditions. However, the final concentration of iron in bulk solution after treatment induced secondary pollution. In another study, Daud et al. [31] introduced a heterogeneous Fenton catalyst. They found that color removal of 50 mg/L Acid Red 1 was 99% after 150 min under optimum conditions. This process received more attention as compared to homogeneous Fenton process due to the easier separation of heterogeneous catalysts from liquid products. The main disadvantage of the Fenton process is that it involves significant sludge generation; it is usually effective within narrow pH range, and takes longer reaction times.

2.2.2.3 Photocatalytic Oxidation (Photodegradation). Photocatalytic oxidation (or photodegradation) process is defined as the use of semiconductor metal oxide as catalyst including: titanium dioxide (TiO_2), zinc oxide (ZnO), Stannic Oxide (SnO_2), Zirconium dioxide (ZrO_2), Zinc Sulfide (ZnS), or Cadmium Sulfide (CdS) in the presence of energy-activation source (UV irradiation). The process is found suitable for a wide range of dyes including direct, reactive, vat, and disperse dyes.

The degradation of dyes depends on several parameters such as pH, catalyst concentration, and dye concentration. A study by Kansal et al. [32] on the degradation of methyl orange (MO) and rhodamine (R6 G) utilizing various semiconductors such as (TiO_2), (ZnO), stannic oxide (SnO_2), zinc sulfide (ZnS) and cadmium sulfide (CdS) has been carried out. The researchers found that the maximum decolorization (more than 90%) of dyes occurred with ZnO catalyst. The maximum adsorption of MO was noticed at pH 4, and of R6G at pH 10. The percentage reduction of MO and R6G was estimated under UV/solar system, and it was found that COD reduction takes place at a faster rate under solar light as compared to UV light. In the case of R6G, highest decolorizing efficiency was achieved with a lower dose of catalyst (0.5 g/L) than MO

(1 g/L) under similar conditions. Moreover, the study demonstrated that the performance of a photocatalytic system employing ZnO/solar light was better than ZnO/UV system. Also, Raliya et al. [33] investigated the photodegradation of methyl orange (MO) with different oxide nanomaterials acting as photocatalysts under visible light. Titanium dioxide (TiO_2), zinc oxide (ZnO), and graphene oxide (GO) were applied for the photocatalytic degradation of the dye. Accordingly, they stated that with MO initial concentration of 50 mg/L the degradation efficiency decreased in the following order: ZnO degraded the most (40%), followed by TiO_2 then GO for a total reaction time of 120 min.

Since UV light source is energy intensive, it is desired to develop methods to sensitize the photocatalyst using visible range in solar light (only 4% of solar light is in the UV range compared to 43% is in the visible range) [19]. Doping is an effective approach to extend the optical absorption range from UV to visible region in order to utilize sunlight instead of UV light. Table 1 presents a summary of research studies to develop new alternatives to sensitize TiO_2 photocatalyst.

Table 1: Summary of research findings for photocatalytic degradation of dyes.

Light Source	**Photocatalyst**	**Important Findings**	**Reference**
Solar light	TiO_2 immobilized on poly-3-hydroxybutyrate	• Textile wastewater with 14500–21000 mg/L COD was treated to 80 mg/L and the color was 100% removed.	[34]
Daylight	Iron (Fe) and cobalt (Co) doped TiO_2	• 100 mg/L Malachite Green (MG) was degraded to 98% using 2 g/L Fe-TiO_2. • 100 mg/L MG was degraded to 86% using Co-TiO_2.	[35]
Visible light	Titanium (Ti) and cobalt (Co) doped silicates (SBA-15)	• 25 mg/L Methylene Blue (MB) was degraded (93% in 5 h) using 3 g/L of 50 Ti-SBA-15. • 10 mg/L MB was degraded (74% in 6 h) using 2 g/L of 40 Co-SBA-15.	[36]
Fluorescent lamps	Glass coated TiO_2 thin film	• 10 mg/L MB, MO, Indigo Carmine, Chicago Sky Blue 6B and Mixed dyes to 90.3, 98.5, 92.4, 60.3, 70.1%, respectively.	[37]

The advantage of this process is that it provides the possibility of complete mineralization of dyes within a relatively short period, produces no sludge, and provides a considerable reduction of COD. On the other hand, the disadvantage of this process is the limitation of light penetration in a water medium, fouling of catalysts, and the problem of fine catalyst separation from the treated liquid. Additionally, they are quite expensive especially for the small-scale sector of developing countries. As a result, this method is generally limited to effluents with low concentration or as a polishing process only.

2.2.3 Physical treatment. There are various physical methods that can be used to remove dyes. These include membrane filtration, ion exchange, and adsorption.

2.2.3.1 Membrane filtration. Membrane filtration involves the passage of the fluid through a porous medium to remove the dye in the effluent. This method is usually used after biological treatment. Membrane filtration methods are based on semi-permeable membranes. They include (in decreasing membrane pore size order) microfiltration (MF), ultrafiltration (UF), nanofiltration (NF), and reverse osmosis (RO), respectively. The membrane is often made of a thin layer of polymer or ceramic. Membrane filtration is a quick and effective process for the removal of all types of dyes.

For example, RO has been successfully employed for recycling water, and the produced effluent was close to pure water [38]. However, the main disadvantages are significant energy consumption, high operating pressure, high cost of the membrane, short membrane life (caused by membrane fouling) which make them unattractive for treating dye wastewater [23].

2.2.3.2 Ion exchange. Ion exchange is a process wherein an ion from solution is exchanged for a similarly charged ion attached to a fixed solid resin. Since ion exchange can only be implemented for the removal of undesirable anions and cations from wastewater, it can only remove both cationic (basic dyes) and anionic (acid, direct, and reactive dyes) effectively.

The removal of non-ionic dyes (disperse dyes) is very poor. Once ion exchange resin is saturated, it needs to be regenerated before reuse, so, the use of an organic solvent to regenerate spent ion exchange resin is unavoidable [26].

The advantages of ion exchange treatment are the recovery of resin upon successful regeneration, reclamation of solvent after reuse, and the effective removal of soluble dyes. The main drawback for the success of the ion exchange method is the lack of effectiveness in removing several types of dyes. In addition, large-scale implementation of this method is challenging, anion/cation exchange resins are expensive, and regeneration of these resins is expensive [19].

2.2.3.3 Adsorption. Adsorption technology is an equilibrium separation process that has significant potential in wastewater treatment applications. The adsorption process has been widely used not only for color removal, but also has been applied for the removal of certain classes of chemical contaminants that are practically unaffected by conventional biological treatments, and odor control [23], [39]. The term adsorption refers to the accumulation of a substance from a liquid or gas phase on the surface of a solid. The substance from the liquid or gas phase is referred to as adsorbate, and the solid upon which accumulation takes place is called adsorbent. If the interaction in the adsorbent/adsorbate interface is physical in nature, the adsorption is referred to as physical adsorption (or physisorption). Physical adsorption is characterized by the weak attraction between the adsorbent and adsorbate (Van der Waals attractive forces), and thus considered reversible in most cases [40]. On the other hand, if the interaction in the adsorbent/adsorbate interface is due to chemical bonding, the adsorption is referred to as chemical adsorption (or chemisorption). Chemical adsorption is characterized by the formation of strong bonding (or chemical association) between the molecules of the adsorbate and the adsorbent, which is generally due to the exchange of electrons. Therefore, it is considered irreversible in most cases [40].

For water treatment and reuse, adsorption is considered better than other treatment methods in terms of flexibility, simplicity of design, initial cost, insensitivity to toxic contaminants and ease of operation [39]. Furthermore, adsorption does not produce harmful substances [41]. The factors that affect adsorption efficiency are adsorbent characteristics, initial concentration of adsorbate material, temperature, pH, and contact time [41]. There are many physical adsorbent materials that have been considered for removal of dyes from wastewater such as, activated carbon [42], zeolites [43], and metal organic frameworks (MOFs) [44]. However, any suitable adsorbent for any water/wastewater treatment applications should satisfy several basic criteria to

compete with present technologies. These include: 1) porous structure (high adsorption capacity); 2) good adsorption/desorption kinetics; 3) water stability 4) repeatable large-scale synthesis.

2.2.3.3.1 Activated carbon (AC). Activated carbon (AC) is the most widely used carbon-based adsorbent in different industrial applications. There are other varieties of carbon-based adsorbents such as graphenes and carbon nanotubes (CNTs), however, activated carbons remain the most popular for the removal of pollutants from wastewater and the most investigated adsorbents in the literature. The effectiveness of adsorption on ACs for the removal of a large number of dyes has made it an ideal alternative to other expensive treatment options [39]. AC is usually prepared from carbon-containing biological material such coal and lignite, agricultural solid waste and by-products (like pine sawdust, coconut shells, and chitosan), or industrial by-products (such as metal hydroxide sludge, activated sludge, sewage sludge, coal fly ash). Many of these sources are considered cheap sources which give AC huge advantage over other adsorbents in terms of the low cost of raw materials. The preparation of AC from these sources generally consists of two major steps: carbonization and activation. Activation methods can either be physical or chemical. In general, physical activation requires high temperature and longer activation time as compared to chemical activation. On the other hand, in chemical activation, the AC requires a thorough washing due to the use of chemical agents. Figure 2 shows a general schematic diagram of the process of producing activated carbon.

Activated carbon is available in two main forms: powdered activated carbon (PAC) which is suitable for batch processes, and granular activated carbon (GAC), more adaptable to continuous contacting in fixed-bed columns. The use of PAC presents some challenges due to the need to separate the adsorbent from the fluid after use, whereas the use of GAC in continuous operation does not need separating the adsorbent from the bulk fluid [23].

Many of the low-cost adsorbent derived from carbonaceous materials have been tested and proposed for dye removal. For example, Chen et al. [10] investigated the adsorption of MO on activated carbon derived from Phragmites australis (a type of grass found in wetlands). They reported that the removal efficiency of MO increased from 30% to 100% when increased the adsorbent dose from 0.01 to 0.08 g (volume of the

MO solution was 100 mL with an initial concentration of 50 mg/L, and the temperature was 25 °C). The increase in dye removal percentage can be attributed to the increased available sorption surface and the availability of more adsorption sites. Also, they studied the effect of the initial concentration of MO solution on removal efficiency and found that the adsorption capacity at equilibrium increased from 351 to 438 mg/g with an increase in the initial MO concentrations from 150 to 250 mg/L. In addition, AC-based composites have been investigated for the removal of dyes. Do et al. [45] studied the adsorption of MO on powdered activated carbon (PAC) combined with Fe_3O_4 nanoparticles (PAC/ Fe_3O_4 composite). Different composites were prepared by varying the percentage of Fe_3O_4 in the composite material (5, 10, 25, and 30 wt.%). They reported highest adsorption capacity of 212 mg/g for the 10 wt.% composite, and lowest adsorption capacity of 182 mg/g for the 30 wt.% composite (specification of the experiment are: 0.1 g of adsorbent and 50 mL of MO solution at a concentration of 500 mg/L and 30 °C). Table 2 presents a summary of the adsorption capacities of MO on different types of adsorbents.

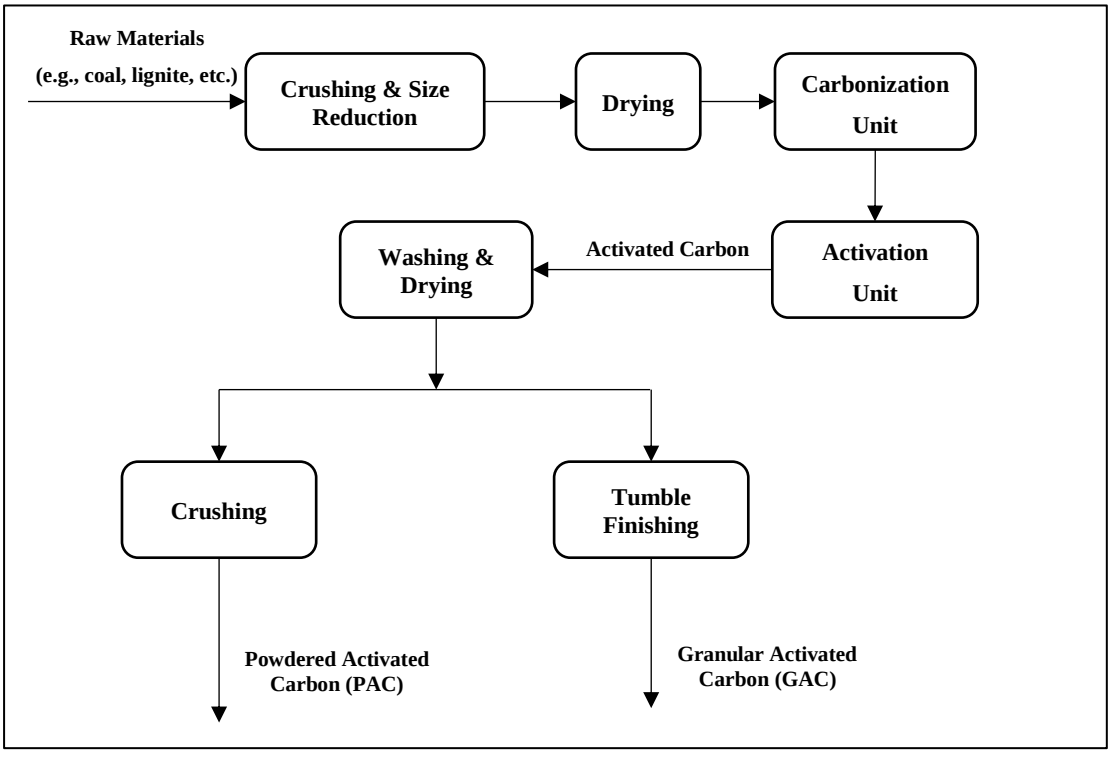

Figure 2: Schematic diagram of the process of producing activated carbon.

Table 2: Adsorption capacities of MO on some adsorbents.

Adsorbent	**Maximum adsorption capacity, q_m (mg/g)**	**References**
De-oiled soya	16.7	[46]
Bottom ash	3.6	[46]
Modified montmorillonite	24	[47]
Chitosan/Alumina	32.7	[48]
Multi-walled carbon nanotubes (MWNTs)	52.86	[49]
Calcium alginate/MWCNTs	12.5	[50]
Chitosan/Fe_2O_3/MWCNTs	66.9	[51]
Alkali-Activated MWCNTs	149	[52]

Although ACs are good materials for the removal of different types of dyes in general, it has been found that adsorption on AC is not usually selective. Furthermore, regeneration of AC is cost and energy intensive process. Once AC has been exhausted, it needs to be regenerated for further use, and several methods can be utilized such as thermal, chemical, or electrochemical, for this goal. Additionally, the regenerated AC may have a slightly lower adsorption capacity after each regeneration cycle [39]. Another problem of using AC in water treatment is that it can be an excellent place for microorganisms to grow. The conditions that promote microorganisms' growth arise when the AC adsorbent becomes saturated with organic contaminants which can be a food source for different microorganisms [53].

2.2.3.3.2 Zeolites. Zeolites are porous solids with well-defined crystalline structures. They can be found naturally or fabricated synthetically. Zeolites generally consist of silicon, aluminum, and oxygen. The primary building units in the structure of zeolites are single TO_4 (T = Si, Al) tetrahedral, with Aluminum or Silicon atom in the center and oxygen atoms at the corners.

These tetrahedral units are linked together at their corners in a periodic array leading to various connectivities. These primary building units are connected to form secondary building units (SBUs), and the repetition of these SBUs in different topological connections give various types of zeolites. The presence of the alumina

atom in the conventional zeolites based on silicate frameworks leads to a negative charge on the framework, with exchangeable cations within the pore structure, therefore, zeolites exhibit ion exchange properties [23]. In addition, zeolites can incorporate other atoms (such as Ti, B, Ni, Cr, Fe, Co, and Mn) in the framework in place of Si atoms [54]. These structural and chemical varieties have given zeolites many applications spanning adsorption, ion exchange, and catalysis [55].

Several zeolites have been investigated as potential adsorbent for the removal of dye from wastewater. For example, Alpat et al. [56] studied the adsorption of Toluidine Blue O (TBO) on the natural zeolite clinoptilolite. The results showed that the maximum adsorption capacity of clinoptilolite for TBO was 2.1×10^{-4} mol/g (64 mg/g) at a solution pH of 11. Another study done by Wang and Ariyanto [57] on the adsorption of malachite green onto clinoptilolite zeolite has shown that the adsorption capacity of malachite green at 30 °C and pH 6 was 5×10^{-5} mol/g (18 mg/g). It can be seen from these results that clinoptilolite is not suitable for the removal of dyes due to low adsorption capacities. These results may be attributed to the highly hydrophilic character of zeolites, which may explain why zeolites have not found broad application as adsorbents in water treatment until now.

2.2.3.3.3 Metal organic frameworks (MOFs). Metal organic frameworks (MOFs) are hybrid organic-inorganic solid materials with an infinite uniform crystalline structure. The organic-inorganic network consists of metal ions (or metal clusters) such as Al^{3+}, Cr^{3+}, Cu^{2+}, or Zn^{2+} and organic ligands (referred to as linkers) such as carboxylate, pyridyl connected via coordination [58]. They are sometimes named porous coordination polymers (PCPs).

The structure of MOFs consists of two secondary building units (SBUs) which are the organic linker and the metal cluster. The organic linker can be ditopic (has two types of coordinative functionalities), tritopic (three types) or polytopic (more than three types). The metal cluster SBU, on the other hand, may be a finite polyatomic inorganic cluster with two or more metal atoms or an infinite inorganic unit such as an infinite periodic rod of metal atoms [59]. Common examples of the organic SBUs are BDC (BDC = benzene-1,4-dicarboxylic acid), BTC (BTC = benzene-1,3,5-tricarboxylic acid), and 4,4'-bipy (4,4'-bipy = 4,4'-Bipyridine). Inorganic SBUs are

either single metal ions or metal cluster that can be obtained from hydrated metal salts. They have various coordination modes (e.g., octahedral, tetrahedral, or square planar).

Moreover, there are special types of MOFs such as zeolitic imidazolate frameworks (ZIFs), which have a topology similar to zeolites. Like zeolites, ZIFs have tetrahedrally-coordinated transition metal ions (such as Zn, Fe, and Cu) connected by imidazolate linkers in angles similar to the 145° Si-O-Si angle in zeolites [60]. Generally, MOFs have some exceptional and unique properties, such as extremely high internal surface area (1000 – 7000 m^2/g) [61], [62] , high thermal stabilities (ranging from 250 to 500 °C), low density (the lowest density reported is 0.126 g/cm^3) [63], large pore volumes (ranging from 1.1 to 4.4 cm^3/g) [61], [62], permanent porosities and flexible frameworks that make them different from other conventional porous solids [64].

One of the attractive features of MOFs is that they are tunable. Unlike activated carbon and zeolites, a systematic approach can be applied to design MOFs based on changing the nature of organic linker and/or changing the connectivity of the metal cluster and how the building blocks come together to form a structure with specific pore size and shape. For example, by only changing the length of the organic ligands with the same metal species, the new pore size of the corresponding frameworks can be obtained, depending on the length of the ligands [65]. Also, several analogous MOFs can also be prepared from identical ligands and different metallic components [65]. This remarkable and easy tunability of MOFs is a key characteristic that distinguishes these materials from traditional porous materials. In addition, it allows the optimization of the pore dimension and surface properties within metal-organic frameworks that were previously absent in zeolite materials [66]. As an example of the tunability of pore size in MOFs, Eddaoudi et al. [67] reported the synthesis of 16 MOF-5 ($Zn_4O(BDC)_3$) functionalized derivatives that were termed IRMOF-1 to IRMOF-16. These MOFs consisted of tetrahedral $[Zn_4O]^{6+}$ clusters connected by ditopic BDC^{2-} ligands to form a cubic three-dimensional network. For each IRMOF the functional organic ligand was changed. The synthesized IRMOFs displayed tunable pore spaces and pore functionality relative to the length of the functional group.

Another attractive feature of MOFs is water stability which is one of the important criteria of choosing a MOF for water treatment applications. Various MOFs

have been reported to be highly stable in water and suitable for water purification or adsorption in water. Several methods have also been reported to enhance water stability of MOFs such as fluorination, composite formation, and incorporating water repellent functional groups [68].

Since the 1990s, great attention has been raised to the potential of MOFs that exhibited in advanced technological applications. Examples of these applications include clean energy storage (e.g., hydrogen and methane) and adsorption/storage in gas and liquid phases (e.g., CO_2 capture and sequestration, liquid phase adsorption of various hazardous compounds). Clean energy storage and adsorption is a major application direction of MOFs attributing to their porous nature [69]. Drug delivery/biomedicine is another application of MOFs. In drug delivery, MOFs are used as vectors for drug delivery [70]. Very recently, MOFs have been used to encapsulate bio-macromolecules, where researchers addressed the insertion of biological structures into pre-formed MOF [71]. Furthermore, in catalysis, MOFs are highly attractive as heterogeneous catalysts due to their high surface area, tunable porosity, and diversity in metal ions/organic linkers. Luminescence, polymerization, and magnetism are also other potential applications of MOFs [68].

The first attempt to investigate the use of MOFs as an adsorbent in the removal of dyes was made by Haque et al. [72] They studied the adsorption of azo dyes onto MOFs in 2010 [72]. In the study, two typical highly porous MOF materials based on chromium-benzenedicarboxylates (Cr-BDC), namely MIL-53(Cr) and MIL-101(Cr) (MIL = Material of Institute Lavoisier) were investigated for the adsorption of methyl orange (MO) from aqueous solutions. The results of the study indicated that the adsorption capacity and adsorption kinetic constant of MIL-101 were greater than those of MIL-53 due to their higher porosity and pore size and that they were much higher than activated carbon (114, 57.9, and 11.2 mg/g respectively at 25°C) for the removal of MO. Since this study, several studies on the removal of different dyes using various MOFs as adsorbents have been reported.

In a different study, Haque et al. investigated the adsorption performance of methylene blue (MB) and methyl orange (MO) on an amino-functionalized MOF, NH_2-MIL-101(Al) [73]. The results indicated that the synthesized MOF exhibited higher adsorption capacity for MB than MO, and performed better than the non-functionalized

MOF, MIL-101(Al). However, recyclability of NH_2-MIL-101(Al) used to adsorb MO was possible, whereas attempts to recycle NH_2-MIL-101(Al) used to adsorb MB were unsuccessful.

Very recently, researchers attempted to synthesize MOF-based composite adsorbents to investigate their adsorption performance. For example, Wu et al. [74] synthesized an aluminum-based MOF/graphite oxide composite, MIL-68(Al)/GO, and explored its adsorption performance toward methyl orange (MO). The highest reported adsorption capacity was 400 mg/g at 25°C. Moreover, the researchers reported that the material can be used over a wide pH range and exhibited superior adsorption performance and regenerability for the adsorption of MO compared to the non-composite MOF material (MIL-68(Al)). Table 3 presents a summary of methyl orange adsorption capacities for different MOFs. Based on the previous appealing findings, it can be seen that MOFs have higher uptake capacities than ACs and zeolites. Furthermore, MOFs exhibit higher stability and regenerability than ACs and zeolites. Therefore, MOFs can be used as a promising adsorbent candidate for the removal of dyes from water samples.

Table 3: Methyl orange (MO) adsorption capacities over various MOFs.

MOF	**Temperature (°C)**	**Maximum adsorption capacity, q_m (mg/g)**	**References**
MIL-53(Cr)	25	57.9	[72]
MIL-101(Cr)	25	114	
ED-MIL-101(Cr)	25	160	
PED-MIL-101(Cr)	25	194	
NH_2-MIL-101(Al)	30	188	[73]
	40	192.1	
	50	198.6	
MOF-235	25	477	[75]
	35	448	
	45	501	
MIL-101 (six samples were prepared)	25	277.92 (sample with highest performance)	[76]
MIL-100(Fe)	30	1045.2	[77]
MIL-100(Cr)	30	211.8	
MIL-68(Al)	35	341.30	[78]

Chapter 3. Adsorptive Removal of Methyl Orange from Aqueous Solutions: Batch Study

In this chapter, a comparative study of MO removal using three MOFs (Fe-BTC, Cu-BTC, and ZIF-8) is reported. The effect of adsorption on the structure of the MOFs and the possible adsorption mechanism were investigated using various characterization techniques including FTIR, XRD, SEM, and TGA. Also, the effects of different operating parameters, such as contact time, adsorbent dosage, initial dye concentration, pH, and temperature on MO removal were investigated. In addition, the kinetics and equilibrium isotherms of adsorption were studied, and the thermodynamic parameters of MO adsorption were calculated. Finally, a 2^3 full factorial design was used to evaluate the importance of MOF type, dosage, and MO initial concentration.

3.1 Experimental Work and Methodology

3.1.1 Materials. Fe-BTC, Cu-BTC, and ZIF-8 were purchased from Sigma-Aldrich under trademark Basolite® F300, Basolite® C300 and Basolite® Z1200, respectively, and were used without further modifications. Iron 1,3,5-benzenetricarboxylate (Fe-BTC) is an iron-based MOF. It exhibits high catalytic activity for various reactions and has been successfully used in the liquid-phase separation of small organic compounds [79]. It was also used in the removal of As(V) from aqueous solutions [80]. Similarly, copper benzene-1,3,5-tricarboxylate (Cu-BTC or HKUST-1), first reported by Chui et al. [81] was one of the most frequently investigated MOFs for gas adsorption and storage [82], [83] and was used in the removal of methylene blue from aqueous solutions [84]. Additionally, 2-Methylimidazole zinc salt (ZIF-8) was reported to exhibit high thermal stability up to 400 °C and excellent chemical stability in water, alkaline solutions and organic solvents [60].

Meanwhile, MO is a well-known azo/anionic dye and is used in textile, printing, pharmaceutical and food industries [46]. Methyl Orange was purchased from LabChem (USA) as 0.1% (1000 mg/L) stock solution, and different concentrations were obtained by subsequent dilution using deionized water (PURELAB® Pulse, ELGA LabWater, UK). For pH adjustment hydrochloric acid (37%) and sodium hydroxide (98%) are used

to prepare 1.0 M of HCl and NaOH aqueous solutions. For MOFs regeneration, ethanol (99.8%, Sigma-Aldrich) is used as the eluent.

3.1.2 Adsorption experiments. Aqueous MO solutions with different concentrations are prepared by successive dilution of the stock solution with deionized water. The concentration of methyl orange was determined by measuring the absorbance (at λ = 464 nm) of the solutions with a UV-Vis spectrophotometer (Evolution 60s, USA; resolution > 1.5 at 1.0 nm spectral bandwidth), and then calculating the concentration according to a calibration curve. The calibration curve was obtained from the spectra of the standard solutions (1–30 mg/L) at a pH of 6. (Figure 3). The Visible spectra of each sample (25 °C and pH 6) from 300 to 600 nm and the corresponding peak absorbance are shown in Figure 4. Each batch experiment is carried out by adding a specific amount of adsorbent to 50 mL MO solution with initial concentration at a specific pH and temperature. The mixtures are mixed thoroughly with magnetic stirring and maintained for a predetermined time of (5 min to 3 h) to ensure complete adsorption. The samples are taken using 5 mL syringe and filtered using membrane filters (Nylon, 17 mm diameter, 0.45 µm pore size). After that, the concentration of MO in the sample was measured by the UV-Vis spectrophotometer.

The amount of adsorbed MO at any time (q_t) was calculated by equation (1).

$$q_t = \frac{(C_o - C_t) \times V}{m} \tag{1}$$

where q_t is the adsorbed amount of MO per unit mass of adsorbent (mg/g), C_o is the initial concentration of MO (mg/L), C_t is the residual concentrations of MO in the liquid phase at time t (min), V is the total volume of the liquid in the beaker (L), m is the mass of the adsorbent used (mg). For calculating the amount of adsorbed MO at equilibrium (q_e), C_e replaces C_t, in equation (1), where C_e is the residual equilibrium concentration in the liquid phase (mg/L). Also, the removal efficiency (or adsorption efficiency) was calculated using equation (2).

$$RE = \frac{C_o - C_t}{C_o} \times 100 \tag{2}$$

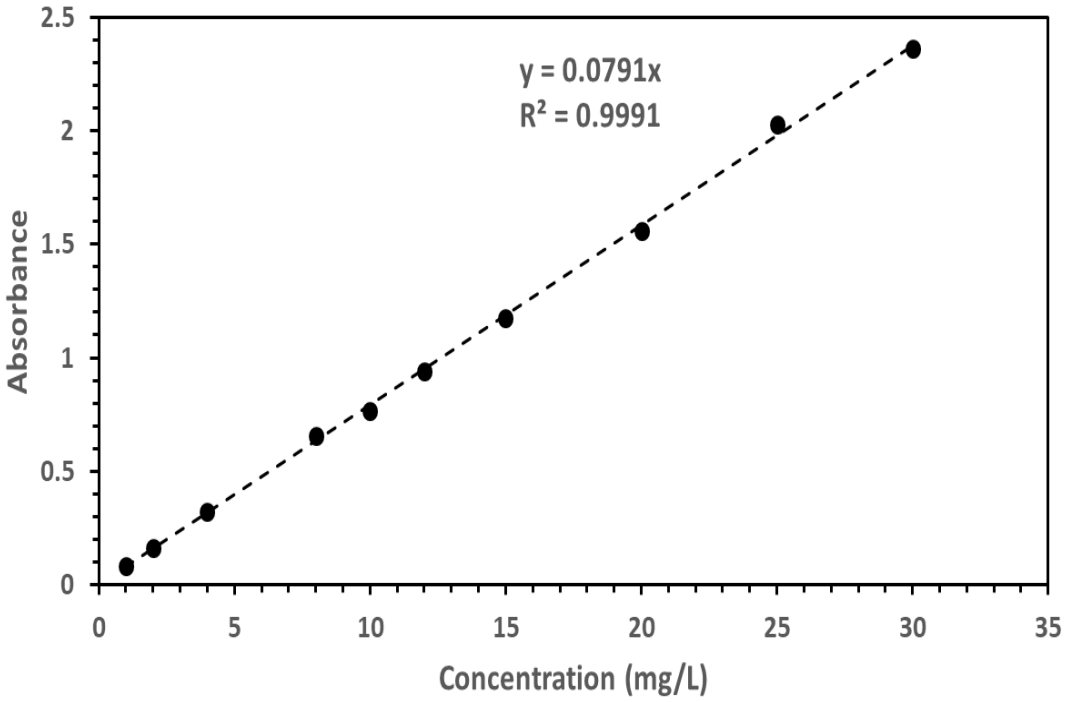

Figure 3: Calibration curve for MO solutions.

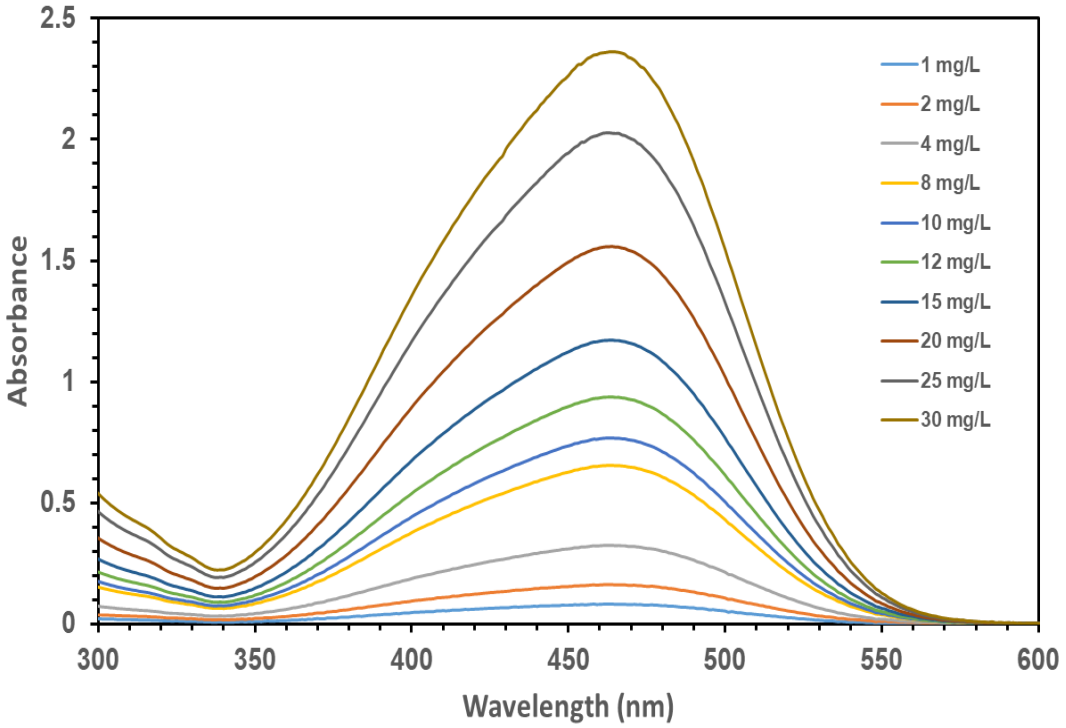

Figure 4: Visible spectra of MO solutions.

3.1.3 Characterization. Characterization of the MOF samples, before and after the adsorption of MO, was done using several complementary techniques. First, the crystal structure was verified using X-ray diffraction (XRD) measurements. In this work, XRD patterns of the samples were collected on a Bruker D8 ADVANCE system with a Cu tube and a linear detector (LYNXEYE XE). The measurements were performed over a 2θ range of 5.0–60° with a step size of 0.03°.

The shapes and crystallite morphologies were examined using a Scanning Electron Microscope (SEM) and Transmission Electron Microscope (TEM).

Fourier Transform Infrared (FTIR) spectra were obtained on FTIR spectrophotometer (PerkinElmer, USA) using the transmission KBr pellet (pressed-disc) technique, operating in the range of 4000 to 450 cm^{-1}, and 10 scans were signal-averaged with a resolution of 1.0 cm^{-1}.

Thermal gravimetric analysis (TGA) of the MOF samples were obtained using a Pyris 1 TGA instrument (PerkinElmer, USA) at a heating rate of 10 °C.min^{-1} from 30 °C to 700 °C.

The surface point zero charge (pH_{PZC}) of each MOF was determined using the solid addition method. The procedure is similar to what is reported in [85], [86], except for the KNO_3, HNO_3, and KOH solutions, where they were replaced with NaCl, HCl and NaOH solutions, respectively.

The experiments were carried out in a series of 100 mL conical flasks containing 50 mL of 0.01M of NaCl solutions. The pH is adjusted by adding either 1M HCl or 1M NaOH such that each flask will contain solution with different initial pH (pH_i) in the range of 2-12.

The pH_i of the solutions was then accurately measured. The adsorbent (100 mg) was added to each flask, and they were securely sealed immediately. The suspensions were then intermittently shaken and allowed to equilibrate for at least 48 hours. The difference between pH_i and the final pH (pH_f) values (ΔpH) was plotted against pH_i. The point at which ΔpH equal zero is considered the pH_{PZC}.

3.1.4 Error analysis. Three error functions are used to quantitatively assess the fitting accuracy of the employed kinetic and isotherm models, which are the coefficient of determination (R^2), Root Mean Square Error (*RMSE*) and the Sum of Squared Errors (*SSE*). These functions are expressed in equations (3-5).

$$R^2 = \frac{\sum_{i=1}^{N}\left(q_{e,i} - q_{e,avg}\right)^2 - \sum_{i=1}^{N}\left(q_{e,i} - q_{p,i}\right)^2}{\sum_{i=1}^{N}\left(q_{e,i} - q_{e,avg}\right)^2} \tag{3}$$

$$RMSE = \sqrt{\frac{1}{N}\sum_{i=1}^{N}\left(q_{p,i} - q_{e,i}\right)^2} \tag{4}$$

$$SSE = \sum_{i=1}^{N}\left(q_{p,i} - q_{e,i}\right)^2 \tag{5}$$

where q_e, q_p, and $q_{e,avg}$ are the experimental adsorbed amount of MO (mg/g), the predicted value from the isotherm model corresponding to C_e (mg/L) and the average of q_e, respectively. N denotes the number of experimental data points. The values of the error functions were calculated using the regression tool in MATLAB.

3.1.5 Adsorption kinetics. The kinetics of dye adsorption onto any adsorbent material is important for choosing the most optimal operating conditions, such as residence time required to reach equilibrium, in a full-scale adsorption system. The study of adsorption kinetics reveals the dye uptake rate which controls the residence time of the dye at the solution interface. The importance of calculating the rate arises when designing the adsorption system, and this rate can be calculated from the kinetic study. In this work, Kinetic experiments were carried out at different initial concentrations (5 –15 mg/L). Kinetic data were fitted to pseudo-first-order (PFO) [87], pseudo-second-order (PSO) [88] and Elovich [89] models. The PFO, PSO and Elovich kinetic models are given in equations (6-8).

$$q_t = q_e\left(1 - e^{-k_1 t}\right) \tag{6}$$

$$q_t = \frac{k_2 q_e^2 t}{1 + k_2 q_e t} \tag{7}$$

$$q_t = \frac{1}{\beta} ln(1 + \alpha\beta t) \quad (8)$$

where k_1 (min^{-1}) represents the PFO kinetic constant, k_2 ($g.mg^{-1}.min^{-1}$) is the PSO kinetic constant, α ($mg.g^{-1}.min^{-1}$) is the initial adsorption rate and β ($g.mg^{-1}$) is the desorption constant related to the extent of surface coverage and the activation energy. All kinetic parameters were determined using non-linear regression technique.

To further understand the diffusion mechanism involved in MO adsorption over MOFs, the intraparticle diffusion kinetics were investigated using the Weber-Morris intraparticle diffusion (IPD) model [90], which is expressed in equation (9),

$$q_t = k_P t^{0.5} + C \quad (9)$$

where k_P ($mg.g^{-1}.min^{-0.5}$) is the intraparticle diffusion rate constant and C ($mg.g^{-1}$) is the intraparticle diffusion constant related to the thickness of boundary layer [90]. Based on the IPD model, the plot of q_t versus $t^{0.5}$ should yield a straight line passing through the origin if intraparticle diffusion was the only rate-limiting step in the adsorption process [46]. Multi-linearity, on the other hand, is indicative of multiple mechanisms that control the adsorption process [91].

3.1.6 Adsorption isotherms. Adsorption isotherms are critical for investigating adsorption mechanisms and effective design of adsorption systems [92]. Besides, they provide qualitative information about the nature of the adsorbate-adsorbent interaction and the relation between the equilibrium concentration of adsorbate and its degree of accumulation onto the adsorbent surface at a constant temperature [93]. Equilibrium adsorption isotherms of MO were studied with initial concentration ranges of 10–250 mg/L and MOF dosage of 50 mg. The obtained adsorption equilibrium data were fitted to Langmuir [94], Freundlich [95], Dubinin-Radushkevich (D-R) [95], and Temkin [95] isotherm models.

The Langmuir isotherm model is based on the following assumptions: (1) the adsorbate forms a homogeneous monolayer at the adsorbent surface; (2) adsorption is at finite number of well-defined sites; (3) all adsorption sites are energetically equivalent; (4) each adsorption site can hold only one adsorbate molecule; (5)

interactions between adjacent adsorbate molecules do not exist. The Langmuir isotherm is given in equation (10).

$$q_e = \frac{q_m K_L C_e}{1 + K_L C_e} \tag{10}$$

where q_m is the maximum monolayer adsorption capacity (mg/g) with the highest dye concentration used in the experiment, K_L is the Langmuir constant (L/mg) associated with the adsorption rate. From the value of K_L calculated from the Langmuir model, the Langmuir dimensionless separation factor or equilibrium parameter (R_L) is calculated by equation (11).

$$R_L = \frac{1}{\left(1 + K_L C_o\right)} \tag{11}$$

where R_L indicates the shape of the isotherm to be either irreversible (R_L=0), favorable (0<R_L<1), linear (R_L=1), or unfavorable (R_L>1).

Freundlich isotherm model assumes that adsorption occurs via multilayers instead of a monolayer on a heterogeneous surface. It also assumes that adsorption sites with different adsorption energies are involved in the adsorption of adsorbate molecules. Equation (12) describes the Freundlich isotherm model.

$$q_e = K_F C_e^{1/n} \tag{12}$$

where n and K_f ($(mg.g^{-1})(L.mg^{-1})^{1/n}$) are Freundlich constants related to the favorability of the adsorption process and the adsorption capacity of the adsorbate, respectively. If ($1/n$)<1, it indicates favorable adsorption.

The Temkin isotherm assumes that as the surface coverage of the adsorbent increases the heat of adsorption decreases linearly [96]. Also, this model assumes that the binding energy is distributed uniformly [97]. The Temkin isotherm is given in equation (13).

$$q_e = \frac{RT}{b_T} ln\left(K_T C_e\right) \tag{13}$$

where K_T (L.mg^{-1}) is the Temkin isotherm constant, and b_T (kJ.mol^{-1}) is the constant related to the heat of adsorption. R is the universal gas constant, and T (K) is the absolute temperature.

The Dubinin-Radushkevich (D-R) isotherm model accounts for the effect of the porous structure of the adsorbent [95]. The model assumes that multilayer adsorption takes place on the adsorbent surface and that the surface is heterogeneous [97]. Also, the model can be used to express the adsorption mechanism with a Gaussian energy distribution function [97]. Equations (14) and (15) present the D-R isotherm model.

$$q_e = q_{DR} e^{-K_{DR}\varepsilon^2} \tag{14}$$

$$\varepsilon = RT\, ln\left(1 + \frac{1}{C_e}\right) \tag{15}$$

where q_{DR} (mg.g^{-1}) is the D-R constant representing the theoretical adsorption capacity, ε is the Polanyi potential, and K_{DR} (mol^2.kJ^{-2}) is the constant of the adsorption energy which can be correlated to the mean adsorption energy (E) by using equation (16).

$$E = \frac{1}{\sqrt{2K_{DR}}} \tag{16}$$

In general, the calculated value of E can give an insight into whether the adsorption is physical or chemical. If the value of E is between 8 and 16 kJ.mol^{-1}, then the adsorption is dominated by a chemical mechanism, while if E is less than 8 kJ.mol^{-1}, then the adsorption proceeds through a physical mechanism [98]–[100].

3.1.7 Adsorption thermodynamics. The thermodynamic parameters such as Gibbs free energy (ΔG°), change in enthalpy (ΔH°), and change in entropy (ΔS°) are important to understand the adsorption behavior related to temperature. These parameters provide an insight into the mechanism related to the adsorption process being investigated.

Generally, ΔH° values less than 40 kJ.mol^{-1} are indicative of physical adsorption, whereas ΔH° values greater than 80 kJ.mol^{-1} are indicative of a chemical adsorption process [101], [102]. ΔG°, ΔH°, and ΔS° are calculated using equations (17) and (18).

$$\Delta G^{o} = -RT\, ln\left(K_{eq}\right) \tag{17}$$

$$ln\left(K_{eq}\right) = \frac{\Delta S^{o}}{R} - \frac{\Delta H^{o}}{RT} \tag{18}$$

where K_{eq} is the adsorption equilibrium constant. From equation (18), it can be seen that a plot of $ln(K_{eq})$ vs. $1/T$ will give a straight line with slope equal to $(-\Delta H^{\circ}/R)$ and intercept equal to $(\Delta S^{\circ}/R)$. This plot is called Van't Hoff plot. It relates the change in adsorption equilibrium constant, K_{eq}, to the change in temperature, and is widely used to estimate ΔH° and ΔS° of adsorption.

3.1.8 Factorial experimental design. The design of experiments (*DOE*) is a method used to plan for experiments such that the data obtained can be statistically analyzed to reach objective conclusions. In any experiment, it is desired to change one or more process variables (or factors) in order to observe the effect the changes have on one or more response variables. The basic steps of statistically designed experiments are (1) selection of factors and their corresponding levels; (2) determination of response variables; (3) selection of the experimental design; (4) statistical analysis of the experimental data.

The full factorial design is one of the most widely used experimental designs to investigate the effects of experimental factors and the interactions between those factors (i.e., how the effects of one factor changes with the level of other factors). One of the main advantages of this design is the reduced number of experiments which reduces the cost associated with the experimental work [103]. The number of experimental runs is given by L^{k}, where k is the number of factors and L is the number of levels in the design space (range of values over which factors are to be varied) [104].

The 2^{k} factorial designs are widely applied in adsorption experiments to estimate the main effects as well as interaction effects, where each variable is investigated at two levels (high and low). In this work, the response variable was selected to be the removal efficiency of MO (*RE*) which is calculated according to equation (2) presented in section 3.1.2. To evaluate the statistical significance of the factors, *RE* was determined as the average of two parallel experiments. For analysis of the experimental data, Minitab Statistical Software (Version 17) was used.

3.2 Results and Discussion

3.2.1 Characterization of materials.

3.2.1.1 Morphology. Figure 5 shows the measured XRD patterns of the MOF samples before and after MO adsorption. The results show that both Cu-BTC and ZIF-8 have a crystalline structure and that the obtained patterns for the commercial MOFs are in good agreement with those reported in the literature for the equivalent lab-synthesized MOFs [60], [105]–[111].

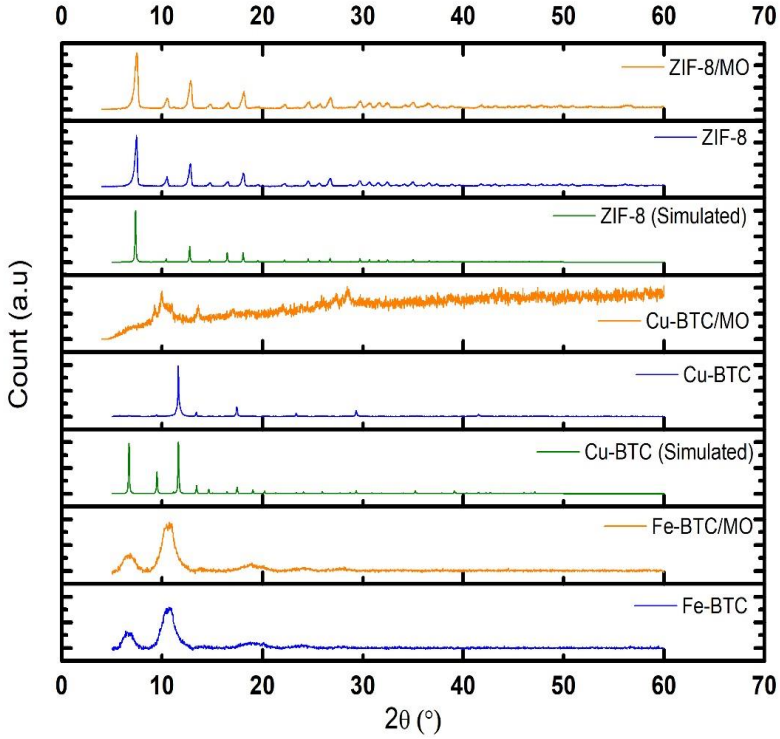

Figure 5: XRD patterns of MOF samples before and after adsorption. The simulated patterns were obtained from the Cambridge Crystallographic Data Centre.

The main signature peaks present for Cu-BTC in the XRD patterns are at 2θ = 11.61°, 13.4°, 17.45°, 23.36°, and 29.33°. In addition, two additional peaks that are reported in the literature at 2θ = 6.7° and 9.5° were detected at low intensity. On the other hand, the signature peaks for ZIF-8 are at 2θ = 7.45°, 10.5°, 12.8°, 14.8, 16.5 and 18.1°. For the Fe-BTC sample, XRD patterns reveal that it is a material of low crystalline order, which is in agreement with what is reported in the literature for commercial Fe-BTC as well as lab-synthesized Fe-BTC [112]–[115]. Also, The semi-amorphous nature of the MOF can be inferred from the XRD patterns which show a

series of broad peaks superposed at 2θ positions that match well with the narrow peaks of the XRD pattern of MIL-100(Fe) material, which has the same chemical composition as Fe-BTC (both are constituted by Fe(III) and BTC) [113], [116].

The XRD patterns of Fe-BTC and ZIF-8 after MO adsorption show that their structure remains intact, while the XRD pattern of the Cu-BTC/MO sample revealed apparent loss of crystallinity, which is an indication that the crystalline structure of Cu-BTC was damaged after adsorption.

The SEM and TEM micrographs shown in Figures 6 and 7, respectively, reveal the crystal morphologies of the MOF samples before and after MO adsorption. The SEM and TEM images for the fresh samples are similar to those reported in the literature for Fe-BTC [112], [115], [117], Cu-BTC [105], [118], [119] and ZIF-8 [120]–[122]. For Cu-BTC, the well-known octahedral shape can be seen in Figure 6(a). However, the morphology of the after adsorption sample shown in Figure 6(b) can't be seen due to the loss of the spatial structure of the MOF. In addition, SEM images of the small particles of ZIF-8 and ZIF-8/MO are shown in Figure 6.

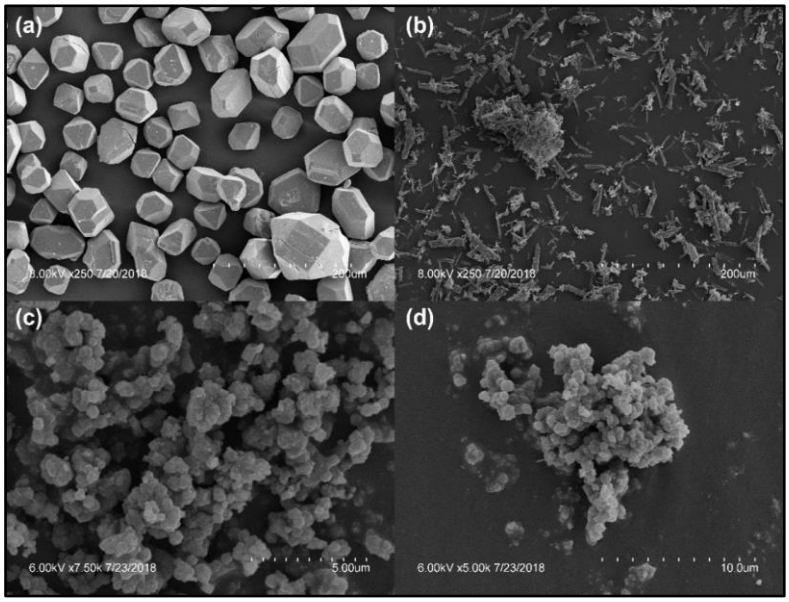

Figure 6: SEM micrographs of (a) Cu-BTC; (b) Cu-BTC/MO; (c) ZIF-8; (d) ZIF-8/MO.

The TEM micrographs in the nm scale presented in Figure 7 reveal the polyhedral shape of ZIF-8. For Fe-BTC samples, it was difficult obtaining SEM images

at higher magnification due to the magnetic character of the Fe-rich samples, whereas TEM images in Figure 7(a) and 7(b) clearly reveal the semi-amorphous nature of Fe-BTC.

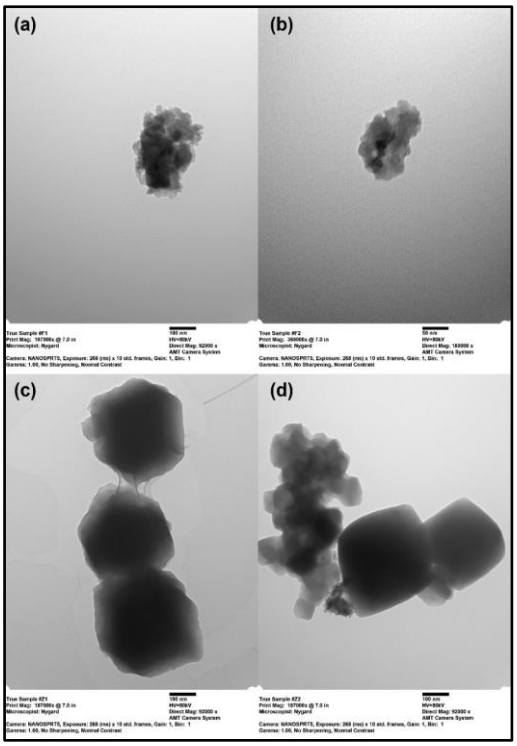

Figure 7: TEM micrographs of (a) Fe-BTC; (b) Fe-BTC/MO; (c) ZIF-8; (d) ZIF-8/MO.

3.2.1.2 FTIR. The FTIR spectra of the MOF samples presented in Figure 8 are in good agreement with the literature [112], [123]–[127]. For Fe-BTC and Cu-BTC MOFs, the measured IR spectra show quite similar absorption peaks. This can be explained by the similarity in nature of the two MOFs regardless of their crystalline order [112], [117].

The broad peaks between 3800 – 3000 cm^{-1} for both samples corresponds to the presence of an OH group of the adsorbed water molecules. Both Fe-BTC and Cu-BTC absorb some of the moisture in the atmosphere, and this explains the presence of free water molecules in the sample before adsorption. On the other hand, water in the samples after adsorption is mainly from the adsorbed water molecule from the aqueous solution.

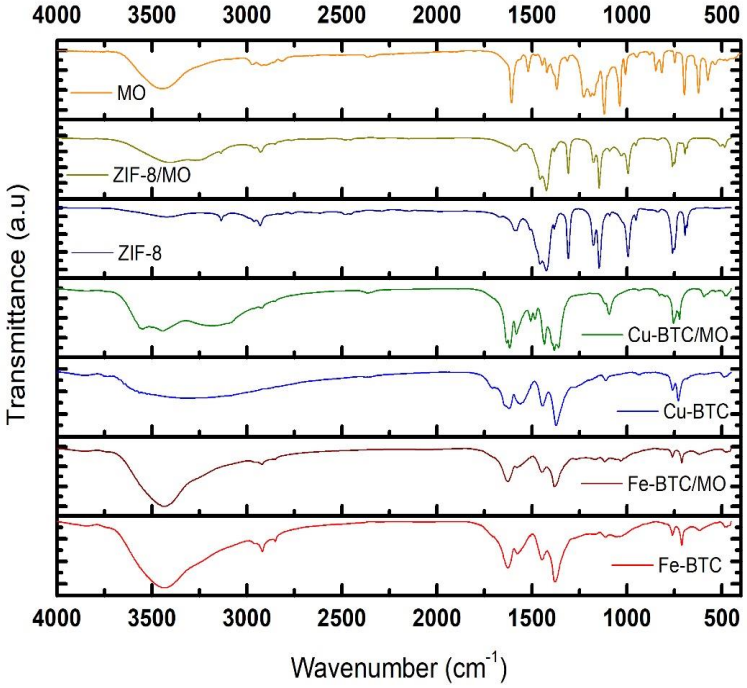

Figure 8: FTIR spectra of MOF samples before and after MO adsorption.

The IR spectrum for the Fe-BTC sample shows absorption peaks at 711.6, 760.5, 1380, 1448, 1577, and 1627 cm^{-1}. The two Absorption bands at 1577 cm^{-1} and 1627 cm^{-1} are attributed to the carboxylic (COO) asymmetric stretching, whereas the peak at 1448 cm^{-1} belongs to the corresponding symmetric stretching vibration [112]. The peak at 1380 cm^{-1} indicates the presence of (C–O) from the BTC ligand [128]. Fe-BTC sample also presents supplementary bands at 2918 and 2851 cm^{-1} that can be assigned to aliphatic C–H groups [114]. In addition, the bands at 760.5 cm^{-1} and 711.6 cm^{-1} might be attributed to Fe–O stretching vibration. The vibrational band corresponding directly to the ligand coordinated with the centered Fe(III) ions is also visible on the IR absorption band at 484.1 cm^{-1}. The IR spectrum of Fe-BTC/MO sample shows a slight shift in some of the peaks related to the carboxylic (COO) stretching and the ligand–Fe bond vibration. Also, the broad band in the range of 3800 – 3000 cm^{-1} had a narrower and less intense peak which might be ascribed to OH group having hydrogen bond interaction with the MO molecule. The measured IR spectra for the Cu-BTC sample on the other hand show absorption peaks at 729.6, 760.1, 1373, 1445, 1560, and 1620 cm^{-1}. The two Absorption bands at 1560 cm^{-1} and 1620 cm^{-1} are attributed to the COO asymmetric stretching, whereas the peaks at 1445 cm^{-1} belong to

the corresponding symmetric stretching vibration [112]. The peak at 1373 cm^{-1} indicates the presence of (C–O) from the BTC ligand [128]. Also, the bands at 760.1 cm^{-1} and 729.6 cm^{-1} might be attributed to Cu–O stretching vibration [84]. The vibrational band corresponding directly to the ligand coordinated with the centered Cu(II) ions is also visible on the IR absorption band at 487 cm^{-1} [129], [130]. The IR spectrum for Cu-BTC/MO sample show clear changes in the peaks related to the COO stretching modes in the 1700 – 1300 cm^{-1} range, and the ligand–Cu bond vibration in the 760 – 730 cm^{-1} range. In the IR spectrum of both Fe-BTC/MO and Cu-BTC/MO, the peak around 1120 cm^{-1} can be assigned to the S-O bonds from MO, confirming the presence of MO molecules onto Fe-BTC and Cu-BTC surfaces. For the ZIF-8 samples, The broad peak in the 3300 – 3600 cm^{-1} range corresponds to the stretching of the N–H bond and the small peaks at 3140 cm^{-1} and 2930 cm^{-1} are attributed to the aromatic and aliphatic C–H stretching vibrational modes of the imidazole ring and the methyl group present in the linker, respectively [131]. In addition, the peak at 1590 cm^{-1} can be assigned to the stretching mode of C=N, whereas that observed between 1460 and 1310 cm^{-1} is associated with the vibration of the entire imidazole ring [132]. Also, the peak at 1150 cm^{-1} corresponds to the C–H bending in the imidazolate [132]. Finally, the peaks between 1100 and 950 cm^{-1} could be related to the in-plane bending of the imidazole ring [131], while the peaks at 760 and 694 cm^{-1} were associated with the out-of-plane bending of the ring [132]. For the ZIF-8/MO sample, the broader and more intense peak in the 3300 – 3600 cm^{-1} range was related to the stretching of the N–H bond plus the stretching vibration of the free hydroxyl group and the hydrogen bonded hydroxyl groups confirming the presence of free water in the ZIF-8/MO sample [127]. Finally, the small peak at 1030 cm^{-1} could be ascribed to the presence of MO on the ZIF-8 surface.

3.2.1.3 TGA. TGA was used to test the stability of the MOFs before and after MO adsorption. The TGA results are presented in Figure 9, and they indicate that the overall thermal stabilities of the MOFs were comparable to those reported for the lab-synthesized MOFs [105], [117], [133]. For Fe-BTC MOF, the overall weight loss for the sample before adsorption was around 70%, whereas the sample after adsorption had a slightly higher weight loss of about 72%.

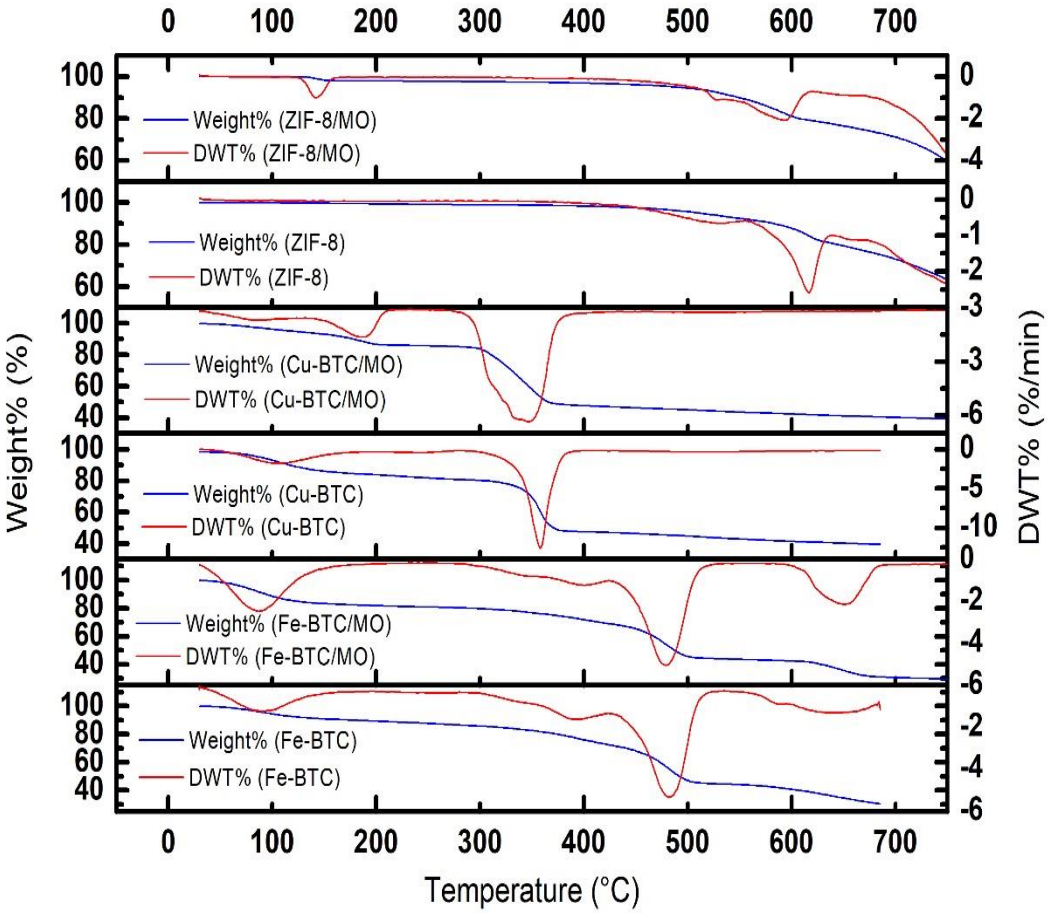

Figure 9: TGA results of MOF samples before and after MO adsorption.

This is confirmed by the peak in derivative weight loss (DWT%) curves for both samples, where the Fe-BTC/MO sample had slightly more intense peak indicating higher water content in the sample, mainly from the MO aqueous solution. In addition, at 200°C, Fe-BTC sample lost around 10% of its weight, whereas Fe-BTC/MO sample lost around 20%, mostly water content. Then, between 200°C and 300°C, both samples showed no significant weight loss. Following this, both samples continued to lose weight between 300°C and 500°C where total weight loss reached around 55% at 500°C. This loss can be attributed to the decomposition of BTC linkers [80]. Between 500°C and 600°C, there was no significant weight loss, followed by a sudden drop in weight above 600°C (ca. 10% for Fe-BTC and ca. 12% for Fe-BTC/MO). This loss of weight is due to the total decomposition of the samples and the formation of iron-containing ashes [113].

For Cu-BTC MOF, the overall weight loss of the samples was around 60%. The first drop in weight is at 100°C which corresponds to the evaporation of water present in the samples. This is confirmed by the peak in DWT% curves for both samples, where Cu-BTC/MO sample had a second peak between 150°C and 200°C, indicating higher water content in the sample, mainly from the MO aqueous solution. Then, above 200°C, Cu-BTC sample showed no significant weight loss up to 360°C after which a sudden weight loss is observed from the DWT% curve. On the other hand, the second stage of weight loss for the Cu-BTC/MO sample occurs at around 300°C, where a broad shoulder peak in the DWT% curve is observed. In both cases, this drop in weight is attributed to the total decomposition of BTC linkers and production of CuO as the remaining product [107], [108], plus the decomposition of MO in the Cu-BTC/MO sample.

For ZIF-8 MOF, the overall weight loss for the sample before adsorption was around 38%, whereas the sample after adsorption had a slightly higher weight loss of about 40%. The TGA results for ZIF-8 sample show that there was no weight loss in the temperature range of 100–450 °C, indicating that the ZIF-8 had no trapped solvent molecules inside the framework and that it was stable up to 450 °C.

On the other hand, the ZIF-8/MO sample had a small weight loss (2%) at 150 °C, corresponding to the release of water adsorbed at the crystal surface. Then both samples exhibited a gradual weight loss at around 500 °C followed by a sharp drop at 600 °C due to the structural collapse of ZIF-8 and decomposition of the organic ligand leading to the formation of ZnO as the final product [131]. In comparison, ZIF-8 had the best overall thermal stability among the three MOFs under consideration.

3.2.2 Removal efficiencies. Figure 10 demonstrates the removal efficiency as a function of time for the three adsorbents. Among the three MOFs considered, Fe-BTC had the highest maximum MO removal efficiency (91%), followed by ZIF-8 (63%), and finally Cu-BTC (35%).

It can be seen that the adsorption process onto Fe-BTC was very rapid and most MO was adsorbed in the first 10 minutes (80%), and the equilibrium could be achieved in 60 min, while adsorption over ZIF-8 took 180 min to reach equilibrium.

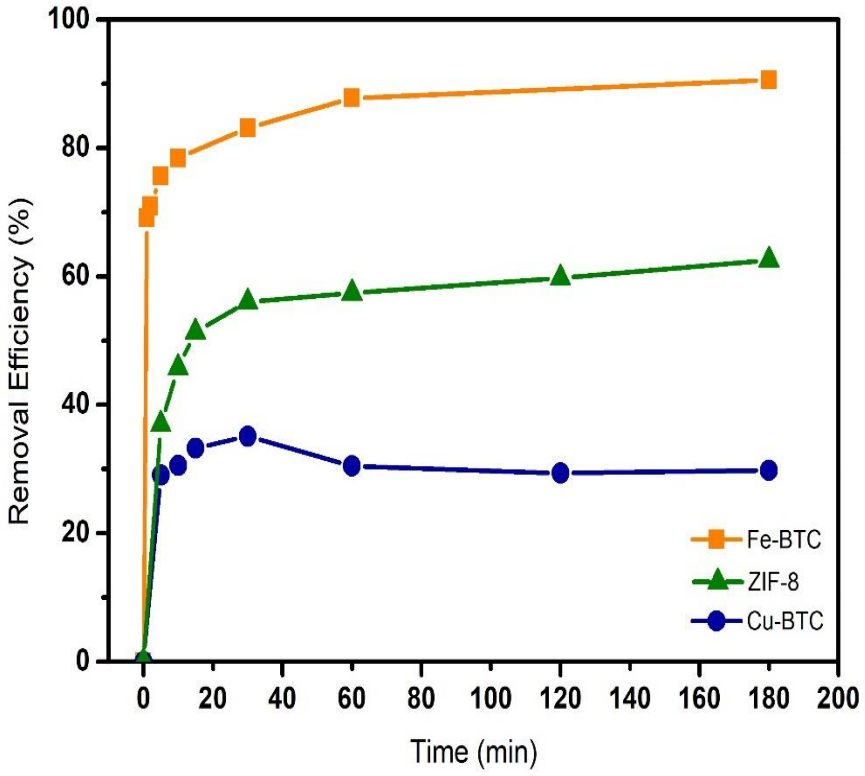

Figure 10: Comparison of MO removal efficiency of Fe-BTC, Cu-BTC and ZIF-8 (m = 100 mg, C_o = 15 mg/L, pH = 6).

In contrast, the removal efficiency of Cu-BTC drops after 30 minutes indicating that the structure of the adsorbent was damaged as was confirmed by the XRD results for Cu-BTC/MO sample, hence, can't be considered as a good candidate for the removal of MO from aqueous solutions under the investigated experimental conditions. Furthermore, although Fe-BTC had the lowest BET surface area (according to the data reported by Sigma-Aldrich), it had the highest removal efficiency, indicating that MO adsorption was not necessarily directly related to the surface area or pore volume of the MOF used, rather, it can be due to the presence of specific interaction between the MOF and MO. Additionally, Luan Tran et al. [134] studied the effect of the external surface area of ZIF-8 on dyes adsorption capacity. According to their findings, the external surface of ZIF-8 was the only contributor to adsorption and that there was no adsorption inside the pores of the MOF. Also, the lower removal efficiency of ZIF-8 compared to Fe-BTC can be linked to the hydrophobic character of ZIF-8 versus the hydrophilic nature of Fe-BTC [116], [127]. Therefore, these factors may be the reason for the limited MO adsorption capacity over ZIF-8 despite the larger surface area of the MOF.

3.2.3 Effect of initial pH (pH_i) and adsorption mechanism. The influence of initial pH on the adsorption of MO was investigated in the range of 2–12. In this work, the pH effect experiments were carried out at 298 K. The initial concentration was kept at 15 mg/L, and the dosage of the MOF was 150 mg. The effect of pH on MO adsorption is shown in Figure 11(a). For Fe-BTC, the pH_i of the solution had an insignificant effect on the adsorption capacity of MO in the range of 2–10, while in the same range, ZIF-8 had the highest adsorption capacity at pH_i of 2 with relatively similar capacities between 4 and 10. On the other hand, the adsorption capacity of Cu-BTC decreased as pH_i increased in the same range. At pH_i 12, the adsorption capacity of all MOFs was the lowest suggesting the collapse of the MOFs' structures under strong alkali conditions [78].

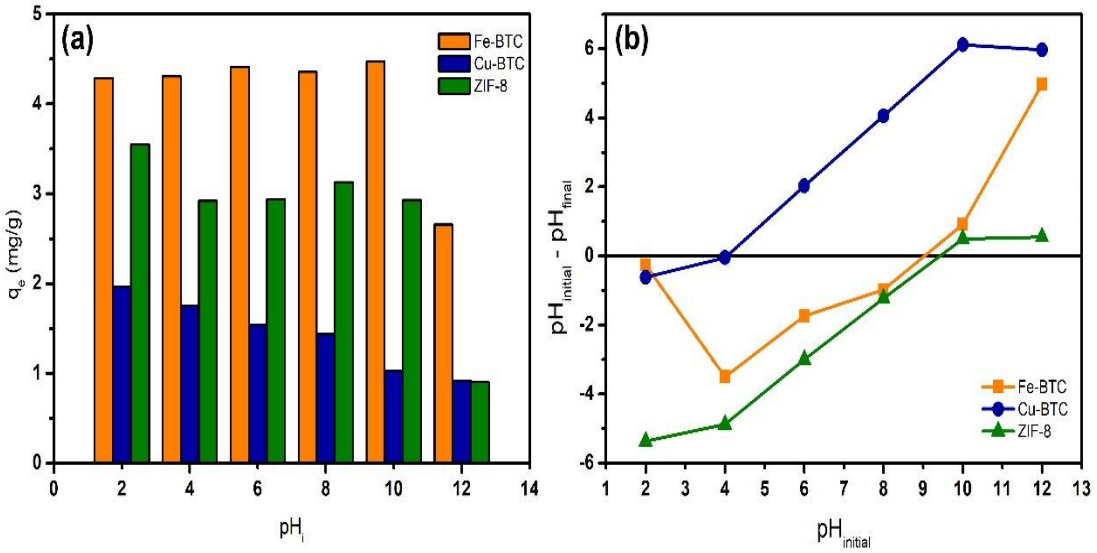

Figure 11: (a) Effect of pH_i on adsorption capacity; and (b) Experimental solid-addition technique curves used to determine pH_{PZC} of the MOFs.

These findings can be linked with the results of pH_{PZC} experiments shown in Figure 11(b). For pH_i less than pH_{PZC}, the surface of the MOF is more positively charged, which enhances the electrostatic attraction between the adsorbent surface and the negatively charged MO molecules (MO usually exists in the sulfate form). Also, for pH_i greater than pH_{PZC}, the surface of the MOF is more negatively charged which leads to strong repulsion between the negatively charged surface of the MOF and the negatively charged MO molecules [72], [78]. In the case of Fe-BTC and ZIF-8, the pH_{PZC} was around 9 and 9.5 respectively. Therefore, the drop in the adsorption capacity

at pH 12 can be attributed to the repulsion between the negative surface charge and the negatively charged MO molecule, as well as the decomposition of the MOF structure. However, for Cu-BTC, the pH_{PZC} was around 4, which explains the higher adsorption capacity at pH_i less than 4 since the surface of Cu-BTC is more positively charged. However, it should be noticed that the improvement in the amount adsorbed at pH_i less than 4 was not substantial indicating that the effect of water on the structure of Cu-BTC was significant as was shown previously. As a result, all other experiments were carried out at the natural pH of the MO solution without adjustment (pH = 6). Finally, hydrogen bonds can form between MO nitrogen or oxygen atoms and hydrogen atoms in the benzene ring of Fe-BTC and the imidazole ring of ZIF-8. Hence, electrostatic and hydrogen-bond interactions are considered the primary mechanisms involved in the adsorption of MO on Fe-BTC and ZIF-8.

3.2.4 Effect of initial concentration. The results in Figure 12 reveal the effect of initial MO concentration on the adsorption capacity for both Fe-BTC and ZIF-8. It can be seen that as the initial concentration increases the adsorption capacity increases as well. This phenomenon can be explained by the fact that at a constant adsorbent dosage, increasing the initial dye concentration enhances the interaction between the dye and adsorbent (i.e., higher driving force for mass transfer), and as a result, leads to increase in MO uptake by the adsorbent [97]. Similar results were reported for the adsorption of MO and other dyes on different MOFs [72], [75], [135], [136].

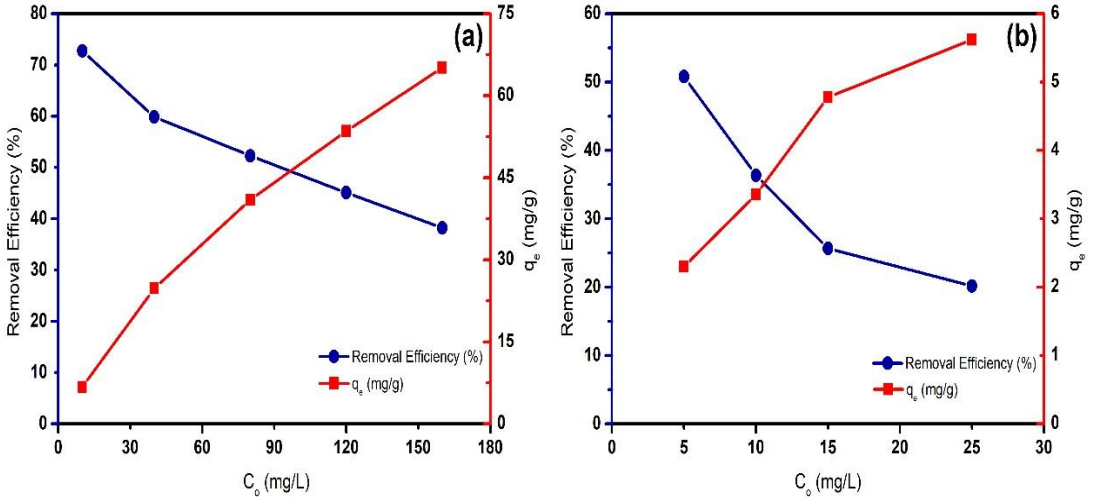

Figure 12: Effect of initial concentration (m = 50 mg) on adsorption capacity and removal efficiency for (a) Fe-BTC and (b) ZIF-8.

Also, it can be noticed that the removal efficiency (*RE*) decreases with increasing initial concentration. This is explained by the fact that at the same amount of adsorbent increasing C_o leads to a higher equilibrium concentration of MO due to the higher amount of the dye molecules in the liquid phase. Consequently, the difference between C_o and C_e will decrease leading to a decrease in the removal efficiency.

3.2.5 Effect of MOF dosage. Figure 13 shows that at initial MO concentration of 15 mg/L, increasing the MOF dosage resulted in a decrease in MO adsorption capacity. On the other hand, the opposite trend was noticed for the removal efficiency of MO; as the adsorbent dosage increased, the dye removal efficiency increased as well. The decrease in adsorption capacity can be attributed to the change in MOF to MO concentrations ratios. At higher MOF to MO ratio (i.e., higher adsorbent dosage), there is very fast superficial adsorption onto the surface of the adsorbent leading to lower MO concentration compared to the lower MOF to MO concentration ratio (i.e., lower adsorbent dosage) [49], [97], [137]. In other words, increasing adsorbent dosage leads to decreasing the concentration gradient between MO concentration in the solution and MO concentration on the adsorbent surface. This also explains the higher removal efficiency for the higher MOF dosage, as removal efficiency is calculated from the difference between the initial and final MO concentrations in the solution.

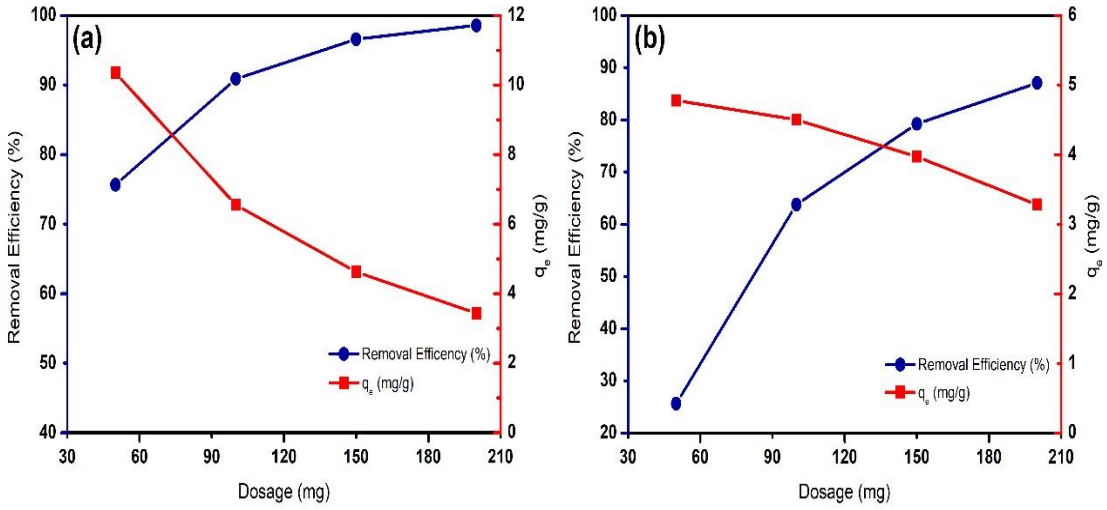

Figure 13: Effect of MOF dosage (C_o = 15 mg/L) on adsorption capacity and removal efficiency for (a) Fe-BTC and (b) ZIF-8.

3.2.6 Adsorption kinetics. The determined kinetic models' parameters along with their corresponding R^2, *RMSE*, and *SSE* are summarized in Table 4. The results reveal that the Elovich model provides the best fit for the experimental data in the case of MO adsorption over Fe-BTC, while for ZIF-8, both PFO and PSO provided a good fit for the experimental data, with the PSO being slightly superior. In addition, Figure 14 presents the predicted q_t curves from the Elovich and PSO models for Fe-BTC and ZIF-8, respectively.

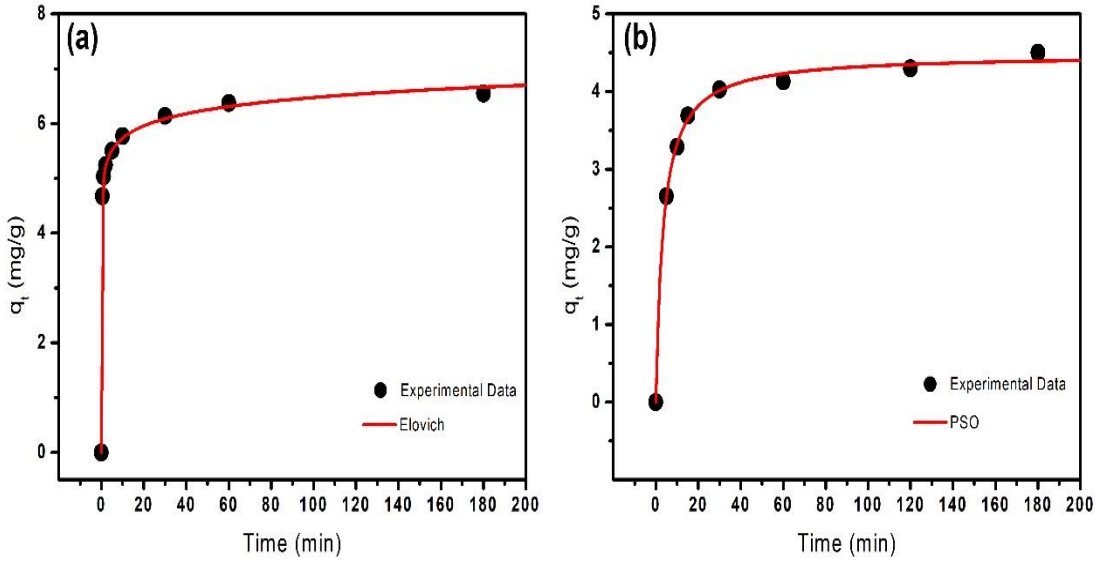

Figure 14: Kinetic models fitted to the experimental data (m = 100 mg, C_o = 15 mg/L) for (a) Fe-BTC, (b) ZIF-8.

In the case of Fe-BTC, the calculated q_e values (Table 4) from the PSO model show good agreement with the experimental q_e while for ZIF-8, both PFO and PSO provided a good agreement between $q_{e,exp,}$ and $q_{e,calc}$. Regarding the PSO rate constant (k_2), the results showed that the rate constant decreases with increasing initial MO concentration in the case of Fe-BTC. This can be ascribed to increasing competition for active adsorption sites as initial concentration increases [77], [78], [135]. In contrast, for ZIF-8, the rate constant increased with increasing initial MO concentration indicating the faster adsorption rate due to enhanced interaction between MO and ZIF-8 (i.e., higher driving force for mass transfer) [138]–[140]. Further, the rate constant values for Fe-BTC were greater than those for ZIF-8, confirming the higher removal efficiency results.

Table 4: Summary of kinetic parameters for MO adsorption over Fe-BTC and ZIF-8.

MOF	Kinetic Model	Parameters	C_o (mg/L)		
			5	10	15
		$q_{e,exp}$ (mg.g^{-1})	2.029	4.262	6.550
Fe-BTC	PFO	k_1 (min^{-1})	2.425	2.924	2.726
		$q_{e,calc}$ (mg.g^{-1})	1.847	3.866	5.896
		R^2	0.943	0.954	0.950
		RMSE	0.160	0.299	0.476
		SSE	0.179	0.626	1.585
	PSO	k_2 (g.mg^{-1}.min^{-1})	2.265	1.405	0.838
		$q_{e,calc}$ (mg.g^{-1})	1.922	4.007	6.118
		R^2	0.979	0.981	0.979
		RMSE	0.097	0.191	0.308
		SSE	0.065	0.256	0.663
	Elovich	α (mg.g^{-1}.min^{-1})	1.438×10^{5}	4.302×10^{6}	1.765×10^{6}
		β (g.mg^{-1})	9.194	5.089	3.108
		R^2	0.995	0.998	0.999
		RMSE	0.046	0.059	0.069
		SSE	0.015	0.025	0.033
ZIF-8		$q_{e,exp}$ (mg.g^{-1})	2.040	3.691	4.500
	PFO	k_1 (min^{-1})	0.061	0.093	0.170
		$q_{e,calc}$ (mg.g^{-1})	2.004	3.423	4.208
		R^2	0.996	0.984	0.984
		RMSE	0.060	0.191	0.199
		SSE	0.018	0.145	0.238
	PSO	k_2 (g.mg^{-1}.min^{-1})	0.034	0.046	0.065
		$q_{e,calc}$ (mg.g^{-1})	2.257	3.665	4.475
		R^2	0.989	0.996	0.998
		RMSE	0.095	0.098	0.070
		SSE	0.045	0.038	0.030
	Elovich	α (mg.g^{-1}.min^{-1})	0.394	31.920	53.670
		β (g.mg^{-1})	2.292	2.637	2.157
		R^2	0.953	0.999	0.984
		RMSE	0.191	0.054	0.198
		SSE	0.182	0.012	0.236

Finally, the high R^2 values and the low *RMSE and SSE* values obtained for the Elovich model indicate that the adsorption of MO on Fe-BTC might be heterogeneous (i.e., the adsorbing surface is heterogeneous) [141], [142].

In addition, the results of the intraparticle diffusion (IPD) model are shown in Figure 15. As can be seen, the obtained data for both Fe-BTC and ZIF-8 at different initial concentrations were not linear over the entire time range. Instead, they exhibited a tri-linear behavior, suggesting the existence of three successive adsorption stages. This multi-linear behavior has been reported in previous investigations [143], [144]. Each linear segment represents a controlling mechanism. In the first step, external surface adsorption related to diffusion through the boundary layer. In the second step,

IPD takes place. The third step is the equilibrium stage, where adsorption slows as surface coverage approaches saturation.

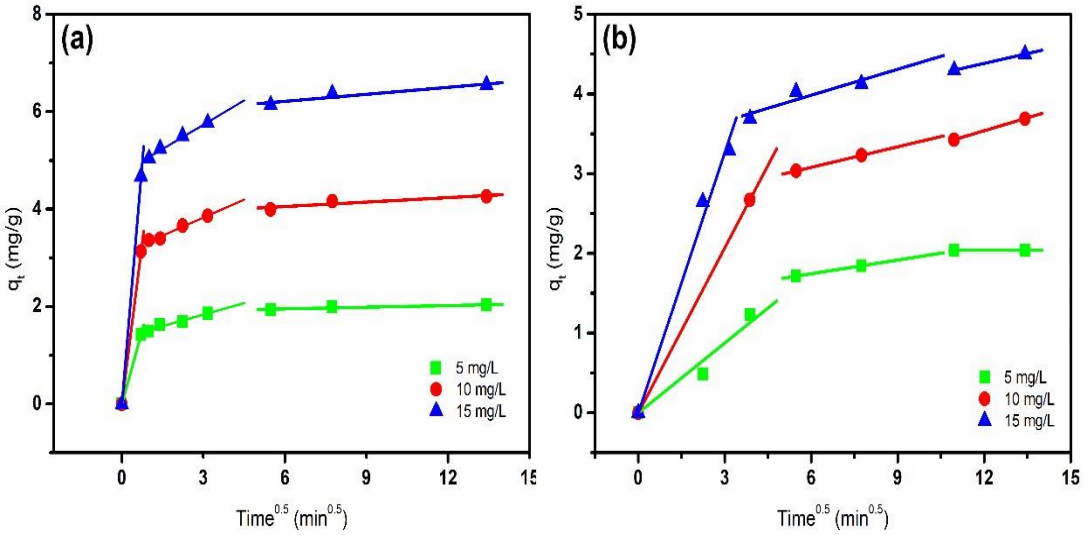

Figure 15: IPD model plot for MO adsorption over (a) Fe-BTC and (b) ZIF-8 (dosage is 100 mg).

3.2.7 Adsorption isotherms. Figure 16 represents the non-linear plots of the Langmuir isotherm fitted to the experimental data of q_e versus C_e at 298 K for both Fe-BTC and ZIF-8. The calculated maximum adsorption capacities, isotherm parameters and the respective values of R^2, *RMSE*, and *SSE* are summarized in Table 5.

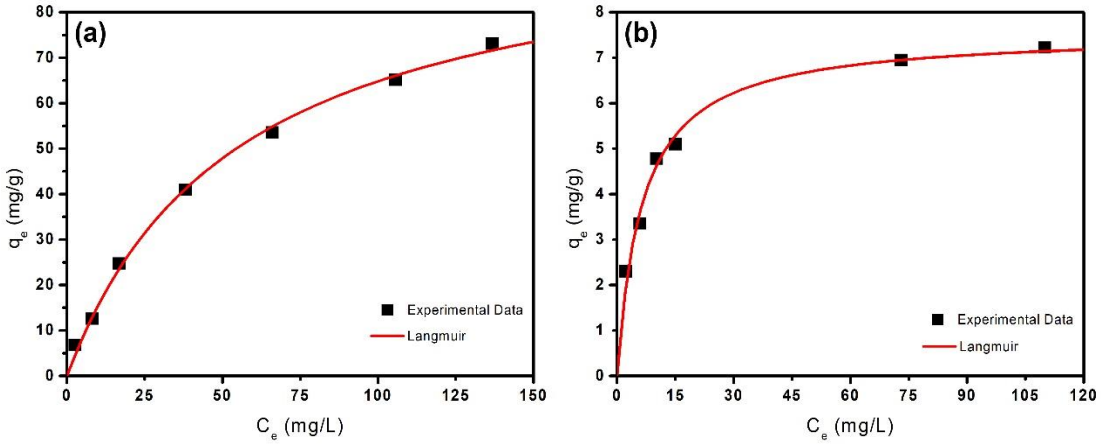

Figure 16: Langmuir isotherm model for MO adsorption on (a) Fe-BTC and (b) ZIF-8 at 298 K.

Among the four models, Langmuir had the best fitting parameters (highest R^2 and lowest *RMSE* and *SSE*) for both MOFs. It can be noticed that the calculated q_m increases as temperature increases in the case of MO adsorption over Fe-BTC, whereas

the opposite is noticed in the case of ZIF-8. This suggests that the adsorption is more effective at a higher temperature for Fe-BTC in contrast to the ZIF-8, where adsorption is favored at a lower temperature.

Table 5: Summary of adsorption isotherms for MO adsorption on Fe-BTC and ZIF-8.

MOF	Isotherm Model	Parameters	*T* (K)		
			298	303	313
Fe-BTC	Langmuir	q_m (mg/g)	100.3	105.0	114.0
		K_L (L/mg)	0.018	0.021	0.025
		R^2	0.997	0.998	0.991
		RMSE	1.508	1.967	4.020
		SSE	11.370	11.610	48.470
	Freundlich	K_F (mg.g^{-1})(L.mg^{-1})$^{1/n}$	5.375	6.103	7.423
		n	1.864	1.948	1.917
		R^2	0.990	0.991	0.967
		RMSE	2.867	4.088	7.808
		SSE	41.090	50.140	182.900
	Temkin	K_T (L.mg^{-1})	0.350	0.449	0.502
		b_T (kJ.mol^{-1})	0.143	0.135	0.128
		R^2	0.951	0.987	0.967
		RMSE	6.264	4.960	7.729
		SSE	196.2	73.8	179.2
	Dubinin-Radushkevich (D-R)	K_{DR} (mol^2.kJ^{-2})	54.99	13.62	11.78
		q_{DR} (mg.g^{-1})	64.30	77.56	78.07
		E (kJ.mol^{-1})	0.095	0.192	0.206
		R^2	0.886	0.969	0.951
		RMSE	9.534	7.554	9.499
		SSE	454.5	171.2	270.7
ZIF-8	Langmuir	q_m (mg/g)	7.56	5.62	4.65
		K_L (L/mg)	0.156	0.147	0.129
		R^2	0.987	0.988	0.997
		RMSE	0.249	0.133	0.067
		SSE	0.248	0.053	0.009
	Freundlich	K_F (mg.g^{-1})(L.mg^{-1})$^{1/n}$	2.385	1.946	1.570
		n	4.080	4.302	4.470
		R^2	0.939	0.934	0.956
		RMSE	0.535	0.305	0.251
		SSE	1.143	0.280	0.126
	Temkin	K_T (L.mg^{-1})	2.940	3.012	2.860
		b_T (kJ.mol^{-1})	1.923	2.586	3.345
		R^2	0.980	0.960	0.983
		RMSE	0.308	0.239	0.155
		SSE	0.381	0.172	0.048
	Dubinin-Radushkevich (D-R)	K_{DR} (mol^2.kJ^{-2})	2.01	5.35	5.87
		q_{DR} (mg.g^{-1})	6.119	4.898	4.089
		E (kJ.mol^{-1})	0.499	0.306	0.292
		R^2	0.700	0.898	0.909
		RMSE	1.188	0.379	0.363
		SSE	5.642	0.431	0.263

Also, the Langmuir separation factor (R_L) as a function of initial concentration at 298, 303 and 313 K is shown in Figure 17. All the values were between 0 and 1 indicating that the adsorption process is favorable for both Fe-BTC and ZIF-8. However, in the case of Fe-BTC, the values of R_L at higher temperatures were smaller than those at lower temperatures, while the opposite was true for ZIF-8, hence, confirming the conclusions from the calculated q_m at different temperatures. In addition, all of the n values in the Freundlich isotherm were greater than unity which means $(1/n)<1$; hence, the adsorption of MO on Fe-BTC and ZIF-8 is favorable. Finally, the values of the mean adsorption energy (E) calculated from the D-R isotherm (Table 5) in both cases suggest that the adsorption of MO proceeds through physical adsorption.

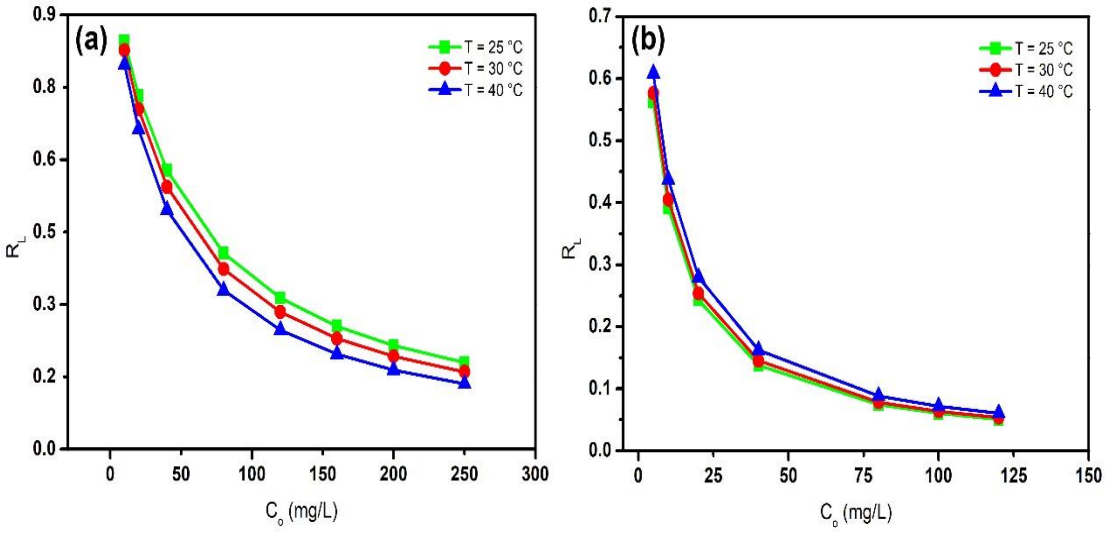

Figure 17: Plot of the Langmuir dimensionless separation factor (R_L) vs. C_o at different temperatures for (a) Fe-BTC and (b) ZIF-8.

3.2.8 Adsorption thermodynamics. In order to obtain meaningful values for the thermodynamic parameters, the value of K_{eq} has to be estimated properly. Since the Langmuir isotherm model was the best among the four models used in fitting the experimental data, the Langmuir constant (K_L) was used to estimate the equilibrium constant (K_{eq}) using the method suggested by Zhou and Zhou [145].

K_L is converted to a dimensionless constant by multiplying it by the molecular weight of MO (327.33 g.mol^{-1}), then by 55.5, then by 1000.

The results of the thermodynamic calculations are listed in Table 6, and the Van't Hoff plot used to estimate ΔH°, and ΔS° of MO adsorption on Fe-BTC and ZIF-8 is presented in Figure 18. The negative $\Delta G°$ values for both Fe-BTC and ZIF-8 reflects the spontaneous nature of the adsorption process under the experimental conditions. For Fe-BTC, the positive $\Delta H°$ value (16.86 kJ.mol^{-1}), confirms the endothermic adsorption of MO over Fe-BTC. This behavior may be attributed to the enhanced mobility of MO molecules from the bulk solution towards the Fe-BTC surface with increasing temperature. Also, at a higher temperature, MO molecules may gain more energy to interact with the active sites at the adsorbent's surface [146]. The endothermic adsorption of MO and other dyes using MOFs have been reported in the literature [73], [75], [76], [97]. In contrast, the negative $\Delta H°$ (-9.94 kJ.mol^{-1}) for ZIF-8 confirms the exothermic MO adsorption. The calculated absolute values of $\Delta H°$ are less than 40 kJ.mol^{-1}, which indicates that MO adsorption over Fe-BTC and ZIF-8 proceeds in a physical adsorption mechanism [101], [102]. This was also confirmed by the results of the D-R isotherm model. In addition, the positive values of $\Delta S°$ (162.4 and 90.2 J.mol^{-1}.K^{-1} for Fe-BTC and ZIF-8, respectively) reflects the increased disorder of the system at the solid-solution interface. This is due to the increased mobility of water molecules when the solvated MO molecules move from the bulk solution to the surface of the adsorbent. Also, in the case of Fe-BTC, the number of pre-adsorbed water molecules released from the surface of the adsorbent is more than the number of MO molecules adsorbed (i.e., the adsorption of a single MO molecule desorbs several water molecules due to larger MO molecule size compared to water), hence, $\Delta S°$ for Fe-BTC is larger than ZIF-8. This reveals that entropy change is a major driving force of MO adsorption on Fe-BTC.

Table 6: Thermodynamic parameters of MO adsorption over Fe-BTC and ZIF-8.

MOF	***T* (K)**	**$\Delta G°$ (kJ.mol^{-1})**	**$\Delta H°$ (kJ.mol^{-1})**	**$\Delta S°$ (J.mol^{-1}.K^{-1})**	**R^2**
Fe-BTC	298	-31.50	16.86	162.4	0.9931
	303	-32.37			
	313	-33.94			
ZIF-8	298	-36.81	-9.94	90.2	0.9984
	303	-37.28			
	313	-38.16			

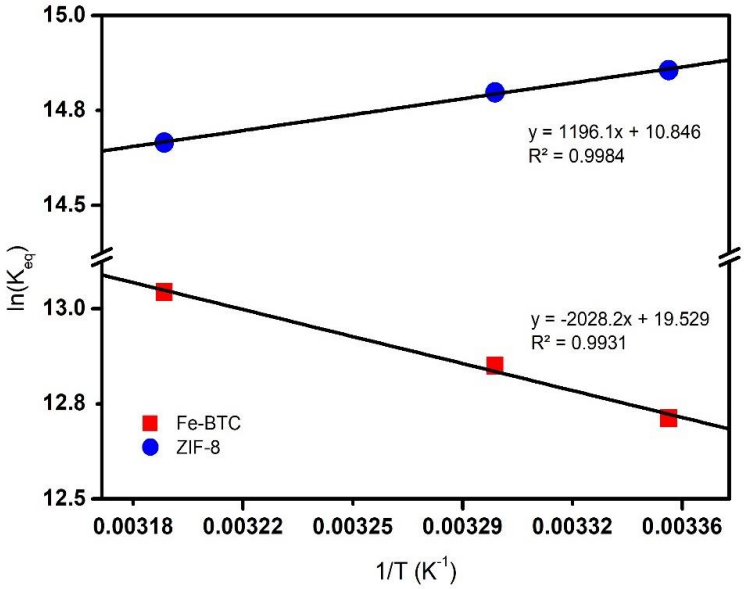

Figure 18: Van't Hoff plot to obtain ΔH° and ΔS° of MO adsorption on Fe-BTC and ZIF-8.

3.2.9 Desorption and regeneration of MOFs. Regeneration and reusability of an adsorbent are important aspects for commercial feasibility. In this work, a simple method of washing with ethanol was utilized to regenerate MO-loaded MOFs. After MO adsorption (C_o is 15 mg/L and m is 200 mg), Fe-BTC was separated from the solution by centrifugation (6000 rpm for 30 min), while ZIF-8 was separated using vacuum filtration. Then, the MO-loaded MOFs were washed by ethanol several times at room temperature until no orange color was observed in the ethanol solution. Finally, the recovered MOFs were dried under vacuum at 100 °C and then reused for a second adsorption experiment.

The results showed that both Fe-BTC and ZIF-8 could be generated easily using ethanol. For Fe-BTC the drop in removal efficiency was 12% (99% to 87%) compared to 16% (61% to 51%) for ZIF-8. However, in the case of Cu-BTC, regeneration attempts were unfruitful. These results show that Fe-BTC could have the potential for dye adsorption from wastewater.

3.2.10 Factorial design analysis. The factors selected for the experimental design were the type of MOF, the dosage of MOF, and the initial concentration.

For the type of MOF factor, only Fe-BTC and ZIF-8 were considered since the structure of Cu-BTC was proven to be unstable under the experimental conditions.

Table 7 presents the high and low levels for the 2^3 factorial design. In total, 16 experiments were carried out. The higher level was designated as '+1' and the lower level was designated as '-1'. For the type of MOF, ZIF-8 was assigned as the lower level since it had lower removal efficiency than Fe-BTC. The factorial design matrix (codified variables) along with the response values for MO removal efficiency are summarized in Table 8. Figure 19 illustrates the mean of the experimental results for the respective low and high levels of each factor.

Table 7: Factors and levels used in the factorial design.

Factor	**Code**	**Low Level (-1)**	**High Level (+1)**
Type of MOF	A	ZIF-18	Fe-BTC
Dosage (mg)	B	100	200
Initial Concentration (mg/L)	C	5	15

Table 8: Factorial design matrix and the experimental response results for MO removal efficiency.

Run	**A**	**B**	**C**	**MO Removal Efficiency (%)**
1	-1	+1	+1	87.3
2	-1	-1	-1	88.9
3	+1	+1	+1	99
4	+1	-1	-1	96.9
5	-1	-1	+1	61.5
6	-1	+1	-1	97.2
7	-1	-1	-1	88.6
8	+1	-1	+1	90.9
9	-1	+1	+1	86.9
10	+1	+1	-1	100
11	+1	-1	-1	96.8
12	+1	+1	-1	100
13	+1	+1	+1	98.1
14	+1	-1	+1	90.9
15	-1	-1	+1	66
16	-1	+1	-1	97.2

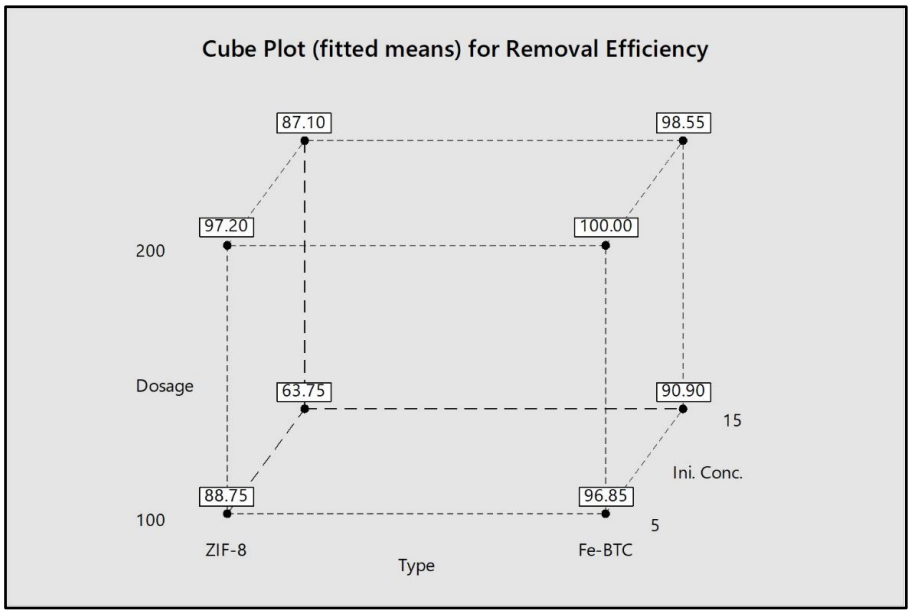

Figure 19: Cube plot for MO removal efficiency.

Analysis of variance (ANOVA) was conducted to examine the reliability of the model describing the response as a function of the factors. ANOVA shows whether the variations related to the model are significant compared to the variations of the experimental results or not [147]. Analyses were done using Fisher's test (F-value) and p-values to determine the significance of the regression coefficients of the main effects and the interaction effects. In general, p-values<0.05 are considered as potentially significant [148]. The ANOVA results are shown in Table 9. The contribution of the main factors and their interactions to the model are shown in Table 9 as well. From the p-values, it can be seen that the main factors (A, B, and C), their 2-way interactions (AB, AC, and BC), and their 3-way interactions (ABC) are statistically significant to the removal efficiency with 95% confidence level. In addition, the model presented a high coefficient of determination (R^2 = 0.9945), fitting the statistical model quite well. This value implies that 99.45% of the variations in the removal efficiency can be explained by the model while only 0.55% of the variations are not explained. The coefficients and the effects of the main factor and their interactions in the model are presented in Table 10. The relative importance of the main factors and their interactions can be determined from the absolute values in the "Effect" column. It can be seen that the order of the effects of the factors and their interactions in the model is ABC < BC < AB < AC < C < B < A. Meanwhile, the positive values of the effects reveal that as

the level of the factor increases the removal efficiency increases, while the negative values imply the opposite (i.e., increasing the level of the factor decreases the removal efficiency).

Table 9: Analysis of variance (ANOVA) results for *RE*.

Source	DF	Sum of squares	Contribution	Adjusted Sum of Squares (Adj. SS)	Adjusted mean Squares (Adj. MS)	F-Value	P-Value
A	1	612.6	31.39%	612.6	612.6	459.7	0.000
B	1	453.7	23.25%	453.7	453.7	340.5	0.000
C	1	451.6	23.14%	451.6	451.6	338.9	0.000
AB	1	110.2	5.650%	110.3	110.3	82.74	0.000
AC	1	191.8	9.830%	191.8	191.8	144.0	0.000
BC	1	94.09	4.820%	94.09	94.09	70.61	0.000
ABC	1	27.04	1.390%	27.04	27.04	20.29	0.002

Table 10: Estimated regression coefficients of the factors and their effects on MO removal.

Term	Effect	Coefficient	P-Value
Constant		90.39	0.000
A	12.38	6.188	0.000
B	10.65	5.325	0.000
C	-10.63	-5.312	0.000
AB	-5.250	-2.625	0.000
AC	6.925	3.463	0.000
BC	4.850	2.425	0.000
ABC	-2.600	-1.300	0.002

The relative importance of the main factors and their interactions was also observed on the Pareto chart (Figure 20). A t-test was performed to determine whether the calculated effects were significantly different from zero. For the 95% confidence level, the t-value was 2.31 (the vertical reference line). The values that exceed the reference line are considered significant [149]. According to Figure 20, all main factors and their interactions were significant at the level of 0.05 which corroborated the results from ANOVA.

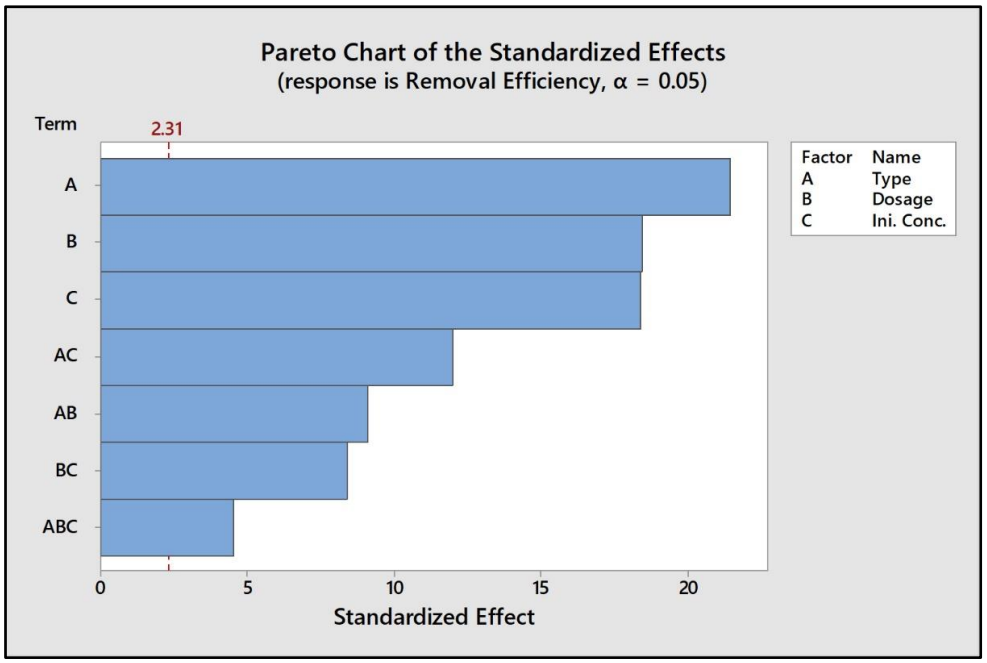

Figure 20: Pareto chart of the standardized effects.

The main effects of each factor on MO removal are shown in Figure 21. The main effects represent the change of the average removal efficiency between the high and low levels of each factor.

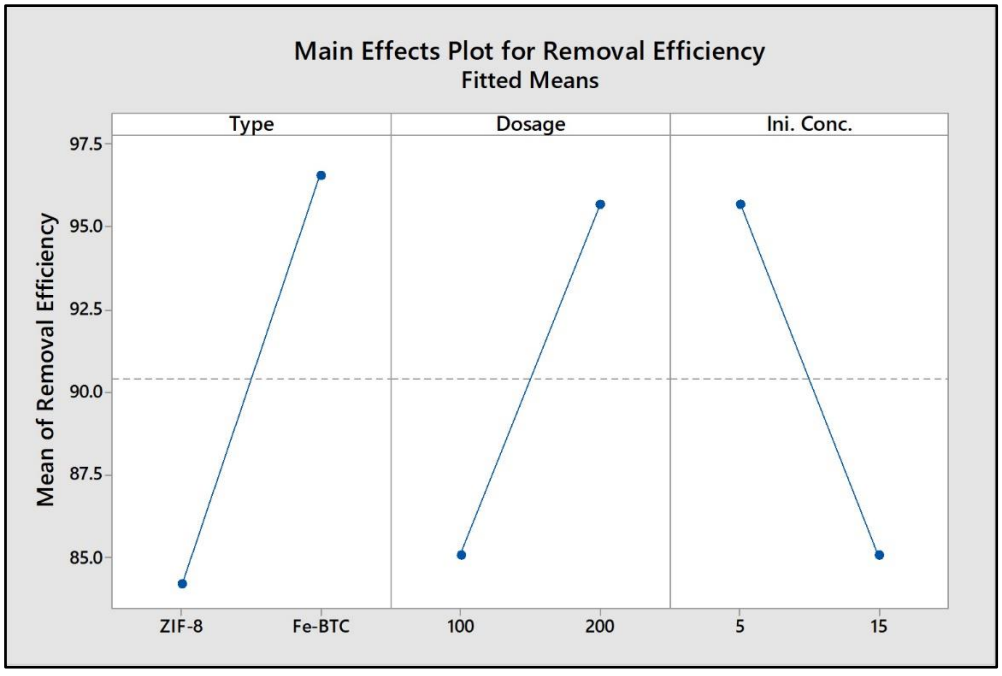

Figure 21: The main effects plot for MO removal efficiency.

The results show that changing the MOF from ZIF-8 to Fe-BTC had a positive effect on the removal efficiency. Similarly, increasing the dosage from 100 mg to 200 mg increased the removal efficiency while increasing the initial concentration decreased the removal efficiency. The results in Figure 21 are similar to the those reported in sections 3.2.2, 3.2.4, and 3.2.5 related to removal efficiencies, the effect of initial concentration, and the effect of dosage, respectively.

Figure 22 represents the interactions effects plot for MO removal efficiency. An interaction is considered prominent when the change in the removal efficiency from low to high levels of a factor is dependent on the level of a second factor (i.e., when the lines are not parallel or intersect) [149]. The plots indicate that interactions between the factors (AB, AC, and BC) were all significant as was confirmed by the ANOVA analysis and the Pareto chart. The AB and AC plots reveal that changing the MOF type had more effect at a lower dosage and higher initial concentration. On the other hand, the BC plot showed that increasing dosage from 100 mg to 200 mg had a higher effect at higher initial concentration. The multi-vari chart presented in Figure 23 reveals a comprehensive representation of the effects of interactions between experimental factors. It can be seen that changing the type of MOF from ZIF-8 to Fe-BTC has a more noticeable effect on removal efficiency at 100 mg dosage and 15 mg/L MO initial concentration.

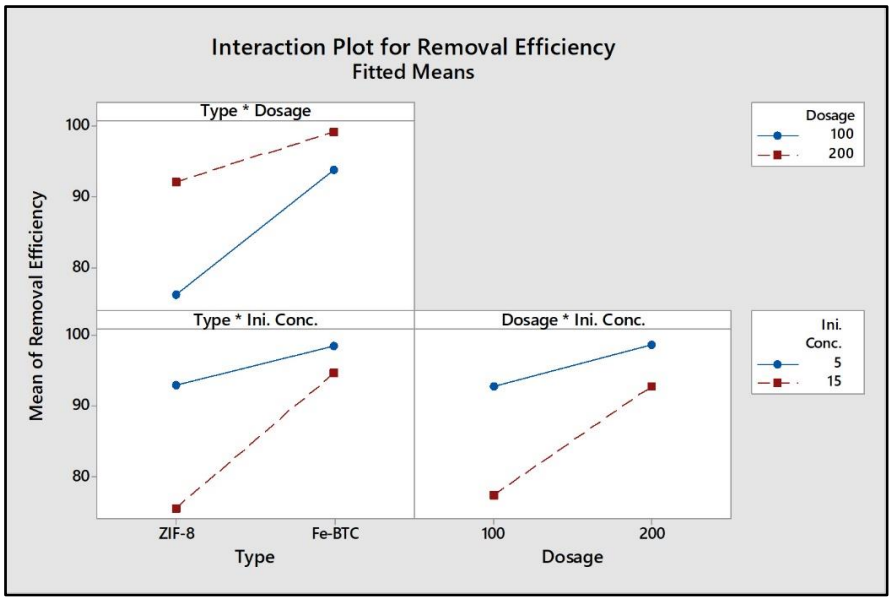

Figure 22: Interaction effects plot for MO removal efficiency.

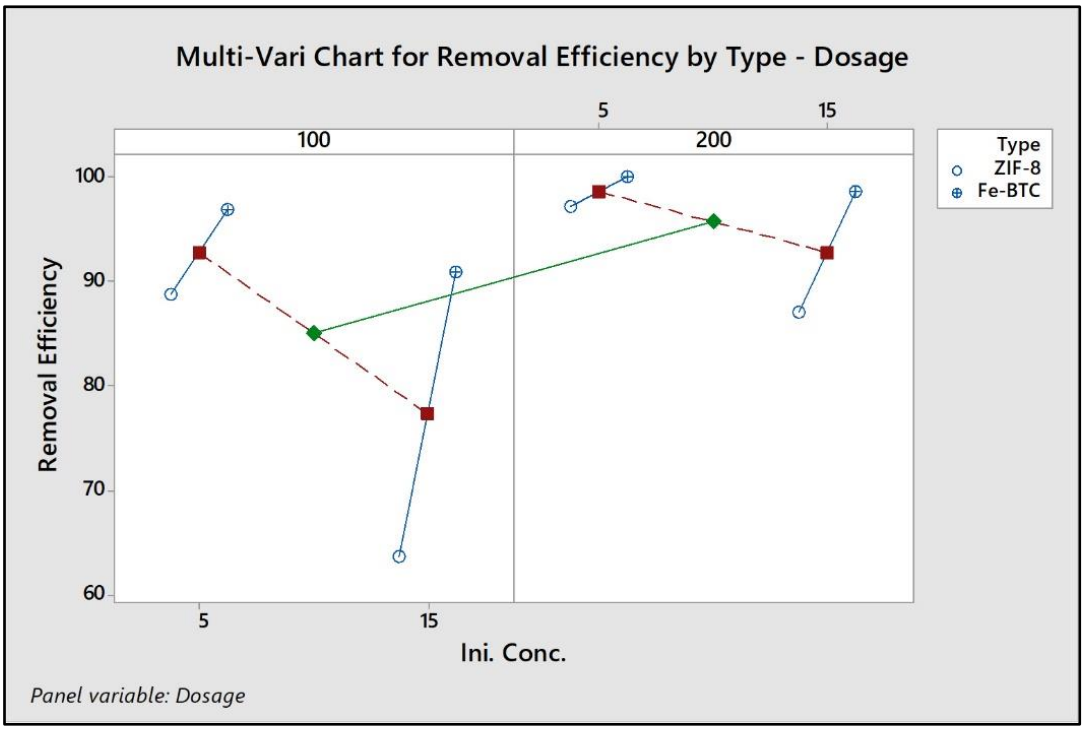

Figure 23: Multi-Vari chart plot for MO removal efficiency.

3.3 Summary

In summary, three MOFs (Fe-BTC, Cu-BTC, and ZIF-8) were used to study the removal of MO from aqueous solutions. The results showed that Fe-BTC exhibited the highest removal efficiency among the three adsorbents. Also, no significant change occurred in the internal structure of Fe-BTC and ZIF-8 after the adsorption process, and they were easily regenerated by washing with ethanol, whereas the crystal structure of Cu-BTC was damaged and could not be regenerated.

The maximum adsorption capacities for Fe-BTC and ZIF-8 were 114 and 7.56 mg/g, respectively. The pH effect experiments revealed that Fe-BTC and ZIF-8 could be used over a wide range of pH and maintain their removal efficiency and adsorption capacity. Additionally, electrostatic interactions and hydrogen bonding were concluded to be important in MO adsorption.

Also, the kinetic analysis of the experimental data showed that MO adsorption on Fe-BTC could be described by the Elovich model, whereas the PFO and PSO models best described the adsorption on ZIF-8.

The equilibrium isotherm study revealed that the experimental data could be best described by the Langmuir isotherm model. Thermodynamic data indicated that the adsorption process was spontaneous and entropically favored. It also showed that MO adsorption was endothermic in the case of Fe-BTC and exothermic in the case of ZIF-8.

Moreover, a 2^3 factorial design was utilized to study the effect of MOF type, dosage, and initial concentration on the MO removal efficiency. The statistical analysis revealed that the MOF type was the most significant factor followed by dosage and initial concentration. The 2-way and 3-way interactions were also found to be significant. The analysis indicated that the type of MOF and dosage had a positive effect on the removal efficiency, while the initial concentration had a negative effect.

Chapter 4. Fixed-Bed Column Adsorption of Methyl Orange Using Fe-BTC

In the second part of the thesis, a bench-scale fixed-bed column, packed with Fe-BTC is used for the removal of MO from aqueous solutions in a continuous setup. In this chapter, the performance and adsorption capacity of the column is studied by varying the bed height. Also, the breakthrough experimental data was fitted to kinetic breakthrough models, and the calculated parameters were reported.

4.1 Introduction

The removal efficiency and adsorption capacity of various adsorbents obtained from batch experiments are useful to determine their effectiveness under the considered experimental conditions. They also provide the fundamental understanding of dye adsorption mechanism, kinetic parameters, and the optimum process conditions. However, the data may not be applied to most of the treatment processes (e.g., continuous column operation) since contact time in these processes is not sufficient to achieve equilibrium [150], [151]. In addition, isotherm equilibrium data obtained from batch experiments are often difficult to apply directly in the design and scale-up of fixed-bed columns since a continuous flow column is not at equilibrium. Therefore, there is a need for fixed-bed column studies. Column adsorption experiments are for the study of adsorption dynamics. The most essential criterion in the design of adsorption system is the service time, known as column breakthrough. The breakthrough time and the shape of the concentration-time profile are essential for the design of an adsorption column. In this chapter, the performance of MO adsorption in a continuous fixed-bed column is investigated. Fe-BTC was selected as the adsorbent in the fixed-bed column since it demonstrated the best removal efficiency among the three MOFs considered in the batch study.

4.2 Experimental Setup

The experimental setup and the bench-scale column used for the fixed-bed adsorption studies are depicted in Figure 24. The adsorbent bed was created by packing known amounts of Fe-BTC (150 and 300 mg) in a transparent glass tube (1 cm diameter) to achieve particular bed heights. The bed was surrounded by layers of

deactivated glass wool (RESTEK, USA) and glass beads (4 mm diameter). The bottom layer provides support for the bed, while the top layer promotes liquid distribution across the column cross-section. Before adsorption experiments, a control experiment was carried out, and the results indicated that the adsorption of MO on glass wool and glass beads was negligible. The column was fed manually with the MO solution of 15 mg/L concentration (C_o). In order to ensure a constant flow rate (Q = 4.5 mL/hr), a constant level of the hydrostatic head above the fixed-bed was maintained. Then, the performance of the column was evaluated at room temperature by collecting samples from the column effluent at different time intervals and measuring the concentration (C_t) using the UV-Vis spectrophotometer. The total volume of the collected effluent was also recorded with each sample. The obtained concentration data were normalized with respect to the influent concentration and plotted against the operating time and collected volume to obtain the breakthrough curves.

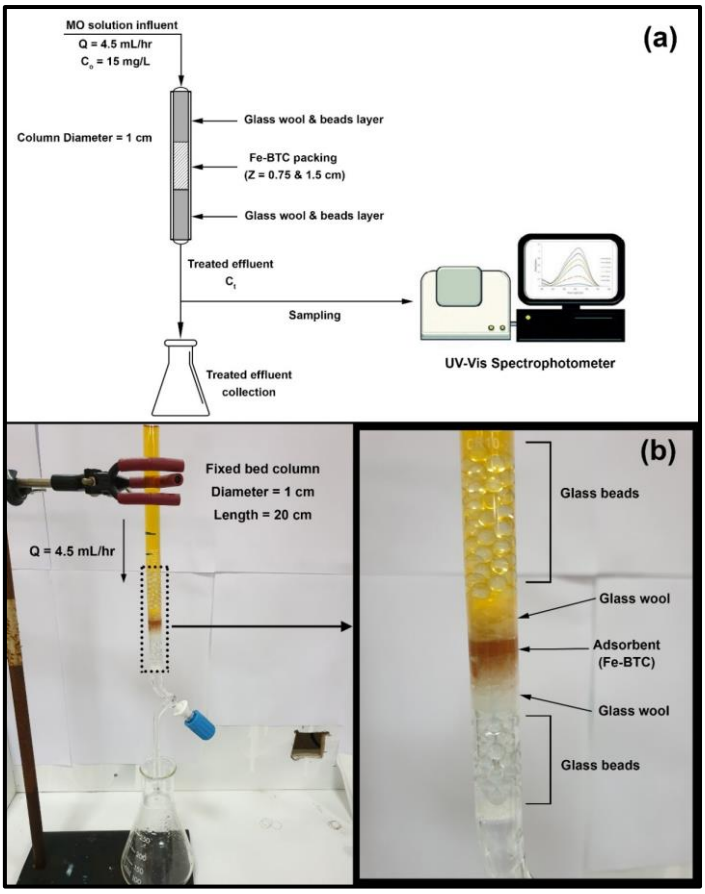

Figure 24: (a) Schematic representation of the experimental setup and (b) Image of the fixed-bed column and the adsorbent packing.

4.3 Theoretical Background

4.3.1 Breakthrough theory. In fixed-bed column process, the operating time to adsorb contaminants, such that the effluent outlet complies with certain allowable levels of concentration is called breakthrough time, and it can be expressed by a breakthrough curve (BTC). A breakthrough plot is usually expressed in terms of the normalized concentration (i.e., C_t/C_o) as a function of time or effluent volume [152]. A typical BTC is shown in Figure 25.

Considering a vertical downward flow, initially, the bed is completely free of the pollutant. Then, once the liquid flow is initiated through the column, the pollutant is gradually transferred to the adsorbent, and most of the mass transfer takes place near the inlet of the bed, where the fluid contacts the adsorbent. As the process progresses, the solid near the inlet is nearly saturated, and Most of the mass transfer takes place farther from the inlet. The region of the column where most of the concentration reduction occurs is called the mass transfer zone (*MTZ*). When the *MTZ* reaches the end of the column, the concentration of the pollutant in the effluent increases until it reaches a threshold level. This level is called the breakthrough point. Then, as time passes, the concentration of the pollutant in the effluent continuous to increase until it reaches the exhaustion point (i.e., the bed is close to full loading) and finally becomes fully saturated. Depending on the specific application of the column, different levels of breakthrough and exhaustion can be used.

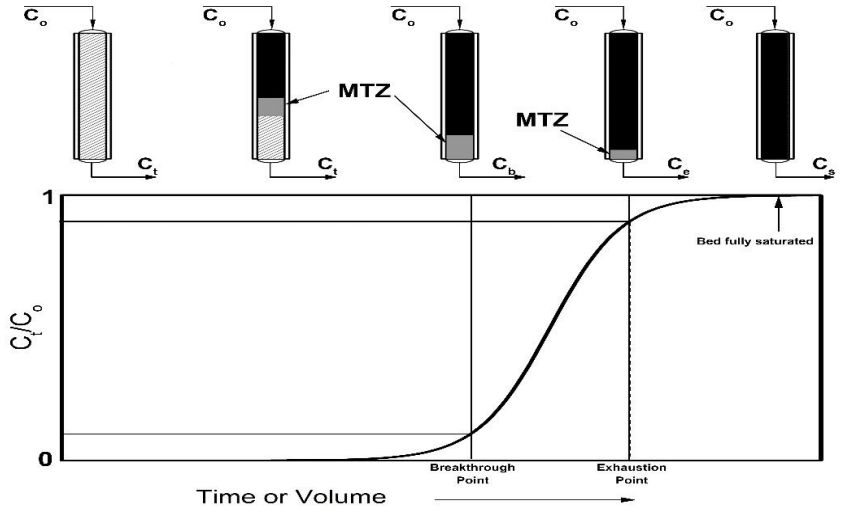

Figure 25: Schematic of a typical breakthrough curve (BTC).

4.3.2 Evaluation of fixed-bed column operation parameters. To evaluate the performance of the fixed bed the breakthrough time (t_b) and the exhaustion time (t_e) were set as the time to reach $\left(C_t/C_o\right)\big|_b = 0.1$ and $\left(C_t/C_o\right)\big|_e = 0.9$, respectively. From the experimental data of the breakthrough curve, the total amount of MO adsorbed at the exhaustion point (m_{ad}) was calculated using equation (19).

$$m_{ad} = QC_o \int_0^{t_e} \left(1 - \frac{C_t}{C_o}\right) dt \tag{19}$$

where Q is the inlet volumetric flow rate, C_o is the influent concentration, and C_t/C_o is the ratio of the effluent concentration to the influent concentration.

Also, the total amount of MO fed to the column at the exhaustion point (m_{tot}) is calculated using equation (20).

$$m_{tot} = QC_o t_e \tag{20}$$

From the values of m_{ad} and m_{tot}, the bed removal efficiency (RE_{bed}) is calculated as follows:

$$RE_{bed} = \frac{m_{ad}}{m_{tot}} \times 100 \tag{21}$$

The column maximum adsorption capacity, also known as the equilibrium adsorption capacity (q_{max}) is calculated using equation (22).

$$q_{max} = \frac{m_{ad}}{m} \tag{22}$$

where m is the mass of the adsorbent packed in the column.

Also, the empty bed contact time ($EBCT$) which is the time during which the liquid feed is in contact with the adsorbent in the column, assuming that the liquid flows through the bed at the same velocity, is given by:

$$EBCT = \frac{Z \times A_{bed}}{Q} \tag{23}$$

where Z is the bed height in the column and A_{bed} is the cross-section area of the bed.

Finally, the length of the mass transfer zone (MTZ) in the bed is calculated by equation (24).

$$MTZ = Z \times \left(1 - \frac{t_b}{t_e}\right) \tag{24}$$

4.3.3 Kinetic modeling of fixed-bed breakthrough. Various kinetic models have been proposed to predict the breakthrough curves in fixed-bed adsorption columns. These models can be used to determine the kinetic parameters and adsorption capacity of the fixed-bed which can be used to scale-up the fixed-bed adsorption process. In this work, breakthrough data were analyzed using Thomas [153], Yoon-Nelson [154], Clark [155], and modified dose response (MDR) [156] models.

Thomas model is one of the most widely used kinetic models to predict the column breakthrough curve. The model's assumptions are: (1) the adsorption is best described by the Langmuir isotherm; (2) the adsorption rate follows second-order reversible kinetics; (3) no axial dispersion is considered [153]. Thomas model also assumes that the constant separation factor (R_L) applies to either favorable or unfavorable isotherm [157]. The model is expressed in equation (25).

$$\frac{C_t}{C_o} = \frac{1}{1 + exp\left[K_{TH}\left(\frac{q_{TH}m}{Q} - C_o t\right)\right]} \tag{25}$$

where K_{TH} is the Thomas rate constant, q_{TH} is the equilibrium (maximum) adsorption capacity predicted by the Thomas model, m is the amount of adsorbent in the column, C_o influent concentration, C_t is the effluent concentration, and Q is the flow rate, and t is the sampling time.

Yoon-Nelson (Y-N) model is considered the less complicated column model since it requires no detailed data about the characteristics of the adsorbate, the type of adsorbent, and the physical properties of adsorption bed. The model is based on the theory of adsorbate probability and assumes no axial dispersion [158]. Equation (26) describes the model as follows:

$$\frac{C_t}{C_o} = \frac{1}{1 + exp\left[K_{YN}(\tau - t)\right]} \tag{26}$$

where K_{YN} is the Yoon-Nelson rate constant and τ is the time required for 50% adsorbate breakthrough.

Clark model given in equation (27) is based on bed differential mass balance in combination with the assumption that adsorption fits the Freundlich isotherm [155].

$$\frac{C_t}{C_o} = \left(\frac{1}{1 + Ae^{-rt}}\right)^{\frac{1}{n-1}} \tag{27}$$

where A and r are the Clark model constants and n is the Freundlich isotherm constant. The value of n was determined from the batch study at 25 °C which is reported in section 3.2.7 (n = 1.864)

Finally, equation (28) presents the MDR model which was proposed by Yan et al. [156]. This model minimizes the error introduced from the use of the Thomas model at lower or higher operating times of the breakthrough curve [156].

$$\frac{C_t}{C_o} = 1 - \frac{1}{1 + \left(\frac{C_o Q t}{q_{MDR} m} \right)^{a_{MDR}}} \tag{28}$$

where a_{MDR} is the MDR model constant, and q_{MDR} is the equilibrium (maximum) adsorption capacity predicted by the MDR model.

4.4 Results and Discussion

4.4.1 Fixed-bed column operation performance. Figure 26 shows the visual change in the Fe-BTC packing inside the column as it becomes saturated. Also, Figure 27 presents both types of BTCs obtained from MO adsorption on Fe-BTC for different bed heights at a flow rate of 4.5 mL/hr and influent MO concentration of 15 mg/L.

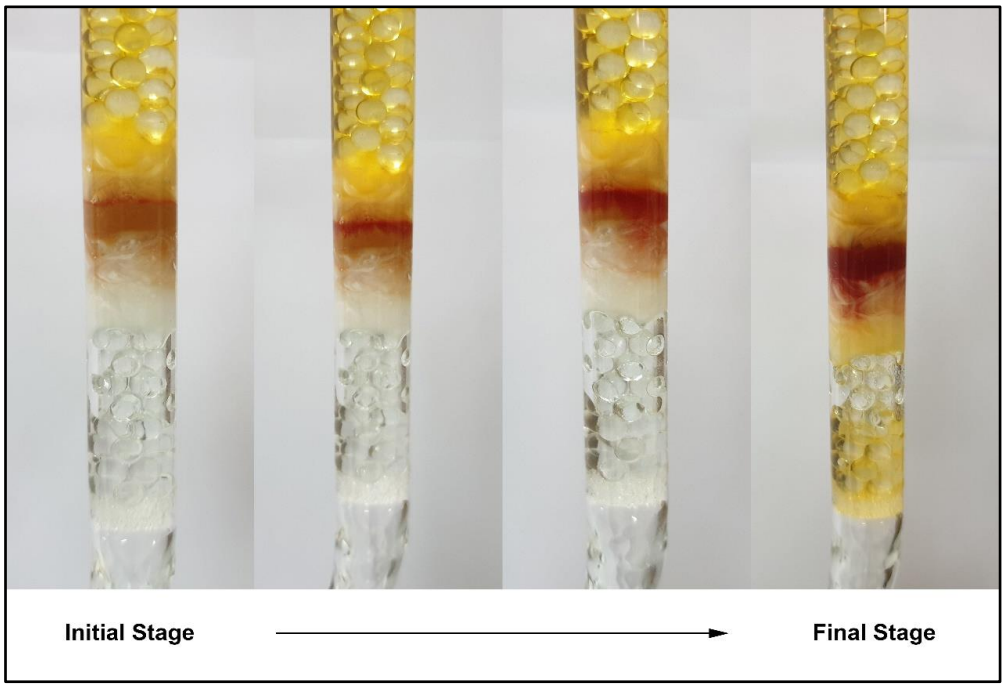

Figure 26: Visual change in the Fe-BTC packing with time.

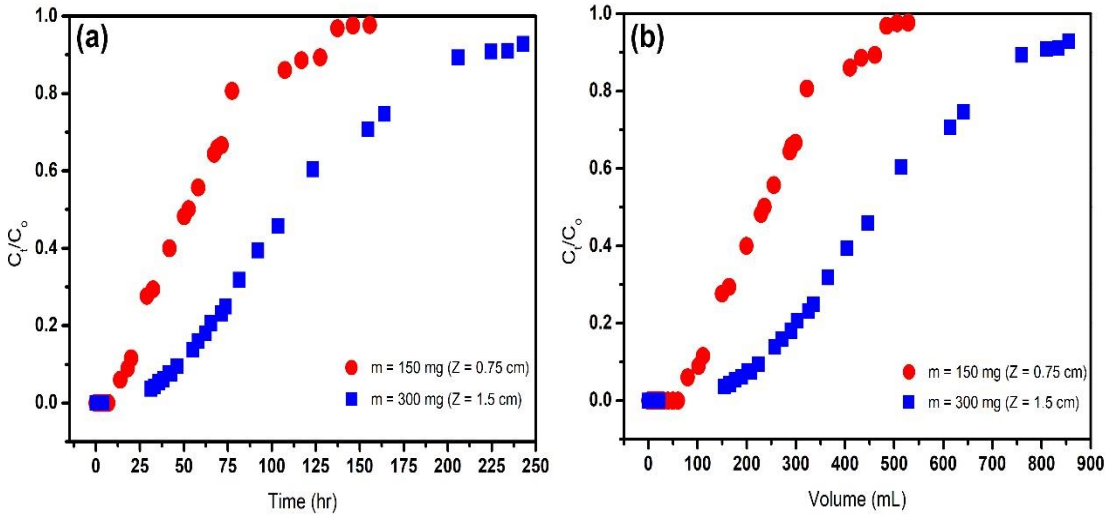

Figure 27: BTCs of MO adsorption on Fe-BTC fixed-bed column as function of (a) time and (b) treated volume (C_o = 15 mg/L, Q = 4.5 mL/hr)

Also, the calculated fixed-bed parameters are shown in Table 11. The results revealed that by increasing the bed height, the breakthrough curves shifted to the right which means breakthrough and exhaustion times increased. By increasing the bed height, the total amount of MO adsorbed in the fixed-bed (m_{ad}), the removal efficiency (RE_{bed}) and the maximum bed adsorption capacity (q_{max}) also increased. An increase in *EBCT*, *MTZ*, $V_{treated}$ (treated effluent volume), and $t_{50\%}$ (time required for 50% breakthrough) was also observed. These results are expected; as bed height is increased the surface area of the adsorbent that could offer adsorption sites is also increased, which means larger total adsorption capacity. Moreover, with longer bed height the contact time in the bed is increased, and in turn, the removal efficiency increased, which means more volume of effluent can be treated. Similar observations were reported in the literature [159], [160].

Table 11: Fixed-bed column parameters obtained at different bed heights (C_o = 15 mg/L, Q = 4.5 mL/hr).

Bed Height (cm)	t_b **(hr)**	t_e **(hr)**	m_{ad} **(mg)**	m_{tot} **(mg)**	RE_{bed} **(%)**	q_{max} **(mg/g)**	***EBCT*** **(min)**	***MTZ*** **(cm)**	$V_{treated}$ **(mL)**	$t_{50\%}$ **(hr)**
0.75	20.0	127.5	3.03	8.61	35.2	20.2	7.85	0.63	106	52.8
1.50	46.2	205.9	6.49	13.9	46.7	21.6	15.7	1.16	228	109.2

4.4.2 Kinetic modeling of fixed-bed breakthrough. The calculated model parameters, maximum adsorption capacities, and the respective values of R^2, *RMSE*, and *SSE* are summarized in Table 12. It was found that Thomas and Y-N models had the same fitting coefficients (R^2, *RMSE*, and *SSE*), and the Clark model was marginally better. The MDR model had the best fitting coefficients (highest R^2 and lowest *RMSE*, and *SSE*). The comparisons of the experimental and the predicted BTCs at different bed heights are shown in Figure 28.

The results of the Thomas model showed that the maximum adsorption capacity (q_{TH}) increased as the bed height increased, while the Thomas rate constant (K_{TH}) decreased. This can be attributed to the availability of additional adsorption sites when bed height is increased which results in longer breakthrough time [161], [162]. Similar to the Thomas model, the Y-N rate constant (K_{YN}) decreased with an increase in bed height, whereas the value of τ increased. The increase in τ is expected since larger bed height will increase contact time in the bed. Hence, the bed breakthrough is delayed which means it will take longer time to reach 50% breakthrough [163], [164].

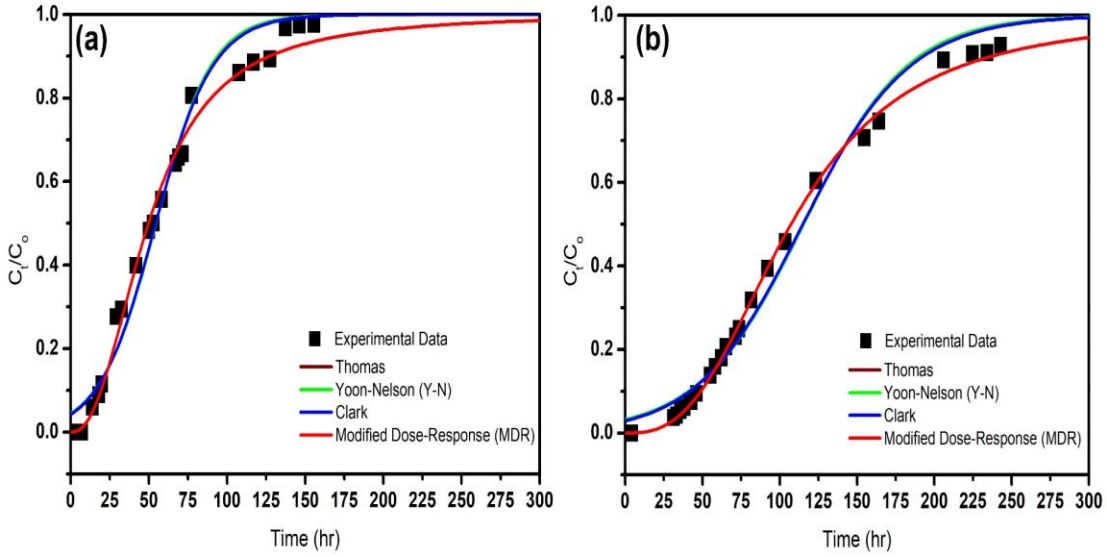

Figure 28: Comparison between the experimental and the predicted BTCs for (a) Z = 0.75 cm and (b) Z = 1.5 cm.

Also, it can be noticed that the values of τ in Table 12 were satisfactorily close to the experimentally determined time to achieve 50% breakthrough ($t_{50\%}$) presented in Table 11. Moreover, the results of the Clark model showed that the value of A increased with increasing bed height while the value of r decreased.

Table 12: Summary of the calculated parameters of the kinetic models at different bed heights.

BTC Model	Parameters	Z (cm)	
		0.75	**1.50**
Thomas	q_{TH} (mg.g^{-1})	24.58	25.97
	K_{TH} (mL.mg^{-1}.hr^{-1})	3.732	1.972
	R^2	0.980	0.986
	RMSE	0.054	0.039
	SSE	0.080	0.049
Yoon-Nelson (Y-N)	K_{YN} (hr^{-1})	0.056	0.030
	τ (hr)	54.6	115.4
	R^2	0.980	0.986
	RMSE	0.054	0.039
	SSE	0.080	0.049
Clark	A	14.38	20.25
	r (hr^{-1})	0.053	0.028
	R^2	0.982	0.988
	RMSE	0.052	0.036
	SSE	0.072	0.042
Modified Dose Response (MDR)	q_{MDR} (mg.g^{-1})	22.39	24.14
	a_{MDR}	2.344	2.801
	R^2	0.995	0.999
	RMSE	0.028	0.012
	SSE	0.021	0.004

Furthermore, the calculated maximum adsorption capacity from the MDR model (q_{MDR}) increased with the increase in the bed height similar to the Thomas model, and the value of a_{MDR} increased as well. The values of q_{MDR} were well close to the experimentally determined maximum bed adsorption capacity (q_{max}).

Finally, it can be noticed from Figure 28 that at the initial operating time the predicted C_t/C_o values from the Thomas, Y-N, and Clark models were all greater than zero, which is not in agreement with the experimental data. The MDR model was the only one to fit the experimental data at the initial operating time when the values of C_t/C_o were zero or very close to zero. The overestimation of C_t/C_o leads to predicting that the breakthrough concentration is reached earlier. As a result, the column service time is shortened during operation, and the actual column capacity will not be fully utilized [156].

4.5 Summary

A fixed-bed column was packed with Fe-BTC to study the performance of MO adsorption. The influent MO solution concentration was 15 mg/L, and the influent flow

rate was 4.5 mL/hr. The adsorption performance was investigated at two different bed heights (0.75 and 1.5 cm). The results showed that as bed height increased the breakthrough and exhaustion times increased. The increase in bed height leads to more adsorbent surface exposed to flow, and this leads to an increase in maximum adsorption capacity, removal efficiency, and treated effluent volume.

Furthermore, the experimental data were fitted using four kinetic breakthrough models, namely, Thomas, Yoon-Nelson (Y-N), Clark and the Modified dose response (MDR). The results showed that all models were suitable in describing the experimental data with the MDR being the best among them. The rate constants K_{TH}, K_{YN}, and r from Thomas, Y-N, and Clark models, respectively decreased with the increase in bed height. Also, the Y-N model was suitable in predicting the time for 50% breakthrough. Finally, the maximum adsorption capacities calculated from Thomas and MDR models increased with increasing bed height. However, the values of the MDR model were closer to the experimental values than the Thomas model.

Chapter 5. Conclusions and Recommendations

This chapter summarizes the main conclusions of this thesis and presents some recommendations for future research.

5.1 Conclusions

This thesis investigates the feasibility of using metal organic frameworks (MOFs) as promising adsorbents to remove methyl orange (MO) from aqueous solutions. In this thesis, MOFs were characterized and tested for MO adsorption under various experimental conditions in batch and continuous setups. The following are the major conclusions of the thesis.

5.1.1 Batch study conclusions. The following are the major conclusions from the batch study of MO adsorption using MOFs:

1. The characterizations tests confirmed that methyl orange was successfully adsorbed by Fe-BTC and ZIF-8 and that their structure remained intact after adsorption, while the structure of Cu-BTC was confirmed to be damaged after adsorption
2. Among the three MOFs considered, Fe-BTC had the highest removal efficiency (>90%). The adsorption was rapid, and the equilibrium could be achieved in 60 min.
3. The adsorption capacity was found to increase with the increase in MO initial concentration, and decrease with increase in MOF dosage, while removal efficiency decreased with increase in MO initial concentration and increased with increase in MOF dosage.
4. The pH effect experiments revealed that Fe-BTC and ZIF-8 could be used over a wide range of pH and maintain their removal efficiency and adsorption capacity.
5. The kinetic study showed that MO adsorption on Fe-BTC could be described by the Elovich model (R^2>0.99), whereas the PFO and PSO models best described the adsorption on ZIF-8 (R^2>0.98).
6. Langmuir isotherm model was found to best fit the experimental data for both Fe-BTC and ZIF-8. The calculated maximum monolayer adsorption capacities were 100.3, 105, and 114 mg/g for Fe-BTC compared to 7.56, 5.62, and 4.65 mg/g for ZIF-8 at 298, 303 and 313 K, respectively.

7. The thermodynamic results indicated that adsorption was endothermic in the case of Fe-BTC ($\Delta H°$ was 16.86 kJ/mol) and exothermic in the case of ZIF-8 ($\Delta H°$ was -9.94 kJ/mol).
8. Both Fe-BTC and ZIF-8 were easily regenerated by a simple washing using ethanol at room temperature.

5.1.2 Fixed-bed study conclusions. The following are the major conclusions from the MO adsorption experiments in Fe-BTC fix-bed column:

1. A fixed-bed column packed with Fe-BTC was successfully used in the removal of MO from aqueous solutions.
2. When the height of the fixed-bed increased, the breakthrough time increased. This lead to an increase in the removal efficiency and maximum bed adsorption capacity. This is because more surface of Fe-BTC was exposed to MO flow.
3. The breakthrough time at 0.75 cm bed height was 20.0 hr while at 1.5 cm it was 46.2 hr. On the other hand, the exhaustion times were 127.5 and 205.9 hr at 0.75 and 1.5 cm bed height, respectively.
4. The bed removal efficiency was 35.2% and 46.7% at 0.75 cm and 1.5 cm bed height, respectively. Also, the bed maximum adsorption capacity was 20.2 and 21.6 mg/g at 0.75 cm and 1.5 cm bed height, respectively.
5. The total volume of the treated MO solution at breakthrough increased as the bed height increased (106 mL at 0.75 cm and 228 mL at 1.5 cm)
6. The application of breakthrough curve models showed that all the models that were used (Thomas, Yoon-Nelson, Clark, and MDR) were suitable in describing the experimental data with the MDR being the best among them (R^2>0.99).
7. The calculated bed maximum adsorption capacities from the MDR model were 22.39 and 24.14 mg/g at 0.75 and 1.5 cm bed height, respectively.

5.2 Recommendations for Future Research

Based on the research done in this thesis and its findings, the following are recommendations for future research:

1. Dye wastewater from various industries always consists of more than a single dye and could be mixed with filler materials. Hence the removal of dyes from

wastewater produced from different industries needs extensive investigation under different operating conditions to assess the performance of adsorption processes.

2. Based on the literature review, most of the dye adsorption studies using MOFs were based on batch adsorption experiments. Very few continuous column studies were reported. Therefore, it is recommended that more focus should be directed to column adsorption studies which give more insight into the feasibility of utilizing MOFs on a commercial scale.
3. Since water stability is an essential criterion for selecting the ideal adsorbent, more efforts need to be directed towards studying the water stability of the various MOFs reported in the literature.
4. The mechanism of dyes adsorption on MOFs is complex and rarely reported properly in the literature. Therefore, more research should be focused on understanding the adsorption mechanism, and attempting to develop new models that could explain the adsorption mechanisms on MOFs.

References

[1] F. A. Caliman and M. Gavrilescu, “Pharmaceuticals, Personal Care Products and Endocrine Disrupting Agents in the Environment - A Review,” *CLEAN - Soil, Air, Water*, vol. 37, no. 4–5, pp. 277–303, Apr. 2009.

[2] M. Arslan, I. Ullah, J. A. Müller, N. Shahid, and M. Afzal, “Organic Micropollutants in the Environment: Ecotoxicity Potential and Methods for Remediation,” in *Enhancing Cleanup of Environmental Pollutants. Volume 1: Biological Approaches*, Cham, Switzerland: Springer International Publishing, 2017, pp. 65–99.

[3] Y. Luo *et al.*, “A review on the occurrence of micropollutants in the aquatic environment and their fate and removal during wastewater treatment,” *Sci. Total Environ.*, vol. 473–474, pp. 619–641, Mar. 2014.

[4] G. Booth, H. Zollinger, K. McLaren, W. G. Sharples, and A. Westwell, “Dyes, General Survey,” in *Ullmann’s Encyclopedia of Industrial Chemistry*, Weinheim, Germany: Wiley-VCH Verlag GmbH & Co. KGaA, 1985, pp. 73–124.

[5] C. C. Wang, J. R. Li, X. L. Lv, Y. Q. Zhang, and G. Guo, “Photocatalytic organic pollutants degradation in metal-organic frameworks,” *Energy Environ. Sci.*, vol. 7, no. 9, pp. 2831–2867, 2014.

[6] C. R. P. Fulong and T. R. Cook, “Sequestration of orange G and methylene blue from aqueous solutions using a Co(ii) coordination polymer,” *RSC Adv.*, vol. 7, no. 43, pp. 26532–26536, May 2017.

[7] A. Gürses, M. Açıkyıldız, K. Güneş, and M. S. Gürses, “Classification of Dye and Pigments,” in *Dyes and Pigments*, Cham, Switzerland: Springer International Publishing, 2016, pp. 31–45.

[8] F. I. Hai, K. Yamamoto, and K. Fukushi, “Hybrid Treatment Systems for Dye Wastewater,” *Crit. Rev. Environ. Sci. Technol.*, vol. 37, no. 4, pp. 315–377, May 2007.

[9] Q. Husain, “Potential Applications of the Oxidoreductive Enzymes in the Decolorization and Detoxification of Textile and Other Synthetic Dyes from Polluted Water: A Review,” *Crit. Rev. Biotechnol.*, vol. 26, no. 4, pp. 201–221, Jan. 2006.

[10] S. Chen, J. Zhang, C. Zhang, Q. Yue, Y. Li, and C. Li, “Equilibrium and kinetic studies of methyl orange and methyl violet adsorption on activated carbon derived from Phragmites australis,” *Desalination*, vol. 252, no. 1–3, pp. 149–156, Mar. 2010.

[11] J. Gao *et al.*, “Adsorption of methylene blue onto activated carbon produced from tea (Camellia sinensis L.) seed shells: kinetics, equilibrium, and thermodynamics studies,” *J. Zhejiang Univ. Sci. B*, vol. 14, no. 7, pp. 650–658, Jul. 2013.

[12] M. A. K. M. Hanafiah, W. S. W. Ngah, S. H. Zolkafly, L. C. Teong, and Z. A. A. Majid, “Acid Blue 25 adsorption on base treated Shorea dasyphylla sawdust: Kinetic, isotherm, thermodynamic and spectroscopic analysis,” *J. Environ. Sci.*, vol. 24, no. 2, pp. 261–268, Feb. 2012.

[13] R. T V, “Spatial Analysis and Characterisation of Lentic Ecosystems : A Case Study of Varthur Lake , Bangalore,” *Int. J. Ecol. Dev.*, vol. 9, no. W08, pp. 39–56, 2008.

[14] J.-Q. Jiang, “The role of coagulation in water treatment,” *Curr. Opin. Chem. Eng.*, vol. 8, pp. 36–44, May 2015.

[15] W. W. Eckenfelder, Jr, D. L. Ford, and A. J. Englande, “Coagulation, Precipitation, and Metals Removal,” in *Industrial Water Quality*, 4th ed., New York: McGraw-Hill, 2009, pp. 137–177.

[16] G. Tchobanoglous, F. L. Burton, and H. D. Stensel, “Primary Sedimentation,” in *Wastewater Engineering: Treatment & Reuse*, 4th ed., Boston: McGraw-Hill, 2003, pp. 396–411.

[17] W. W. Eckenfelder, Jr, “Sedimentation,” in *Industrial Water Pollution Control*, 3rd ed., Boston: McGraw-Hill, 2000, pp. 85–102.

[18] W. Somasiri, X.-F. Li, W.-Q. Ruan, and C. Jian, “Evaluation of the efficacy of upflow anaerobic sludge blanket reactor in removal of colour and reduction of COD in real textile wastewater,” *Bioresour. Technol.*, vol. 99, no. 9, pp. 3692–3699, Jun. 2008.

[19] Y. L. Pang and A. Z. Abdullah, “Current Status of Textile Industry Wastewater Management and Research Progress in Malaysia: A Review,” *CLEAN - Soil, Air, Water*, vol. 41, no. 8, pp. 751–764, Aug. 2013.

[20] H. S. Rai, M. S. Bhattacharyya, J. Singh, T. K. Bansal, P. Vats, and U. C. Banerjee, “Removal of Dyes from the Effluent of Textile and Dyestuff Manufacturing Industry: A Review of Emerging Techniques With Reference to Biological Treatment,” *Crit. Rev. Environ. Sci. Technol.*, vol. 35, no. 3, pp. 219–238, Mar. 2005.

[21] M. S. Khehra, H. S. Saini, D. K. Sharma, B. S. Chadha, and S. S. Chimni, “Biodegradation of azo dye C.I. Acid Red 88 by an anoxic–aerobic sequential bioreactor,” *Dye. Pigment.*, vol. 70, no. 1, pp. 1–7, Jul. 2006.

[22] M. P. Celia and S. Suruthi, “Textile dye degradation using bacterial strains isolated from textile mill effluent,” *Int. J. Appl. Res.*, vol. 2, no. 3, pp. 337–341, 2016.

[23] V. K. Gupta and Suhas, “Application of low-cost adsorbents for dye removal – A review,” *J. Environ. Manage.*, vol. 90, no. 8, pp. 2313–2342, Jun. 2009.

[24] R. Andreozzi, “Advanced oxidation processes for the treatment of mineral oil-contaminated wastewaters,” *Water Res.*, vol. 34, no. 2, pp. 620–628, Feb. 2000.

[25] V. Preethi, K. S. Parama Kalyani, K. Iyappan, C. Srinivasakannan, N. Balasubramaniam, and N. Vedaraman, “Ozonation of tannery effluent for removal of cod and color,” *J. Hazard. Mater.*, vol. 166, no. 1, pp. 150–154, Jul.

2009.

[26] T. Robinson, G. McMullan, R. Marchant, and P. Nigam, “Remediation of dyes in textile effluent: a critical review on current treatment technologies with a proposed alternative,” *Bioresour. Technol.*, vol. 77, no. 3, pp. 247–255, May 2001.

[27] M. Sundrarajan, G. Vishnu, and K. Joseph, “Ozonation of light-shaded exhausted reactive dye bath for reuse,” *Dye. Pigment.*, vol. 75, no. 2, pp. 273–278, 2007.

[28] H. Zhang, L. Duan, and D. Zhang, “Decolorization of methyl orange by ozonation in combination with ultrasonic irradiation,” *J. Hazard. Mater.*, vol. 138, no. 1, pp. 53–59, Nov. 2006.

[29] D. Ge, Z. Zeng, M. Arowo, H. Zou, J. Chen, and L. Shao, “Degradation of methyl orange by ozone in the presence of ferrous and persulfate ions in a rotating packed bed,” *Chemosphere*, vol. 146, pp. 413–418, Mar. 2016.

[30] B. H. Hameed and T. W. Lee, “Degradation of malachite green in aqueous solution by Fenton process,” *J. Hazard. Mater.*, vol. 164, no. 2–3, pp. 468–472, 2009.

[31] N. K. Daud, M. A. Ahmad, and B. H. Hameed, “Decolorization of Acid Red 1 dye solution by Fenton-like process using Fe–Montmorillonite K10 catalyst,” *Chem. Eng. J.*, vol. 165, no. 1, pp. 111–116, Nov. 2010.

[32] S. K. Kansal, M. Singh, and D. Sud, “Studies on photodegradation of two commercial dyes in aqueous phase using different photocatalysts.,” *J. Hazard. Mater.*, vol. 141, no. 3, pp. 581–90, Mar. 2007.

[33] R. Raliya, C. Avery, S. Chakrabarti, and P. Biswas, “Photocatalytic degradation of methyl orange dye by pristine titanium dioxide, zinc oxide, and graphene oxide nanostructures and their composites under visible light irradiation,” *Appl. Nanosci.*, vol. 7, no. 5, pp. 253–259, Jun. 2017.

[34] N. Sridewi, L.-T. Tan, and K. Sudesh, “Solar Photocatalytic Decolorization and Detoxification of Industrial Batik Dye Wastewater Using P(3HB)-TiO2 Nanocomposite Films,” *CLEAN - Soil, Air, Water*, vol. 39, no. 3, pp. 265–273, Mar. 2011.

[35] R. L. Narayana, M. Matheswaran, A. A. Aziz, and P. Saravanan, “Photocatalytic decolourization of basic green dye by pure and Fe, Co doped TiO2 under daylight illumination,” *Desalination*, vol. 269, no. 1–3, pp. 249–253, Mar. 2011.

[36] P. V. Suraja, Z. Yaakob, N. N. Binitha, M. R. Resmi, and P. P. Silija, “Photocatalytic degradation of dye pollutant over Ti and Co doped SBA-15: Comparison of activities under visible light,” *Chem. Eng. J.*, vol. 176–177, pp. 265–271, Dec. 2011.

[37] Z. Zainal, L. K. Hui, M. Z. Hussein, Y. H. Taufiq-Yap, A. H. Abdullah, and I. Ramli, “Removal of dyes using immobilized titanium dioxide illuminated by fluorescent lamps.,” *J. Hazard. Mater.*, vol. 125, no. 1–3, pp. 113–20, Oct. 2005.

[38] S. Sostarturk, M. Simonic, and I. Petrinic, “Wastewater treatment after reactive

printing," *Dye. Pigment.*, vol. 64, no. 2, pp. 147–152, Feb. 2005.

[39] M. T. Yagub, T. K. Sen, S. Afroze, and H. M. Ang, "Dye and its removal from aqueous solution by adsorption: A review," *Adv. Colloid Interface Sci.*, vol. 209, no. Supplement C, pp. 172–184, Jul. 2014.

[40] D. O. Cooney, "The Nature of Adsorption," in *Adsorption Design for Wastewater Treatment*, 1st ed., Boca Raton, FL: CRC Press, 1999, pp. 27–38.

[41] G. Crini, "Non-conventional low-cost adsorbents for dye removal: a review.," *Bioresour. Technol.*, vol. 97, no. 9, pp. 1061–85, Jun. 2006.

[42] S. Babel and T. A. Kurniawan, "Low-cost adsorbents for heavy metals uptake from contaminated water: a review.," *J. Hazard. Mater.*, vol. 97, no. 1–3, pp. 219–43, Feb. 2003.

[43] O. Ozdemir, B. Armagan, M. Turan, and M. S. Çelik, "Comparison of the adsorption characteristics of azo-reactive dyes on mezoporous minerals," *Dye. Pigment.*, vol. 62, no. 1, pp. 49–60, Jul. 2004.

[44] E. M. Dias and C. Petit, "Towards the use of metal–organic frameworks for water reuse: a review of the recent advances in the field of organic pollutants removal and degradation and the next steps in the field," *J. Mater. Chem. A*, vol. 3, no. 45, pp. 22484–22506, 2015.

[45] M. H. Do *et al.*, "Activated carbon/Fe3O4 nanoparticle composite: Fabrication, methyl orange removal and regeneration by hydrogen peroxide," *Chemosphere*, vol. 85, no. 8, pp. 1269–1276, Nov. 2011.

[46] A. Mittal, A. Malviya, D. Kaur, J. Mittal, and L. Kurup, "Studies on the adsorption kinetics and isotherms for the removal and recovery of Methyl Orange from wastewaters using waste materials.," *J. Hazard. Mater.*, vol. 148, no. 1–2, pp. 229–40, Sep. 2007.

[47] D. Chen, J. Chen, X. Luan, H. Ji, and Z. Xia, "Characterization of anion–cationic surfactants modified montmorillonite and its application for the removal of methyl orange," *Chem. Eng. J.*, vol. 171, no. 3, pp. 1150–1158, Jul. 2011.

[48] J. Zhang, Q. Zhou, and L. Ou, "Kinetic, Isotherm, and Thermodynamic Studies of the Adsorption of Methyl Orange from Aqueous Solution by Chitosan/Alumina Composite," *J. Chem. Eng. Data*, vol. 57, no. 2, pp. 412–419, Feb. 2012.

[49] Y. Yao, H. Bing, X. Feifei, and C. Xiaofeng, "Equilibrium and kinetic studies of methyl orange adsorption on multiwalled carbon nanotubes," *Chem. Eng. J.*, vol. 170, no. 1, pp. 82–89, May 2011.

[50] K. Sui *et al.*, "Biocomposite fiber of calcium alginate/multi-walled carbon nanotubes with enhanced adsorption properties for ionic dyes.," *Carbohydr. Polym.*, vol. 90, no. 1, pp. 399–406, Sep. 2012.

[51] H. Y. Zhu, R. Jiang, L. Xiao, and G. M. Zeng, "Preparation, characterization, adsorption kinetics and thermodynamics of novel magnetic chitosan enwrapping nanosized gamma-Fe2O3 and multi-walled carbon nanotubes with enhanced adsorption properties for methyl orange.," *Bioresour. Technol.*, vol. 101, no. 14,

pp. 5063–9, Jul. 2010.

[52] J. Ma *et al.*, “Enhanced Adsorptive Removal of Methyl Orange and Methylene Blue from Aqueous Solution by Alkali-Activated Multiwalled Carbon Nanotubes,” *ACS Appl. Mater. Interfaces*, vol. 4, no. 11, pp. 5749–5760, Nov. 2012.

[53] L. Bertin, S. Berselli, F. Fava, M. Petrangeli-Papini, and L. Marchetti, “Anaerobic digestion of olive mill wastewaters in biofilm reactors packed with granular activated carbon and ‘Manville’ silica beads.,” *Water Res.*, vol. 38, no. 14–15, pp. 3167–78, Aug. 2004.

[54] B. Jha and D. N. Singh, “Basics of Zeolites,” in *Fly Ash Zeolites: Innovations, Applications, and Directions*, vol. 78, Singapore: Springer Singapore, 2016, pp. 5–31.

[55] B. Jha and D. N. Singh, “Applications of Fly Ash Zeolites: Case Studies,” in *Fly Ash Zeolites: Innovations, Applications, and Directions*, vol. 78, Singapore: Springer Singapore, 2016, pp. 191–202.

[56] S. K. Alpat, O. Ozbayrak, S. Alpat, and H. Akçay, “The adsorption kinetics and removal of cationic dye, Toluidine Blue O, from aqueous solution with Turkish zeolite.,” *J. Hazard. Mater.*, vol. 151, no. 1, pp. 213–20, Feb. 2008.

[57] S. Wang and E. Ariyanto, “Competitive adsorption of malachite green and Pb ions on natural zeolite.,” *J. Colloid Interface Sci.*, vol. 314, no. 1, pp. 25–31, Oct. 2007.

[58] A. Ayati, M. N. Shahrak, B. Tanhaei, and M. Sillanpää, “Emerging adsorptive removal of azo dye by metal–organic frameworks,” *Chemosphere*, vol. 160, pp. 30–44, Oct. 2016.

[59] A. Alshammari, Z. Jiang, and K. E. Cordova, “Metal Organic Frameworks as Emerging Photocatalysts,” in *Semiconductor Photocatalysis - Materials, Mechanisms and Applications*, W. Cao, Ed. London, United Kingdom: InTechOpen, 2016, pp. 301–341.

[60] K. S. Park *et al.*, “Exceptional chemical and thermal stability of zeolitic imidazolate frameworks,” *Proc. Natl. Acad. Sci.*, vol. 103, no. 27, pp. 10186–10191, Jul. 2006.

[61] H. Furukawa, K. E. Cordova, M. O’Keeffe, and O. M. Yaghi, “The Chemistry and Applications of Metal-Organic Frameworks,” *Science*, vol. 341, no. 6149, pp. 1230444–1230444, Aug. 2013.

[62] O. K. Farha *et al.*, “Metal-organic framework materials with ultrahigh surface areas: is the sky the limit?,” *J. Am. Chem. Soc.*, vol. 134, no. 36, pp. 15016–21, Sep. 2012.

[63] H. Furukawa *et al.*, “Isoreticular Expansion of Metal–Organic Frameworks with Triangular and Square Building Units and the Lowest Calculated Density for Porous Crystals,” *Inorg. Chem.*, vol. 50, no. 18, pp. 9147–9152, Sep. 2011.

[64] J. Aguilera-Sigalat and D. Bradshaw, “Synthesis and applications of metal-organic framework–quantum dot (QD@MOF) composites,” *Coord. Chem. Rev.*,

vol. 307, pp. 267–291, Jan. 2016.

[65] S. H. Jhung, N. A. Khan, and Z. Hasan, "Analogous porous metal–organic frameworks: synthesis, stability and application in adsorption," *CrystEngComm*, vol. 14, no. 21, p. 7099, 2012.

[66] C. Janiak and J. K. Vieth, "MOFs, MILs and more: concepts, properties and applications for porous coordination networks (PCNs)," *New J. Chem.*, vol. 34, no. 11, p. 2366, 2010.

[67] M. Eddaoudi *et al.*, "Systematic Design of Pore Size and Functionality in Isoreticular MOFs and Their Application in Methane Storage," *Science*, vol. 295, no. 5554, pp. 469–472, Jan. 2002.

[68] Z. Hasan and S. H. Jhung, "Removal of hazardous organics from water using metal-organic frameworks (MOFs): Plausible mechanisms for selective adsorptions," *J. Hazard. Mater.*, vol. 283, pp. 329–339, Feb. 2015.

[69] Y. Zhao, "Emerging Applications of Metal–Organic Frameworks and Covalent Organic Frameworks," *Chem. Mater.*, vol. 28, no. 22, pp. 8079–8081, Nov. 2016.

[70] P. Horcajada, C. Serre, M. Vallet-Regí, M. Sebban, F. Taulelle, and G. Férey, "Metal-organic frameworks as efficient materials for drug delivery.," *Angew. Chem. Int. Ed. Engl.*, vol. 45, no. 36, pp. 5974–8, Sep. 2006.

[71] K. Liang *et al.*, "Biomimetic mineralization of metal-organic frameworks as protective coatings for biomacromolecules.," *Nat. Commun.*, vol. 6, p. 7240, Jun. 2015.

[72] E. Haque *et al.*, "Adsorptive removal of methyl orange from aqueous solution with metal-organic frameworks, porous chromium-benzenedicarboxylates," *J. Hazard. Mater.*, vol. 181, no. 1–3, pp. 535–542, May 2010.

[73] E. Haque, V. Lo, A. I. Minett, A. T. Harris, and T. L. Church, "Dichotomous adsorption behaviour of dyes on an amino-functionalised metal–organic framework, amino-MIL-101(Al)," *J. Mater. Chem. A*, vol. 2, no. 1, pp. 193–203, 2014.

[74] S. Wu, L. Yu, F. Xiao, X. You, C. Yang, and J. Cheng, "Synthesis of aluminum-based MOF/graphite oxide composite and enhanced removal of methyl orange," *J. Alloys Compd.*, vol. 724, pp. 625–632, Nov. 2017.

[75] E. Haque, J. W. Jun, and S. H. Jhung, "Adsorptive removal of methyl orange and methylene blue from aqueous solution with a metal-organic framework material, iron terephthalate (MOF-235)," *J. Hazard. Mater.*, vol. 185, no. 1, pp. 507–511, Jan. 2011.

[76] T. Shen, J. Luo, S. Zhang, and X. Luo, "Hierarchically mesostructured MIL-101 metal–organic frameworks with different mineralizing agents for adsorptive removal of methyl orange and methylene blue from aqueous solution," *J. Environ. Chem. Eng.*, vol. 3, no. 2, pp. 1372–1383, Jun. 2015.

[77] M. Tong, D. Liu, Q. Yang, S. Devautour-Vinot, G. Maurin, and C. Zhong, "Influence of framework metal ions on the dye capture behavior of MIL-100 (Fe,

Cr) MOF type solids," *J. Mater. Chem. A*, vol. 1, no. 30, p. 8534, 2013.

[78] S. Wu, X. You, C. Yang, and J. Cheng, "Adsorption behavior of methyl orange onto an aluminum-based metal organic framework, MIL-68(Al)," *Water Sci. Technol.*, vol. 75, no. 12, pp. 2800–2810, Jun. 2017.

[79] A. Centrone, E. E. Santiso, and T. A. Hatton, "Separation of Chemical Reaction Intermediates by Metal-Organic Frameworks," *Small*, vol. 7, no. 16, pp. 2356–2364, Aug. 2011.

[80] B.-J. Zhu *et al.*, "Iron and 1,3,5-Benzenetricarboxylic Metal–Organic Coordination Polymers Prepared by Solvothermal Method and Their Application in Efficient As(V) Removal from Aqueous Solutions," *J. Phys. Chem. C*, vol. 116, no. 15, pp. 8601–8607, Apr. 2012.

[81] S. S. Y. Chui, S. M. F. Lo, J. P. H. Charmant, A. G. Orpen, and I. D. Williams, "A chemically functionalizable nanoporous material [Cu3(TMA)2 (H2O)3](n)," *Science*, vol. 283, no. 5405, pp. 1148–1150, 1999.

[82] Q. Min Wang *et al.*, "Metallo-organic molecular sieve for gas separation and purification," *Microporous Mesoporous Mater.*, vol. 55, no. 2, pp. 217–230, Sep. 2002.

[83] L. Hamon, E. Jolimaître, and G. D. Pirngruber, "CO2 and CH4 Separation by Adsorption Using Cu-BTC Metal−Organic Framework," *Ind. Eng. Chem. Res.*, vol. 49, no. 16, pp. 7497–7503, Aug. 2010.

[84] S. Lin *et al.*, "Adsorption behavior of metal–organic frameworks for methylene blue from aqueous solution," *Microporous Mesoporous Mater.*, vol. 193, pp. 27–34, Jul. 2014.

[85] S. Hosseini, M. A. Khan, M. R. Malekbala, W. Cheah, and T. S. Y. Choong, "Carbon coated monolith, a mesoporous material for the removal of methyl orange from aqueous phase: Adsorption and desorption studies," *Chem. Eng. J.*, vol. 171, no. 3, pp. 1124–1131, Jul. 2011.

[86] N. Fiol and I. Villaescusa, "Determination of sorbent point zero charge: usefulness in sorption studies," *Environ. Chem. Lett.*, vol. 7, no. 1, pp. 79–84, Feb. 2009.

[87] K. L. Tan and B. H. Hameed, "Insight into the adsorption kinetics models for the removal of contaminants from aqueous solutions," *J. Taiwan Inst. Chem. Eng.*, vol. 74, pp. 25–48, May 2017.

[88] Y. S. Ho and G. McKay, "Pseudo-second order model for sorption processes," *Process Biochem.*, vol. 34, no. 5, pp. 451–465, Jul. 1999.

[89] M. Ghaedi, A. M. Ghaedi, E. Negintaji, A. Ansari, A. Vafaei, and M. Rajabi, "Random forest model for removal of bromophenol blue using activated carbon obtained from Astragalus bisulcatus tree," *J. Ind. Eng. Chem.*, 2014.

[90] W. J. Weber and J. C. Morris, "Kinetics of Adsorption on Carbon from Solution," *J. Sanit. Eng. Div.*, vol. 89, no. 2, pp. 31–60, 1963.

[91] F. C. Wu, R. L. Tseng, and R. S. Juang, "Initial behavior of intraparticle diffusion

model used in the description of adsorption kinetics," *Chem. Eng. J.*, 2009.

[92] M. I. El-Khaiary, "Least-squares regression of adsorption equilibrium data: Comparing the options," *J. Hazard. Mater.*, vol. 158, no. 1, pp. 73–87, Oct. 2008.

[93] Y. Li *et al.*, "Removal of lead from aqueous solution by activated carbon prepared from Enteromorpha prolifera by zinc chloride activation," *J. Hazard. Mater.*, vol. 183, no. 1–3, pp. 583–589, Nov. 2010.

[94] I. Langmuir, "The adsorption of gases on plane surfaces of glass, mica and platinum," *J. Am. Chem. Soc.*, vol. 40, no. 9, pp. 1361–1403, Sep. 1918.

[95] Y. Liu and Y.-J. Liu, "Biosorption isotherms, kinetics and thermodynamics," *Sep. Purif. Technol.*, vol. 61, no. 3, pp. 229–242, Jul. 2008.

[96] C. Aharoni and M. Ungarish, "Kinetics of activated chemisorption. Part 2.—Theoretical models," *J. Chem. Soc. Faraday Trans. 1 Phys. Chem. Condens. Phases*, vol. 73, p. 456, 1977.

[97] J. Abdi, M. Vossoughi, N. M. Mahmoodi, and I. Alemzadeh, "Synthesis of metal-organic framework hybrid nanocomposites based on GO and CNT with high adsorption capacity for dye removal," *Chem. Eng. J.*, vol. 326, pp. 1145–1158, Oct. 2017.

[98] M. Kousha, E. Daneshvar, M. S. Sohrabi, M. Jokar, and A. Bhatnagar, "Adsorption of acid orange II dye by raw and chemically modified brown macroalga Stoechospermum marginatum," *Chem. Eng. J.*, vol. 192, pp. 67–76, Jun. 2012.

[99] K. Vijayaraghavan, T. Padmesh, K. Palanivelu, and M. Velan, "Biosorption of nickel(II) ions onto Sargassum wightii: Application of two-parameter and three-parameter isotherm models," *J. Hazard. Mater.*, vol. 133, no. 1–3, pp. 304–308, May 2006.

[100] C. Basar, "Applicability of the various adsorption models of three dyes adsorption onto activated carbon prepared waste apricot," *J. Hazard. Mater.*, vol. 135, no. 1–3, pp. 232–241, Jul. 2006.

[101] D. Angin, "Utilization of activated carbon produced from fruit juice industry solid waste for the adsorption of Yellow 18 from aqueous solutions.," *Bioresour. Technol.*, vol. 168, pp. 259–266, Sep. 2014.

[102] M. Kara, H. Yuzer, E. Sabah, and M. . Celik, "Adsorption of cobalt from aqueous solutions onto sepiolite," *Water Res.*, vol. 37, no. 1, pp. 224–232, Jan. 2003.

[103] D. Bingol, N. Tekin, and M. Alkan, "Brilliant Yellow dye adsorption onto sepiolite using a full factorial design," *Appl. Clay Sci.*, vol. 50, no. 3, pp. 315–321, Nov. 2010.

[104] F. Geyikçi, "Factorial design analysis for adsorption of Indigo Carmine onto Montmorillonite-Evaluation of the kinetics and equilibrium data," *Prog. Org. Coatings*, vol. 98, pp. 28–34, Sep. 2016.

[105] S. N. Nobar, "Cu-BTC Synthesis, Characterization and Preparation for Adsorption Studies," *Mater. Chem. Phys.*, vol. 213, pp. 343–351, 2018.

[106] K. Schlichte, T. Kratzke, and S. Kaskel, “Improved synthesis, thermal stability and catalytic properties of the metal-organic framework compound Cu3(BTC)2,” *Microporous Mesoporous Mater.*, vol. 73, no. 1–2, pp. 81–88, Aug. 2004.

[107] Y. Yang, P. Shukla, S. Wang, V. Rudolph, X.-M. Chen, and Z. Zhu, “Significant improvement of surface area and CO2 adsorption of Cu–BTC via solvent exchange activation,” *RSC Adv.*, vol. 3, no. 38, p. 17065, 2013.

[108] K.-S. Lin, A. K. Adhikari, C.-N. Ku, C.-L. Chiang, and H. Kuo, “Synthesis and characterization of porous HKUST-1 metal organic frameworks for hydrogen storage,” *Int. J. Hydrogen Energy*, vol. 37, no. 18, pp. 13865–13871, Sep. 2012.

[109] L. Chen *et al.*, “Effective Adsorption Separation of n -Hexane/2-Methylpentane in Facilely Synthesized Zeolitic Imidazolate Frameworks ZIF-8 and ZIF-69,” *Ind. Eng. Chem. Res.*, vol. 55, no. 40, pp. 10751–10757, Oct. 2016.

[110] Y.-R. Lee, M.-S. Jang, H.-Y. Cho, H.-J. Kwon, S. Kim, and W.-S. Ahn, “ZIF-8: A comparison of synthesis methods,” *Chem. Eng. J.*, vol. 271, pp. 276–280, Jul. 2015.

[111] H.-Y. Cho, J. Kim, S.-N. Kim, and W.-S. Ahn, “High yield 1-L scale synthesis of ZIF-8 via a sonochemical route,” *Microporous Mesoporous Mater.*, vol. 169, pp. 180–184, Mar. 2013.

[112] N. Torres *et al.*, “Implications of structural differences between Cu-BTC and Fe-BTC on their hydrogen storage capacity,” *Colloids Surfaces A Physicochem. Eng. Asp.*, vol. 549, no. February, pp. 138–146, Jul. 2018.

[113] F. Martínez, P. Leo, G. Orcajo, M. Díaz-García, M. Sanchez-Sanchez, and G. Calleja, “Sustainable Fe-BTC catalyst for efficient removal of methylene blue by advanced fenton oxidation,” *Catal. Today*, vol. 313, no. September, pp. 6–11, Sep. 2018.

[114] A. Dhakshinamoorthy *et al.*, “Comparison of Porous Iron Trimesates Basolite F300 and MIL-100(Fe) As Heterogeneous Catalysts for Lewis Acid and Oxidation Reactions: Roles of Structural Defects and Stability,” *ACS Catal.*, vol. 2, no. 10, pp. 2060–2065, Oct. 2012.

[115] S. Shahid and K. Nijmeijer, “High pressure gas separation performance of mixed-matrix polymer membranes containing mesoporous Fe(BTC),” *J. Memb. Sci.*, vol. 459, pp. 33–44, Jun. 2014.

[116] Y.-K. Seo *et al.*, “Large scale fluorine-free synthesis of hierarchically porous iron(III) trimesate MIL-100(Fe) with a zeolite MTN topology,” *Microporous Mesoporous Mater.*, vol. 157, pp. 137–145, Jul. 2012.

[117] G. Autie-Castro, M. A. Autie, E. Rodríguez-Castellón, C. Aguirre, and E. Reguera, “Cu-BTC and Fe-BTC metal-organic frameworks: Role of the materials structural features on their performance for volatile hydrocarbons separation,” *Colloids Surfaces A Physicochem. Eng. Asp.*, vol. 481, pp. 351–357, Sep. 2015.

[118] H. Dathe, E. Peringer, V. Roberts, A. Jentys, and J. A. Lercher, “Metal organic

frameworks based on Cu2+ and benzene-1,3,5-tricarboxylate as host for SO2 trapping agents," *Comptes Rendus Chim.*, vol. 8, no. 3–4, pp. 753–763, Mar. 2005.

[119] P. Chowdhury, C. Bikkina, D. Meister, F. Dreisbach, and S. Gumma, "Comparison of adsorption isotherms on Cu-BTC metal organic frameworks synthesized from different routes," *Microporous Mesoporous Mater.*, vol. 117, no. 1–2, pp. 406–413, Jan. 2009.

[120] J. McEwen, J.-D. Hayman, and A. Ozgur Yazaydin, "A comparative study of CO2, CH4 and N2 adsorption in ZIF-8, Zeolite-13X and BPL activated carbon," *Chem. Phys.*, vol. 412, pp. 72–76, Feb. 2013.

[121] H. Yin, H. Kim, J. Choi, and A. C. K. Yip, "Thermal stability of ZIF-8 under oxidative and inert environments: A practical perspective on using ZIF-8 as a catalyst support," *Chem. Eng. J.*, vol. 278, pp. 293–300, 2015.

[122] M. Du, L. Li, M. Li, and R. Si, "Adsorption mechanism on metal organic frameworks of Cu-BTC, Fe-BTC and ZIF-8 for CO 2 capture investigated by X-ray absorption fine structure," *RSC Adv.*, vol. 6, no. 67, pp. 62705–62716, 2016.

[123] M. Sanchez-Sanchez, I. de Asua, D. Ruano, and K. Diaz, "Direct Synthesis, Structural Features, and Enhanced Catalytic Activity of the Basolite F300-like Semiamorphous Fe-BTC Framework," *Cryst. Growth Des.*, vol. 15, no. 9, pp. 4498–4506, Sep. 2015.

[124] A. Dhakshinamoorthy *et al.*, "Iron(III) metal–organic frameworks as solid Lewis acids for the isomerization of α-pinene oxide," *Catal. Sci. Technol.*, vol. 2, no. 2, pp. 324–330, 2012.

[125] Y. Wang *et al.*, "Synthesis of ZIF-8 in a deep eutectic solvent using cooling-induced crystallisation," *Microporous Mesoporous Mater.*, vol. 195, pp. 50–59, Sep. 2014.

[126] M. He, J. Yao, Q. Liu, K. Wang, F. Chen, and H. Wang, "Facile synthesis of zeolitic imidazolate framework-8 from a concentrated aqueous solution," *Microporous Mesoporous Mater.*, vol. 184, pp. 55–60, Jan. 2014.

[127] M. Jian, B. Liu, G. Zhang, R. Liu, and X. Zhang, "Adsorptive removal of arsenic from aqueous solution by zeolitic imidazolate framework-8 (ZIF-8) nanoparticles," *Colloids Surfaces A Physicochem. Eng. Asp.*, vol. 465, pp. 67–76, Jan. 2015.

[128] C. McKinstry, E. J. Cussen, A. J. Fletcher, S. V. Patwardhan, and J. Sefcik, "Scalable continuous production of high quality HKUST-1 via conventional and microwave heating," *Chem. Eng. J.*, vol. 326, pp. 570–577, Oct. 2017.

[129] L. He *et al.*, "Silver nanoparticles prepared by gamma irradiation across metal–organic framework templates," *RSC Adv.*, vol. 5, no. 14, pp. 10707–10715, 2015.

[130] J. E. Conde-González, E. M. Peña-Méndez, S. Rybáková, J. Pasán, C. Ruiz-Pérez, and J. Havel, "Adsorption of silver nanoparticles from aqueous solution on copper-based metal organic frameworks (HKUST-1)," *Chemosphere*, vol. 150, pp. 659–666, May 2016.

[131] H. Kaur, G. C. Mohanta, V. Gupta, D. Kukkar, and S. Tyagi, “Synthesis and characterization of ZIF-8 nanoparticles for controlled release of 6-mercaptopurine drug,” *J. Drug Deliv. Sci. Technol.*, vol. 41, pp. 106–112, Oct. 2017.

[132] E. L. Bustamante, J. L. Fernández, and J. M. Zamaro, “Influence of the solvent in the synthesis of zeolitic imidazolate framework-8 (ZIF-8) nanocrystals at room temperature,” *J. Colloid Interface Sci.*, vol. 424, pp. 37–43, Jun. 2014.

[133] L. T. L. Nguyen, K. K. A. Le, and N. T. S. Phan, “A Zeolite Imidazolate Framework ZIF-8 Catalyst for Friedel-Crafts Acylation,” *Chinese J. Catal.*, vol. 33, no. 4–6, pp. 688–696, Apr. 2012.

[134] B. Luan Tran, H.-Y. Chin, B. K. Chang, and A. S. T. Chiang, “Dye adsorption in ZIF-8: The importance of external surface area,” *Microporous Mesoporous Mater.*, vol. 277, pp. 149–153, Mar. 2019.

[135] C. Chen, M. Zhang, Q. Guan, and W. Li, “Kinetic and thermodynamic studies on the adsorption of xylenol orange onto MIL-101(Cr),” *Chem. Eng. J.*, vol. 183, pp. 60–67, Feb. 2012.

[136] S.-H. Huo and X.-P. Yan, “Metal–organic framework MIL-100(Fe) for the adsorption of malachite green from aqueous solution,” *J. Mater. Chem.*, vol. 22, no. 15, p. 7449, 2012.

[137] P. Senthil Kumar, S. Ramalingam, C. Senthamarai, M. Niranjanaa, P. Vijayalakshmi, and S. Sivanesan, “Adsorption of dye from aqueous solution by cashew nut shell: Studies on equilibrium isotherm, kinetics and thermodynamics of interactions,” *Desalination*, vol. 261, no. 1–2, pp. 52–60, Oct. 2010.

[138] B. H. Hameed and A. A. Rahman, “Removal of phenol from aqueous solutions by adsorption onto activated carbon prepared from biomass material,” *J. Hazard. Mater.*, vol. 160, no. 2–3, pp. 576–581, Dec. 2008.

[139] A. T. Mohd Din, B. H. Hameed, and A. L. Ahmad, “Batch adsorption of phenol onto physiochemical-activated coconut shell,” *J. Hazard. Mater.*, vol. 161, no. 2–3, pp. 1522–1529, Jan. 2009.

[140] V. C. Srivastava, M. M. Swamy, I. D. Mall, B. Prasad, and I. M. Mishra, “Adsorptive removal of phenol by bagasse fly ash and activated carbon: Equilibrium, kinetics and thermodynamics,” *Colloids Surfaces A Physicochem. Eng. Asp.*, vol. 272, no. 1–2, pp. 89–104, Jan. 2006.

[141] H. Teng and C.-T. Hsieh, “Activation Energy for Oxygen Chemisorption on Carbon at Low Temperatures,” *Ind. Eng. Chem. Res.*, vol. 38, no. 1, pp. 292–297, Jan. 1999.

[142] W. Piasecki and W. Rudziński, “Application of the statistical rate theory of interfacial transport to investigate the kinetics of divalent metal ion adsorption onto the energetically heterogeneous surfaces of oxides and activated carbons,” *Appl. Surf. Sci.*, vol. 253, no. 13, pp. 5814–5817, Apr. 2007.

[143] F. M. Machado *et al.*, “Adsorption of Reactive Blue 4 dye from water solutions by carbon nanotubes: experiment and theory,” *Phys. Chem. Chem. Phys.*, vol.

14, no. 31, p. 11139, 2012.

[144] A. Dhakshinamoorthy, M. Alvaro, and H. Garcia, “Aerobic oxidation of cycloalkenes catalyzed by iron metal organic framework containing N-hydroxyphthalimide,” *J. Catal.*, vol. 289, pp. 259–265, May 2012.

[145] X. Zhou and X. Zhou, “The unit problem in the thermodynamic calculation of adsorption using the Langmuir equation,” *Chem. Eng. Commun.*, vol. 201, no. 11, pp. 1459–1467, Nov. 2014.

[146] N. M. Mahmoodi and F. Najafi, “Synthesis, amine functionalization and dye removal ability of titania/silica nano-hybrid,” *Microporous Mesoporous Mater.*, vol. 156, pp. 153–160, Jul. 2012.

[147] A. R. Khataee, A. Naseri, M. Zarei, M. Safarpour, and L. Moradkhannejhad, “Chemometrics approach for determination and optimization of simultaneous photooxidative decolourization of a mixture of three textile dyes,” *Environ. Technol.*, vol. 33, no. 20, pp. 2305–2317, Oct. 2012.

[148] A. Regti, M. R. Laamari, S.-E. Stiriba, and M. El Haddad, “Use of response factorial design for process optimization of basic dye adsorption onto activated carbon derived from Persea species,” *Microchem. J.*, vol. 130, pp. 129–136, Jan. 2017.

[149] T. Mathialagan and T. Viraraghavan, “Biosorption of Pentachlorophenol by Fungal Biomass from Aqueous Solutions: a Factorial Design Analysis,” *Environ. Technol.*, vol. 26, no. 5, pp. 571–580, May 2005.

[150] P. Agrawal and A. K. Bajpai, “Dynamic Column Adsorption Studies of Toxic Cr(VI) Ions onto Iron Oxide Loaded Gelatin Nanoparticles,” *J. Dispers. Sci. Technol.*, vol. 32, no. 9, pp. 1353–1362, Sep. 2011.

[151] S. Sadaf and H. N. Bhatti, “Evaluation of peanut husk as a novel, low cost biosorbent for the removal of Indosol Orange RSN dye from aqueous solutions: batch and fixed bed studies,” *Clean Technol. Environ. Policy*, vol. 16, no. 3, pp. 527–544, Mar. 2014.

[152] Z. Aksu, Ş. Ş. Çağatay, and F. Gönen, “Continuous fixed bed biosorption of reactive dyes by dried Rhizopus arrhizus: Determination of column capacity,” *J. Hazard. Mater.*, vol. 143, no. 1–2, pp. 362–371, May 2007.

[153] H. C. Thomas, “Heterogeneous Ion Exchange in a Flowing System,” *J. Am. Chem. Soc.*, vol. 66, no. 10, pp. 1664–1666, Oct. 1944.

[154] Y. H. Yoon and J. H. Nelson, “Application of Gas Adsorption Kinetics I. A Theoretical Model for Respirator Cartridge Service Life,” *Am. Ind. Hyg. Assoc. J.*, vol. 45, no. 8, pp. 509–516, Aug. 1984.

[155] R. M. Clark, “Evaluating the cost and performance of field-scale granular activated carbon systems,” *Environ. Sci. Technol.*, vol. 21, no. 6, pp. 573–580, Jun. 1987.

[156] G. Yan, T. Viraraghavan, and M. Chen, “A New Model for Heavy Metal Removal in a Biosorption Column,” *Adsorpt. Sci. Technol.*, vol. 19, no. 1, pp. 25–43, Feb. 2001.

[157] M. T. Yagub, T. K. Sen, S. Afroze, and H. M. Ang, “Fixed-bed dynamic column adsorption study of methylene blue (MB) onto pine cone,” *Desalin. Water Treat.*, vol. 55, no. 4, pp. 1026–1039, Jul. 2015.

[158] Z. Aksu and F. Gönen, “Biosorption of phenol by immobilized activated sludge in a continuous packed bed: prediction of breakthrough curves,” *Process Biochem.*, vol. 39, no. 5, pp. 599–613, Jan. 2004.

[159] R. Han *et al.*, “Adsorption of methylene blue by phoenix tree leaf powder in a fixed-bed column: experiments and prediction of breakthrough curves,” *Desalination*, vol. 245, no. 1–3, pp. 284–297, Sep. 2009.

[160] I. A. W. Tan, A. L. Ahmad, and B. H. Hameed, “Adsorption of basic dye using activated carbon prepared from oil palm shell: batch and fixed bed studies,” *Desalination*, vol. 225, no. 1–3, pp. 13–28, May 2008.

[161] K. H. Chu, “Fixed bed sorption: Setting the record straight on the Bohart–Adams and Thomas models,” *J. Hazard. Mater.*, vol. 177, no. 1–3, pp. 1006–1012, May 2010.

[162] J. Cruz-Olivares, C. Pérez-Alonso, C. Barrera-Díaz, F. Ureña-Nuñez, M. C. Chaparro-Mercado, and B. Bilyeu, “Modeling of lead (II) biosorption by residue of allspice in a fixed-bed column,” *Chem. Eng. J.*, vol. 228, pp. 21–27, Jul. 2013.

[163] X. Xu *et al.*, “Nitrate adsorption by stratified wheat straw resin in lab-scale columns,” *Chem. Eng. J.*, vol. 226, pp. 1–6, Jun. 2013.

[164] M. S. Podder and C. . Majumder, “Fixed-bed column study for As(III) and As(V) removal and recovery by bacterial cells immobilized on Sawdust/MnFe2O4 composite,” *Biochem. Eng. J.*, vol. 105, pp. 114–135, Jan. 2016.

Vita

Abdollah Karami was born in 1989, in Dubai, United Arab Emirates. He was educated in local public schools in Sharjah, UAE, and graduated in 2007. He received his B.Sc. degree in Chemical Engineering from the American University of Sharjah in 2012.

In 2015, he joined the Chemical Engineering master's program at the American University of Sharjah as a graduate teaching assistant. His research interests are in wastewater treatment and reuse, specifically, potential technologies for harnessing energy from wastewater. He is also interested in the applications of metal-organic frameworks in water treatment.